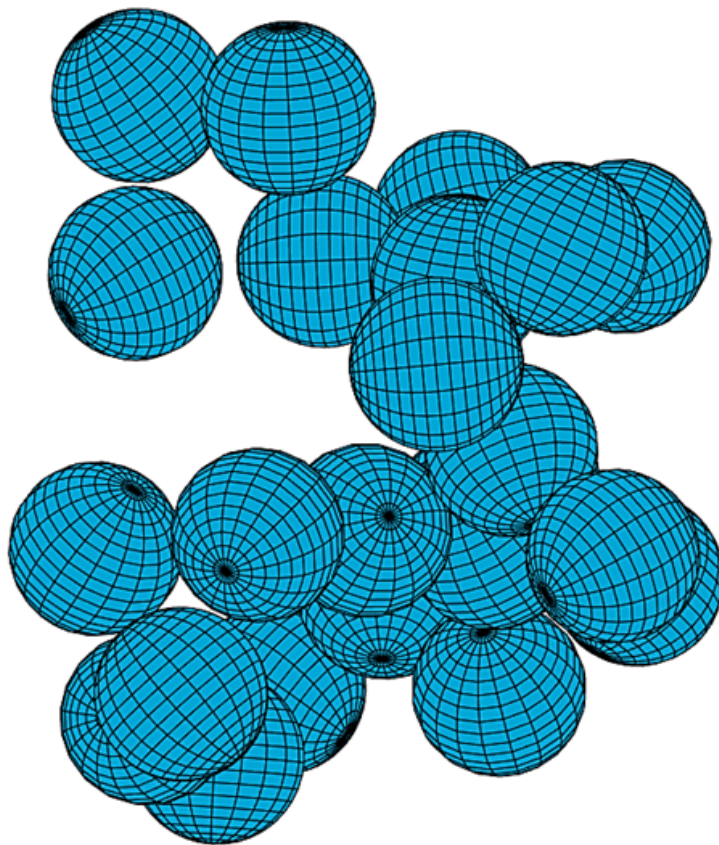


Numerical study of the sedimentation of particle suspensions in ducts

P&E report number 2960
[Luuk Altenburg](#)



Numerical study of the sedimentation of particle suspensions in ducts

MASTER THESIS

Solid & Fluid Mechanics, Faculty of Mechanical Engineering

by

L.A. ALTENBURG

to obtain the degree of Master of Science

at the Delft University of Technology,

to be defended publicly on Thursday March 14, 2019 at 02:00 PM.

Student number: 4104188

Thesis committee: Prof.dr.ir. C. Poelma, TU Delft
Dr.ir. W.P. Breugem, TU Delft, supervisor
Dr.ir. G.H. Keetels, TU Delft
Dr.ir. J.T. Padding, TU Delft

An electronic version of this thesis is available at <http://repository.tudelft.nl/>.



Abstract

Numerical study of the sedimentation of particle suspensions in ducts

by L.A. Altenburg

Sedimentation of particle suspensions is a relevant process to a variety of applications, such as the reclamation of land and chemical engineering systems. Direct numerical simulations of the settling of a single, two and multiple solid spheres under gravity in a square duct have been performed. The simulations involve 4 different Galileo numbers, i.e. $Ga = 144, 178, 200$ and 250 for a fixed solid-to-fluid-density ratio $\Gamma = 1.5$ and solid-volume fractions ranging from $\Phi = 0.005$ to $\Phi = 0.3$. It is shown that for these Ga the particle motions of a single particle are steady vertical, steady oblique, oblique oscillating and chaotic.

In the simulations for a single particle it has been found that the observed fluctuations of the vertical particle velocity are due to particle-wall interactions.

Drafting-kissing-tumbling (DKT), which is a key mechanism in the formation of particle clusters, has been observed in the two particles simulations and show that DKT initiates when the particles are almost aligned vertically and move in the same direction in the horizontal plane. DKT could occur even when the particles are several particle diameters apart.

In the simulations of multiple particles only the steady vertical, steady oblique and oblique oscillating regimes have been considered and the particles are initially randomly distributed in the computational domain. It is shown for these regimes that for solid-volume fractions $\Phi \leq 0.01$ an increase of the settling velocity of the suspensions compared to the value of a single particle is observed for all regimes, while for higher solid-volume fractions a hindered settling effect occurs. The statistics of a spatial parameter related to the angle of a particle and its nearest neighbour show that the particles align vertically more than a set of random distributed particles for solid-volume fractions $\Phi \leq 0.01$. This indicates the formation of particle clusters. These findings are supported by multiple instances of DKT observed in the animations of the simulations. Finally, it has been observed for all regimes that the vertical particle velocity fluctuations relative to the settling velocity of the suspension increase roughly with $\Phi^{1/3}$.

Acknowledgements

First of all I would like to thank my supervisor Wim-Paul Breugem for guiding me through this project. Especially the crash-courses in a variety of subjects, involving fluid dynamics and statistics, he gave in the personal meetings. These meetings were very helpful in improving my work and made me look at encountered problems from a different angle. He was also very understanding and patient when I sustained a knee injury last summer, for which I am grateful.

I would also like to thank Mathieu Pourquie for helping me out with the problems I encountered on the Reynolds cluster and granting me additional data storage.

Finally I would like to thank my family and friends for their support during this project.

Contents

Abstract	ii
Acknowledgements	iv
List of Figures	viii
List of Tables	x
List of Symbols	xi
1 Introduction	1
1.1 Motivation	1
1.2 Background	2
1.2.1 Sedimentation of a single spherical particle	2
1.2.2 Sedimentation of two spherical particles	5
1.2.3 Sedimentation of multiple spherical particles	6
1.3 Objective	10
1.4 Approach	10
2 Computational setup	12
2.1 Flow configuration single particle	12
2.1.1 Main setup	12
2.1.2 Wall effect setup	14
2.2 Flow configuration two particles	15
2.3 Flow configuration multiple particles	16
3 Results	18
3.1 Single particle	18
3.1.1 Steady vertical regime	19
3.1.2 Steady oblique regime	20
3.1.3 Oblique oscillating regime	25
3.1.4 Chaotic regime	27
3.1.5 Wall effects	29
3.2 Two particles	31
3.2.1 Steady vertical regime	31
3.2.2 Steady oblique regime	32
3.2.3 Oblique oscillating regime	36
3.2.4 Chaotic regime	37
3.3 Multiple particles	38
3.3.1 Steady vertical regime	39
3.3.2 Steady oblique regime	45
3.3.3 Oblique oscillating regime	50
3.3.4 Vertical particle velocity fluctuations	54

4 Conclusions	55
A Governing equations	57
A.1 Equations for flows with solid particles	57
A.2 Non-dimensionalized equations and free parameters	59
B Sphere dynamics	61
B.1 Morison's equation for a sphere settling under gravity in free space . . .	61
B.2 Wall effects on terminal settling velocity of a sphere in a quiescent fluid	63
B.3 Transient motion of a sphere	65
C Immersed boundary method and collision model	68
D Additional simulations	71
D.1 Flow around a fixed sphere	71
D.2 Effect of periodic boundary conditions	75
E Additional results	76
E.1 PDFs of the vertical particle velocity	76
F Random generator for particle distribution	79
Bibliography	81

List of Figures

1.1 Examples of gravity-driven particle-laden flow	1
1.2 C_D vs. Re by Boiko et al. [2]	3
1.3 Regimes of the trajectory of a single solid sphere settling under gravity by Jenny et al.[3]	3
1.4 The four regimes of a single solid sphere settling under gravity by Uhlmann and Doychev [7]	4
1.5 Drafting, kissing, tumbling	5
1.6 Average particle settling velocity vs. time by Uhlmann and Doychev [7]	8
1.7 Velocity PDFs for different Ga by Huisman et al.[15]	8
1.8 Sketch of intrinsic convection	9
2.1 Computational domains for a single sphere and two spheres	13
2.2 Computational domains for multiple spheres	17
3.1 S144A: Particle trajectory	19
3.2 S144A: Angular and vertical particle velocity	20
3.3 S178A: Particle trajectory	20
3.4 S178A: Angular and vertical particle velocity	21
3.5 S178A: Spectral analysis of the vertical particle velocity fluctuation .	22
3.6 S178A: Angle of particle motion vs. time	22
3.7 S178A: Particle velocity vs. distance to nearest wall	23
3.8 Wake structure for $Ga = 178$	24
3.9 S200A: Particle trajectory	25
3.10 S200A: Angular and vertical particle velocity	25
3.11 S200A: Spectral analysis of the vertical particle velocity fluctuation .	26
3.12 S200A: Particle velocity vs. distance to nearest wall	26
3.13 S250A: Particle trajectory	27
3.14 S250A: Angular and vertical particle velocity	27
3.15 S250A: Spectral analysis of the vertical particle velocity fluctuation .	28
3.16 S250A: Particle velocity vs. distance to nearest wall	28
3.17 S144B: Trajectory and vertical particle velocity	29
3.18 S144C: Trajectory and vertical particle velocity	30
3.19 Vertical particle velocity vs. duct width for $Ga = 144$	30
3.20 T144: Particle positions vs. time	31
3.21 T144: Vertical particle velocity vs. time	32
3.22 T178: Vertical particle positions vs. time	32
3.23 T178: DKT	33
3.24 T178: DKT onset	34
3.25 T178: Vertical particle velocity vs. time	35
3.26 T200: Vertical particle positions vs. time	36
3.27 T200: Vertical particle velocity vs. time	36
3.28 T250: Particle positions vs. time	37
3.29 ACF of the vertical particle velocity for M144A, M178A and M200A .	39

3.30	Average particle settling velocity vs. time for $Ga = 144$	39
3.31	Suspension settling velocity vs. solid-volume fraction for $Ga = 144$	40
3.32	$\log \frac{U_s}{U} $ vs. $\log(1 - \Phi)$ for $Ga = 144$	40
3.33	Distributions of the vertical particle velocity for $Ga = 144$	41
3.34	Particle locations seen from the top of the domain for M144A	42
3.35	Distributions of the angle θ for $Ga = 144$	43
3.36	DKT for M144A	44
3.37	Average particle settling velocity vs. time for $Ga = 178$	45
3.38	Suspension settling velocity vs. solid-volume fraction for $Ga = 178$	45
3.39	$\log \frac{U_s}{U} $ vs. $\log(1 - \Phi)$ for $Ga = 178$	46
3.40	Distributions of the vertical particle velocity for $Ga = 178$	46
3.41	Distributions of the angle θ for $Ga = 178$	48
3.42	Particle locations seen from the top of the domain for M178A	49
3.43	DKT for M178A	49
3.44	Average particle settling velocity vs. time for $Ga = 200$	50
3.45	Suspension settling velocity vs. solid-volume fraction for $Ga = 200$	50
3.46	$\log \frac{U_s}{U} $ vs. $\log(1 - \Phi)$ for $Ga = 200$	51
3.47	Distributions of the vertical particle velocity for $Ga = 200$	51
3.48	Distributions of the angle θ for $Ga = 200$	52
3.49	Particle locations seen from the top of the domain for M200B	53
3.50	DKT for M200B	53
3.51	Vertical particle velocity fluctuations vs. solid-volume fraction for all regimes	54
B.1	Schematic of a sphere falling in a duct	63
B.2	Vertical particle velocity in transient region	65
B.3	Predicted vertical position as a function of time	66
C.1	Eulerian and Lagrangian grid	68
C.2	Validation of collision model	70
D.1	C_D as a function of time steps for the flow around a fixed sphere	72
D.2	Velocity contour of a fixed sphere - $Ga = 144$	73
D.3	Velocity contour of a fixed sphere - $Ga = 178$	73
D.4	Velocity contour of a fixed sphere - $Ga = 200$	74
D.5	Velocity contour of a fixed sphere - $Ga = 250$	74
D.6	Periodic boundary effects on the settling velocity of the suspension	75
E.1	Distributions of the vertical particle velocity for $Ga = 144$ (complementary)	76
E.2	Distributions of the vertical particle velocity for $Ga = 178$ (complementary)	77
E.3	Distributions of the vertical particle velocity for $Ga = 200$ (complementary)	78

List of Tables

1.1	n as function of $\frac{D_p}{D_t}$ and Re_p by Richardson&Zaki [1]	6
1.2	Parameters of Ulmann and Doychev[7] and Huisman et al.[15]	7
2.1	Simulation parameters for the sedimentation of a single sphere	14
2.2	Simulation parameters for studying wall effects	14
2.3	Simulation parameters for the sedimentation of two spheres	15
2.4	Simulation parameters for the sedimentation of multiple spheres	16
B.1	Solutions to steady Morison's equation for multiple Ga	62
D.1	Simulation parameters for the flow around a fixed sphere	71

List of Symbols

A	surface area of the particle	m^2
A_{fs}	frontal surface area of the particle	m^2
C_D	drag coefficient	—
$C_D(Re)$	drag coefficient as function of (particle) Reynolds number Re	—
$C_D(Re_p)$	drag coefficient as function of particle Reynolds number Re_p	—
D_d	diameter of the duct	m
D_p	diameter of the particle	m
D_t	diameter of the tube	m
d_{wall}	distance of the particle surface to the nearest wall	m
g	gravitational acceleration	m s^{-2}
Ga	Galileo number	—
I_p	moment of inertia of particle	kg m^2
\mathbf{k}	unit vector in positive z -direction	—
L_x	length of the computational domain in the x -direction	m
L_y	length of the computational domain in the y -direction	m
L_z	length of the computational domain in the z -direction	m
n	Richardson-Zaki hindered settling index	—
\mathbf{n}	outward pointing unit normal vector	—
N_p	number of particles	—
N_t	number of simulated time steps	—
p	pressure	$\text{kg m}^{-1} \text{s}^{-2}$
Q	anti-symmetric part of the velocity gradient $\nabla \mathbf{u}$	s^{-1}
\mathbf{r}	position vector relative to the particle centroid	m
Re	Reynolds number	—
Re_p	particle Reynolds number	—
Re_T	particle Reynolds number at terminal settling velocity	—
S	symmetric part of the velocity gradient $\nabla \mathbf{u}$	s^{-1}
t	time	s
\mathbf{u}	velocity vector $\langle u, v, w \rangle$	m s^{-1}
\mathbf{u}_c	translational velocity vector of the particle centroid	m s^{-1}
$\mathbf{U}_{ps}(\mathbf{X})$	velocity vector of particle segment at position \mathbf{X}	m s^{-1}
\mathbf{U}_p	particle velocity vector $\langle U_{px}, U_{py}, U_{pz} \rangle$	m s^{-1}
\mathbf{U}_{pr}	particle velocity vector relative to ambient fluid velocity $\langle U_{prx}, U_{pry}, U_{prz} \rangle$	m s^{-1}
U_{pH}	horizontal particle velocity ($=\sqrt{U_{prx}^2 + U_{pry}^2}$)	m s^{-1}
U_{pV}	vertical particle velocity ($=U_{prz}$)	m s^{-1}
\overline{U}_{pV}	average particle settling velocity	m s^{-1}
U_{pV}^{rms}	standard deviation of the vertical particle velocity fluctuations	m s^{-1}
U_S	settling velocity of the suspension	m s^{-1}
U_T	terminal settling velocity of a single particle	m s^{-1}
V_p	volume of the particle	m^3
\mathbf{x}_c	position vector of the particle centroid $\langle x_c, y_c, z_c \rangle$	m
\mathbf{X}	position vector located on the particle surface	m

α	angle of particle motion with respect to the vertical	$^\circ$
Φ	solid-volume fraction	—
θ	angle of a particle with its nearest neighbouring particle and the vertical	$^\circ$
∇	gradient operator	m^{-1}
μ_f	dynamic viscosity	$kg\ m^{-1}\ s^{-1}$
ν_f	kinematic viscosity	$m^2\ s^{-1}$
λ_2	second eigenvalue of the tensor $\mathbf{S}^2 + \mathbf{Q}^2$	—
ρ_f	mass density of the fluid	$kg\ m^{-3}$
ρ_p	mass density of the solid	$kg\ m^{-3}$
Γ	solid-to-fluid-density ratio	—
τ	stress tensor for Newtonian fluid	$kg\ m^{-1}\ s^{-2}$
τ_{lag}	lag time	s
ω_c	angular velocity vector of the particle $\langle \omega_{cx}, \omega_{cy}, \omega_{cz} \rangle$	s^{-1}
ω_{cH}	angular particle velocity in the horizontal direction ($= \sqrt{\omega_{cx}^2 + \omega_{cy}^2}$)	s^{-1}
ω_{cV}	angular particle velocity in the vertical direction ($= \omega_{cz}$)	s^{-1}
\mathcal{L}	characteristic length scale ($= D_p$)	m
\mathcal{T}	characteristic time scale ($= \mathcal{L}/U$)	s
\mathcal{U}	characteristic velocity scale ($= [\Gamma - 1]gD_p]^{1/2}$)	$m\ s^{-1}$
\mathcal{Q}	a physical quantity	—
\mathcal{Q}'	fluctuation of Q	—

Chapter 1

Introduction

1.1 Motivation

Particle-laden flow is one of the main topics in the field of fluid dynamics. It involves complex multiphase interactions between a carrier phase and a dispersed phase, which are present in the form of a viscous fluid and (heavy) particles, respectively.

This study focuses on the the gravity-driven motion of multiple particles in an otherwise quiescent fluid. Examples of this flow configuration are removal of solid particles by sedimentation in a clarifier (waste-water treatment), the reclamation of land by propelling sand of dredging ships, which is also known as 'rainbowing' and chemical engineering systems, such as a fluidized bed reactor (FBR). The last mentioned usually involves a fluidization process, whereas the first two examples involve a sedimentation process. However from earlier studies by Richardson and Zaki [1] it can be concluded that sedimentation and fluidization of particles show similar dynamical behaviour. This flow configuration is also of interest in seismological studies, such as the settling of dust in the ocean after an earthquake.

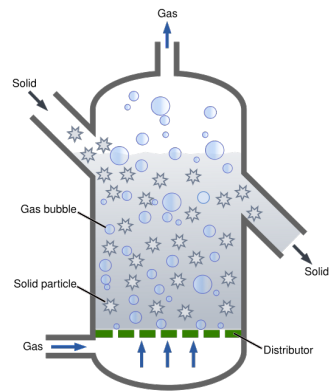


Figure 1.1 From left to right: A clarifier for treating waste water, a dredging ship during a 'rainbowing' process and a schematic of the flow in a FBR.
(Sources: www.tpmag.com, www.marineinsight.com and en.wikipedia.org)

1.2 Background

The collective behaviour of multiple particles (suspensions) sedimenting in an otherwise quiescent fluid is a challenging topic, of which full understanding has not been attained yet. This behaviour can be examined by looking at certain properties, such as the average settling velocity of the particles and their spatial distribution.

To explain the collective behaviour of sedimenting solid particles in dilute suspensions, it is important to understand the dynamics of a single isolated particle and the interplay between a small number of particles. In this chapter, earlier research on these subjects is presented. Starting with the sedimentation of a single particle, followed by the interplay between two particles and ending with collective behaviour of many particles in (dilute) suspensions. The first two subjects will be referred to as the *microscale* level, whereas the latter will be referred to as the *macroscale* level or the *collective*. Solid particles occur in many shapes in nature. However in the present work only spherical particles are considered, because of their simplicity, i.e. spheres act the same way in all directions.

1.2.1 Sedimentation of a single spherical particle

The research on a single sphere falling under gravity surrounded by a fluid starts with *Stokes Law*, which describes the drag force acting on slowly settling spherical objects in a viscous fluid, i.e. a low Reynolds number configuration ($Re \ll 1$).

In this so-called *Stokes regime* a sphere will settle along a straight vertical path and will reach a constant terminal velocity U_T , where the drag force F_D and buoyancy force F_B balance:

$$\underbrace{\frac{\pi}{8} C_D(Re) \rho_f D_p^2 U_T^2}_{F_D} = \underbrace{\frac{\pi D_p^3}{6} |\rho_p - \rho_f| g}_{F_B} \quad (1.1)$$

Where

- $C_D(Re)$ = drag coefficient as function of Reynolds number (Re),
- $Re = \frac{\rho_f D_p U_T}{\mu_f}$,
- D_p = diameter of the spherical particle,
- ρ_p = mass density of the spherical particle,
- ρ_f = mass density of the fluid,
- g = magnitude of the gravitational acceleration.

From Figure 1.2, a familiar graph seen in the field of fluid mechanics, the drag coefficient in the Stokes regime can be deduced and reads $C_D = 24/Re$. It then follows from equation 1.1 that the terminal particle velocity $U_T = \frac{|\rho_p - \rho_f| g D_p^2}{18 \mu_f}$.

At higher Reynolds numbers, Stokes Law will no longer hold and the flow around the sphere becomes more complex leading to wake instabilities and accompanying path instabilities.

For the settling of a freely moving sphere in a quiescent fluid it follows from dimensional analysis, that these instabilities depend on two non-dimensional parameters, i.e. **the solid-to-fluid-density ratio** $\Gamma = \frac{\rho_p}{\rho_f}$ and the **Galileo number** Ga . The derivation of these parameters will be described in Appendix A.1-A.2.

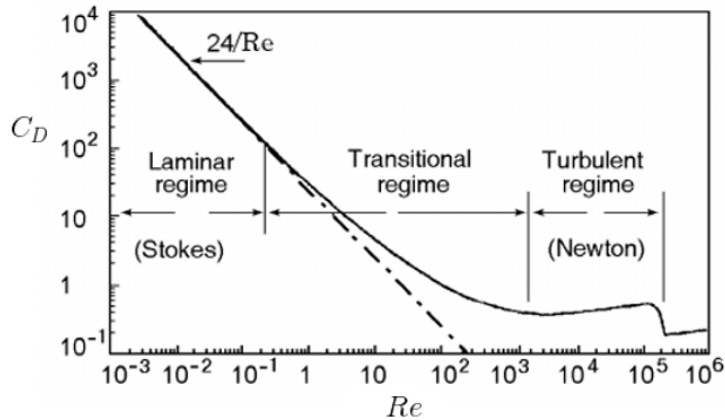


Figure 1.2 Drag coefficient as a function of the Reynolds Number for the flow over a sphere. Picture from the work of Boiko et al.[2].

The Ga -number is a measure for the ratio between the gravitational and viscous forces acting on a submerged particle and can be written in the form of a Reynolds number: $Ga = \frac{U\mathcal{L}}{\nu_f}$, where $U = (|\Gamma - 1|gD_p)^{1/2}$ is a characteristic velocity scale, $\mathcal{L} = D_p$ is a characteristic length scale and ν_f is the kinematic viscosity of the fluid. This two-parameter space has been extensively studied both numerically by Jenny et al.[3] and experimentally by Veldhuis and Biesheuvel among others [4, 5].

Figure 1.3 shows the numerical results by Jenny et al., where the regimes in the two-parameter space indicate the particle trajectory. In the present work the solid-to-fluid-density ratio $\Gamma = 1.5$, therefore the following path instabilities will occur with increasing Ga -number:

The sphere will have a steady vertical trajectory up to $Ga \approx 155$ (Regime I). Beyond this value the trajectory will be steady oblique up to $Ga \approx 185$ (Regime II). Further increase in Ga results in an oblique oscillating trajectory of the sphere up to $Ga \approx 215$ (Regime III) and finally the trajectory of the sphere becomes chaotic for $Ga \gtrsim 215$ (Regime VI).

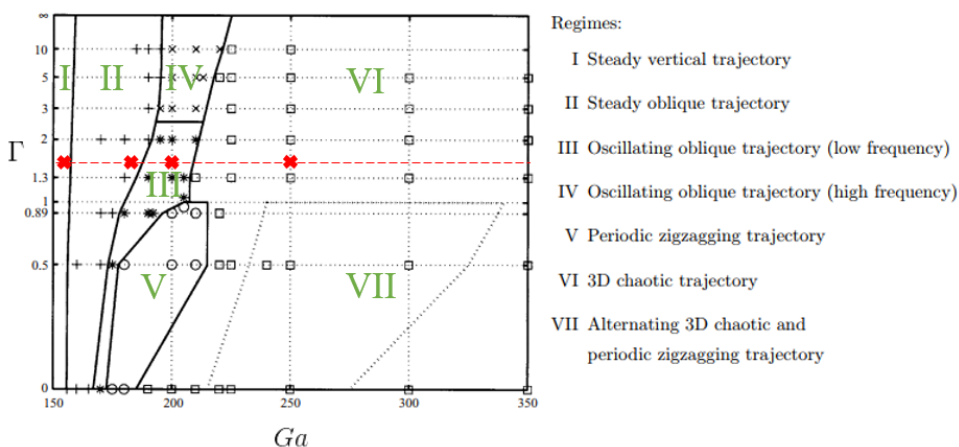


Figure 1.3 Numerical results of trajectories of a freely moving sphere in the two-parameter (Ga, Γ) space by Jenny et al.[3]. The red crosses indicate the Ga, Γ -couples used in the present work (see Section 1.4).

More recently Uhlmann and Dušek [6] performed benchmark studies for Ga numbers ranging from 144 to 250 and a solid-to-fluid-density ratio $\Gamma = 1.5$ to provide detailed data describing the settling of a sphere in a quiescent fluid. A visualization of the wake structures and particle motion of the four regimes is shown in Figure 1.4. The picture is taken from Uhlmann and Doychev [7] and summarizes the results of Uhlmann and Dušek [6] regarding the settling of a single solid sphere.

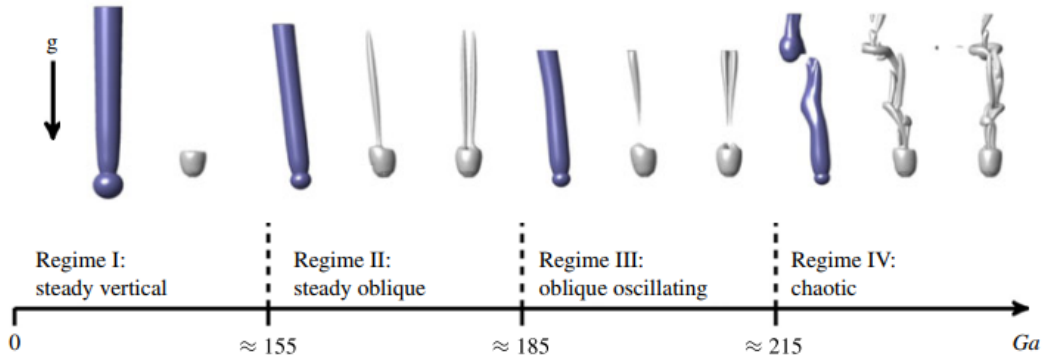


Figure 1.4 Visualization taken from [7]: The four regimes of a single sphere settling under gravity in an otherwise quiescent fluid. From left to right: $Ga = 144, 178, 190, 250$ and $\Gamma = 1.5$. The purple iso-surface indicates the vertical component of the fluid velocity equal to $1.2\mathcal{U}$ and the grey iso-surface visualizes the vortex structures by means of the λ_2 -method.

1.2.2 Sedimentation of two spherical particles

Besides the study of the motion of a single particle, it is important to mention a typical phenomenon in particle laden flows known as "drafting-kissing-tumbling" (DKT). This phenomenon has been demonstrated both experimentally by Fortes et al.[8] and numerically by Feng et al. among others [9–11].

DKT could occur when two particles are falling with their line-of-center (slightly) aligned in the direction of the gravity (vertical). The trailing particle may experience a smaller drag force than the leading particle when it enters the wake of the leading particle. Therefore the velocity of the trailing particle will be higher than the leading particle and they thus approach each other, which is known as "**drafting**". When the trailing particle touches the leading particle, the two particles will momentarily fall as a single body aligned with the vertical, which is known as "**kissing**".

This vertical alignment of the trailing and leading particle is unstable and causes the particles to tumble, resulting in the trailing particle overtaking the leading particle, known as "**tumbling**". Subsequently the particles will either repel each other or the DKT process repeats. In Figure 1.5 photographs of the fluidization experiment by Fortes et al.[8] visualize the DKT phenomenon. Note that DKT is similar in fluidization and sedimentation, since the dynamics is controlled by suctions of the wakes of spheres in relative motion.

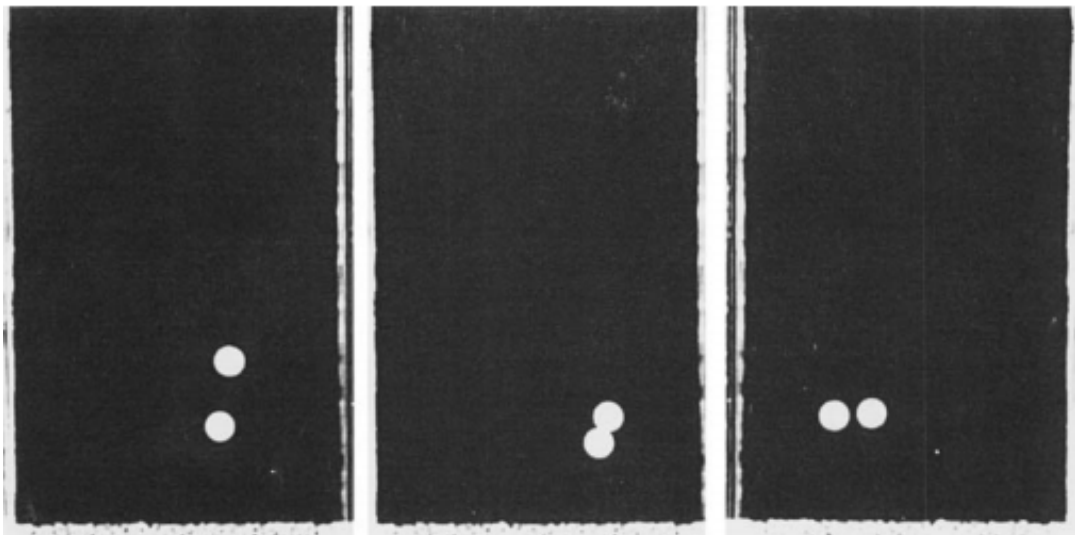


Figure 1.5 Photographs of the fluidization experiment by Fortes et al.[8]. The three photographs show drafting (left), kissing (middle) and tumbling (right) for $Re = \frac{u_f D_p}{\nu_f} = 800$, where u_f is the average fluid velocity.

1.2.3 Sedimentation of multiple spherical particles

The motion of a single particle settling under gravity (in an otherwise quiescent fluid) is determined by two parameters, i.e. the **solid-to-fluid-density ratio** Γ and the **Galileo number** Ga . When studying the motion of multiple particles settling under gravity, another parameter has to be taken into account. This parameter is the **solid-volume fraction** Φ . Extensive research has been done with regard to the sedimentation of dilute and dense suspensions of solid spheres.

In 1954 pioneers Richardson and Zaki investigated the sedimentation of dense suspensions ($\Phi > 0.04$). In their experiments they examined the effect of the solid-volume fraction of a suspension on its settling velocity [1]. As a result an empirical equation was developed, known as the Richardson-Zaki equation 1.2, which gives a prediction of the suspension settling velocity as a function of the solid-volume fraction and an experimentally determined exponent n . n is found to be a function of $\frac{D_p}{D_t}$ and $Re_p (= \frac{U_T D_p}{\nu_f})$, where D_t corresponds to the diameter of the tube used in their experiments. In Table 1.1 values for n as function of $\frac{D_p}{D_t}$ and Re_p are given.

$$\frac{U_S(\Phi)}{U_T} = (1 - \Phi)^n \quad (1.2)$$

Where

- $U_S(\Phi)$ = Settling velocity of the suspension,
- U_T = Terminal settling velocity of a single sphere,
- Φ = Solid-volume fraction of the suspension,
- n = Richardson-Zaki hindered settling index.

TABLE 1.1: n as function of $\frac{D_p}{D_t}$ and Re_p . These relations are valid for $0 < \frac{D_t}{D_p} < 2500$.

$n = 4.65 + 19.5 \cdot \frac{D_p}{D_t}$	for $Re_p < 0.2$
$n = (4.35 + 17.5 \cdot \frac{D_p}{D_t}) \cdot Re_p^{-0.03}$	for $0.2 < Re_p < 1$
$n = (4.45 + 18 \cdot \frac{D_p}{D_t}) \cdot Re_p^{-0.1}$	for $1 < Re_p < 200$
$n = 4.45 \cdot Re_p^{-0.1}$	for $200 < Re_p < 500$
$n = 2.39$	for $Re_p > 500$

To compare sedimentation and fluidization velocities suspensions, Richardson and Zaki performed experiments in which fluidization is followed by sedimentation. It can be concluded from their results that both the sedimentation and fluidization velocity are the same functions of the solid-volume fraction Φ and exponent n .

Baldock et al.[12] also performed experiments to investigate the reduction in the sedimentation (or fluidization) velocity as a function of the solid-volume fraction Φ and exponent n , known as the *hindered settling effect*. Their experiment was similar to the one Richardson and Zaki performed, however, instead of spherical particles, they used natural sands of different grain sizes and sphericity. They found that the values of n differ significantly from those suggested by Richardson and Zaki for spheres of equal sizes and that the values for n are larger, corresponding to a significantly greater *hindered settling effect*.

One of the first to perform direct numerical simulations of dilute suspensions of solid spheres ($\Phi = 0.002$) were Kajishima and Takiguchi [13]. In their simulations the effect of particle rotation was not accounted for. They observed the formation of particle clusters, in the case where $\Gamma = 8.8$, $Ga \approx 210$ ($Re_p \approx 300^1$), which resulted in an enhancement in the average settling velocity of the particles. The latter result was explained by the DKT process (see Section 1.2.2).

Later Kajishima and Takiguchi [14] performed simulations for identical parameters, but now taking particle rotation into account. No clusters were formed for this case, hence the rotational motion of particles has a significant influence in the (re)generation of particle clusters.

In 2014, Uhlmann and Doychev [7] numerically investigated the sedimentation of dilute suspensions of solid spheres ($\Phi = 0.005$). In their study four cases were simulated, two involving multiple particles (M121 and M178) and two involving a single particle (S121 and S178) for reason of validation and comparison. These specific cases and their (physical) parameters are listed in Table 1.2.

TABLE 1.2: Cases (and their physical parameters) investigated by Uhlmann and Doychev [7] and Huisman et al.[15].

	Ga	Γ	Φ
(M)121	1.5	5×10^{-3}	
(M)178	1.5	5×10^{-3}	
(S)121	1.5	5.3×10^{-5}	
(S)178	1.5	2.7×10^{-5}	
(M)178*	1.5	4.8×10^{-4}	

Recall that M121 and M178 correspond to a steady vertical path and a steady oblique trajectory, respectively, when considering a single isolated sphere.

The simulations were performed in triply periodic computational boxes and the numerical method used was the IBM of Uhlmann [16] (Immersed Boundary Method). Their work resulted in new insights in the behaviour of dilute sedimenting suspensions. No clusters were formed in the M121 case, whereas clear column clusters were observed for M178. Due to particle clustering the average particle settling velocity increased by 12% compared to the value of a single settling particle (S178), while there is no significant difference in the average particle settling velocity in case M121 compared to the value of a single settling particle (S121). However, the average relative particle settling velocity with respect to the local fluid velocity (return flow), which is averaged over a spherical shell around the particle, showed no significant difference with the terminal velocity of a single particle. This means that the particles preferentially sample downward fluid motions. Figure 1.6 summarizes the aforementioned findings regarding the average particle velocity by Uhlmann and Doychev.

¹ Ga and Re_p are related to each other and an approximate relation can be derived from Morison's equation, which describes the force balance for a particle in gravitational motion, see Appendix B.1

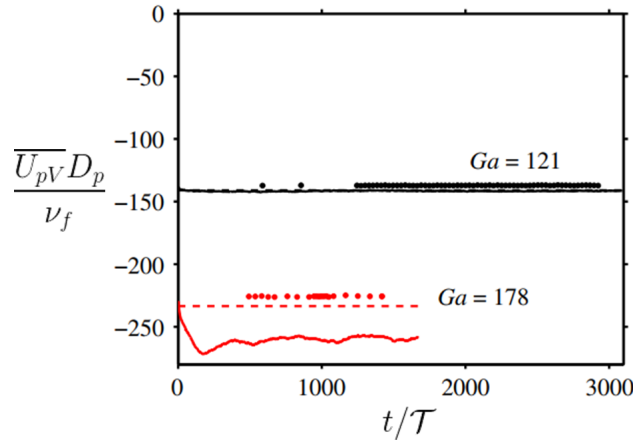


Figure 1.6 The average particle settling velocity ($\overline{U_{pV}}$) as a function of time by Uhlmann and Doychev [7]. Solid lines indicate the average particle velocity normalized with the particle diameter and the kinematic viscosity for M121 and M178. Dashed lines indicate the terminal velocity of a corresponding single sphere (S121 and S178). The settling velocity with respect to the local fluid velocity in the particles' vicinity is indicated by filled circular symbols.

The results from Uhlmann and Doychev were also experimentally verified by Huisman et al. [15]. In their experiment they investigated the settling of multiple particles with a Galileo number Ga varying from 110 to 310, a solid-to-fluid-density ratio $\Gamma = 2.5$ and solid-volume fractions Φ varying from 10^{-4} to 10^{-3} .

For comparison a numerical case, M178*, was added, which is identical to the M178 case of Uhlmann and Doychev [7], except for the solid-volume fraction ($\Phi = 4.8 \times 10^{-4}$, see Table 1.2). In Figure 1.7 the results of Huisman et al. [15], concerning the velocity of the particles, are displayed. Figure 1.7(b) shows the probability density functions of the vertical average particle velocities normalized by the settling velocity of a single (isolated) sphere U_T . The largest enhancement in the average particle velocity is for $Ga = 170$, which is notably higher than for $Ga = 110$ and $Ga = 310$. For $Ga = 110$ this is expected, since the particles are expected to have a steady vertical trajectory (Regime I). For the $Ga = 310$, their most probable explanation for this behaviour is that the chaotic wakes of the $Ga = 310$ particles might prohibit the formation of column clusters.

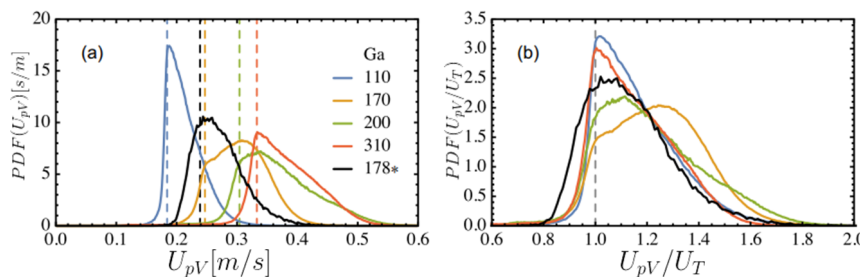


Figure 1.7 Particle velocity results of the experiments performed by Huisman et al. [15] **(a)** Velocity probability density functions as a function of Ga obtained from multiple experiments. **(b)** Probability density functions of the vertical particle velocity normalized by the settling velocity of a single (isolated) sphere U_T . U_T is indicated by the dashed lines. Note that M178* is the numerical simulation with $\Gamma = 1.5$, whereas $\Gamma = 2.5$ for the experiments.

The results from Uhlmann and Doychev regarding the average particle settling velocity seem to contradict Richardson and Zaki, since Uhlmann and Doychev observe that an increase in the solid-volume fraction Φ results in an increase in the average settling velocity of the particles. This contradiction can be clarified by the presence or absence of particle clusters. If there is no significant particle clustering, than the findings of Richardson and Zaki 1.2 hold. This is also validated by numerical studies by Fornari et al.[17]. It is important to emphasize the difference between the conditions in the experiments by Richardson and Zaki and the flow configuration in the simulations by Uhlmann and Doychev. The simulations were focused on dilute suspensions of solid spheres ($\Phi = 0.005$), whereas Richardson and Zaki have examined more dense suspensions ($\Phi > 0.04$) in their experiments. There is also a difference in the boundary conditions. In Uhlmann's simulations periodic boundary conditions in all three directions (x,y,z) were used. While in the experiments there was no periodicity in the horizontal directions(x,y), since a tube was used, which acts as a wall in the horizontal directions.

In this study the sedimentation of particles in a confined geometry is considered. Earlier work on this subject [18–20] reveals a macroscopic flow, known as *intrinsic convection*, which could influence the sedimentation of suspensions. A sketch of intrinsic convection is given in Figure 1.8. Intrinsic convection is a global convection in addition to settling of the particles relative to the fluid. An intrinsic flow could be formed due to the depletion of particles near the wall. Kuusela et al.[20] performed simulations at low particle Reynolds numbers ($Re_p < 10$) and found a depletion of particles at the walls for low solid-volume fractions, whereas an excess of particles is observed for high solid-volume fractions.

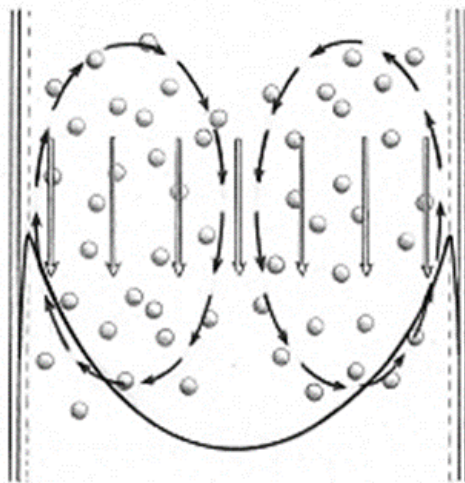


Figure 1.8 Sketch of intrinsic convection. Picture taken from [18].

1.3 Objective

In this study the gravity-induced settling of a suspension of solid particles in an other quiescent fluid is considered.

The main objective of this study is to investigate the effect of the solid-volume fraction of a suspension of solid spheres on its dynamical features taking into account wall effects. Dynamical features of interest are the average particle settling velocity and the spatial distribution of the sedimenting suspension of solid spheres. Accounting for walls in the horizontal directions (x,y) , by means of a square tube, gives a better resemblance of the experimental conditions, such as the cylindrical tubes used in the experiments of Richardson and Zaki [1] and the square tube used in the experiments by Huisman et al.[15].

1.4 Approach

From literature and dimensional analysis, it can be concluded that the sedimentation of suspensions of solid spheres in an otherwise quiescent fluid depends on upon three parameters: the solid-to-fluid-density ratio Γ , the Galileo number Ga and the solid-volume fraction Φ .

Solid-to-fluid-density ratio Γ

In this study a fixed solid-to-fluid-density ratio $\Gamma = 1.5$ is chosen. This corresponds to the value of plastic materials (polyester,PVC) in water.

Galileo number Ga

Concerning the Galileo number four values are considered, corresponding to different regimes of motion of a single sphere (see Figure 1.3):

- **$Ga = 144$** : steady vertical trajectory
- **$Ga = 178$** : steady oblique trajectory
- **$Ga = 200$** : oscillating oblique trajectory
- **$Ga = 250$** : chaotic trajectory

The combination of the solid-to-fluid-density ratio and the Galileo numbers corresponds to a particle Reynolds ranging from 185 to 362 according to Morison's equation for a sphere (see Appendix B.1).

Solid-volume fraction Φ

To investigate the influence of the solid-volume fraction the following values are considered:

- **$\Phi = 0.005$**
- **$\Phi = 0.010$**
- **$\Phi = 0.025$**
- **$\Phi = 0.050$**
- **$\Phi = 0.100$**
- **$\Phi = 0.200$**
- **$\Phi = 0.300$**

The solid-volume fractions are chosen, so that the method employed in this work could be validated and to investigate the collective behaviour for higher solid-volume fractions, which resemble the conditions of the experiments by Richardson and Zaki [1]. Results by Uhlmann and Dušek [6], Uhlmann and Doychev [7] and Huisman et al.[15] are used to validate and compare the results for the sedimentation of a single sphere and multiple spheres in the present work. Please note that the studies by Uhlmann are performed in triply periodic boxes.

Direct numerical simulations are performed in order to reach the objective. The numerical method employed in the simulations is the *immersed boundary method* (IBM) of Breugem [21]. This method is an improvement on the method used in the works of Uhlmann [6, 7, 16]. The improvement is due to three modifications made in the IBM of Uhlmann resulting in a second-order spatial accuracy and an improved numerical stability. For details on the characteristics of an *immersed boundary method* and the modifications made by Breugem, see Appendix C.

For the numerical investigation the following approach is used: First the gravitational motion of a single sphere (for each Ga, Γ -couple) is simulated to examine and validate its dynamical features. Secondly, simulations involving two falling spheres are performed to examine whether drafting-kissing-tumbling occurs or not. Finally, simulations of suspensions of solid spheres with solid-volume fractions Φ are performed for $Ga = 144, 178$ and 200 to explore and inspect its (collective) dynamical features.

Chapter 2

Computational setup

In this chapter the flow configurations and parameters used to simulate the sedimentation of a single sphere, two spheres and multiple spheres are explained and illustrated. The computational domain and boundary conditions used for a single sphere and two spheres are similar. For the simulation of multiple falling spheres the boundary condition in the vertical direction differs from the one employed in the single/two sphere setup. The collision model of Glowinski et al.[11] is used to accommodate for collisions between spheres and between spheres and walls. This model is briefly explained in Appendix C. For all simulations a Cartesian coordinate system is used, where the vertical z -direction is opposite to the direction of gravity. The grid size is $D_p/\Delta x = 16$.

2.1 Flow configuration single particle

2.1.1 Main setup

The computational domain, used for simulating the sedimentation of a single sphere taking into account wall effects, is sketched in Figure 2.1. The domain has horizontal lengths $L_x = L_y = 6D_p$ and vertical length $L_z = 24D_p$. In the simulation an inlet velocity is imposed at the inflow plane (blue) with $\mathbf{u}_\infty = \langle 0, 0, w_\infty \rangle$. A Neumann boundary condition for the velocity is set at the outflow plane (orange). Walls moving in the vertical direction are employed at the vertical planes (yellow), which means that no-slip/no-penetration conditions are imposed. The for-mentioned collision model of Glowinski was used for collisions between the sphere and the wall.

Neumann boundary conditions for the pressure are imposed at the inflow plane and the vertical planes. At the outflow plane a Dirichlet pressure boundary condition ($p = 0$) is imposed.

Applying these boundary conditions results in a moving frame of reference moving downwards with the magnitude of w_∞ . A moving frame of reference enables us to track the sphere in the computational domain for as long as possible, while using a relatively small computational box. Hence, the simulation is computationally efficient (the simulation costs are reduced).

The simulation is divided into two parts, which follow each other consecutively:

PART I In the first part the sphere is fixed ($x_c = y_c = 3D_p, z_c = 10D_p$) and a w_∞ is imposed at the inflow plane. The time the sphere is held fixed (t_{fixed}) is determined by the drag force acting on a single fixed sphere. Therefore additional simulations involving a fixed sphere are performed. The results of these simulations are presented in Appendix D.1.

PART II In the second part the simulation continues using the last flow field, but now the sphere is free to move in the entire computational domain for time t_{mobile} .

The value for w_∞ has to be chosen, so that the sphere does not reach either the bottom or top of the computational domain. The sphere has to remain a distance of $5D_p$ away from the inflow and outflow plane to ensure that the sphere does not influence the inflow and the sphere's wake is within the computational domain. The search for an appropriate value for w_∞ starts by solving Mordant's equation for steady motion for a sphere settling under gravity in free space for a given Ga (see Appendix B.1). The solution to this equation is the terminal settling velocity of a single sphere in free space U_T . When this solution is corrected by a crude estimate for the effect of walls on the terminal settling velocity of a single sphere (see Appendix B.2), one obtains a good starting point so that the amount of trials could be reduced in the search for an appropriate value for w_∞ . In Table 2.1 the parameters for the simulations of the sedimentation of a single sphere are displayed.

For each case a total of 30000 simulation time steps N_t are performed. The total simulation time differs for each case, since the duration of a time step depends on inlet velocity, which depends on the Galileo number Ga .

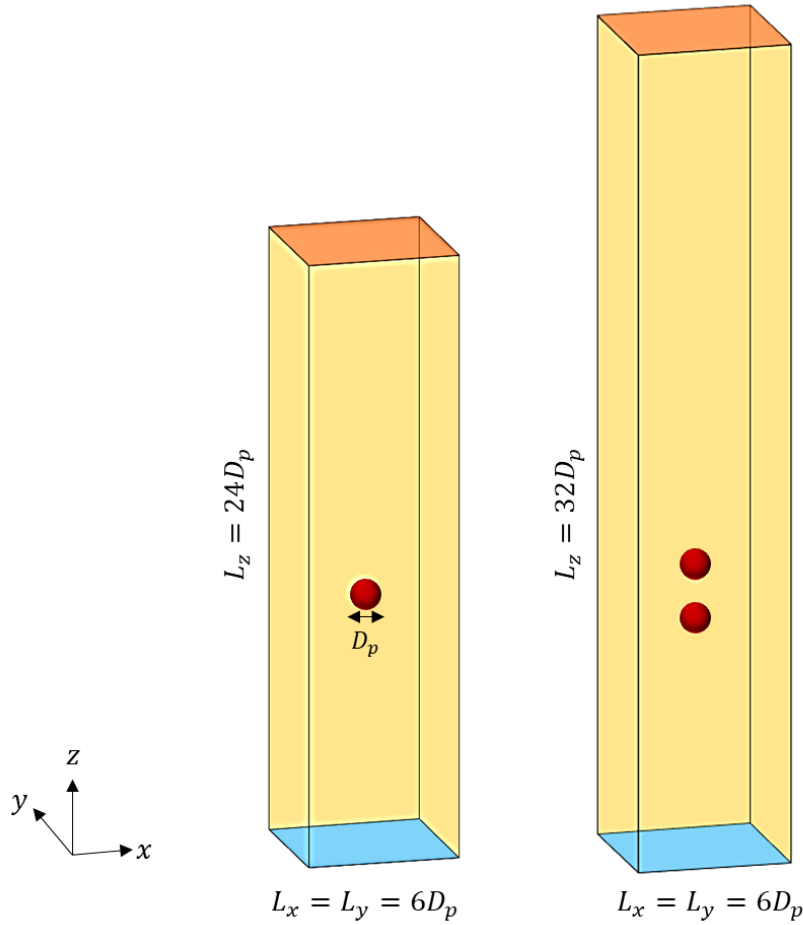


Figure 2.1 The computational domain employed in the simulations for the sedimentation of a single sphere (left) and two spheres (right).

TABLE 2.1: Simulation parameters for the sedimentation of a single sphere.

Case	Ga	Γ	w_∞/U_T	w_∞/\mathcal{U}	N_t	t_{fixed}/\mathcal{T}	t_{mobile}/\mathcal{T}
S144A	144	1.5	0.9920	1.2708	30000	52.70	734.98
S178A	178	1.5	0.9500	1.2799	30000	51.93	692.75
S200A	200	1.5	0.9250	1.2786	30000	51.50	678.69
S250A	250	1.5	0.9150	1.3235	30000	48.73	641.38

2.1.2 Wall effect setup

A single parameter combination, i.e. $Ga = 144$ and $\Gamma = 1.5$, was chosen to study the effect of the walls on the dynamics of a sphere falling under gravity in a square tube. Besides case S144A, two additional simulations involving a single sphere were performed with different cross section dimensions of the square tube (see Table 2.2).

TABLE 2.2: Additional simulation cases and their parameters for studying wall effects.

Case	Ga	Γ	w_∞/U_T	w_∞/\mathcal{U}	N_t	t_{fixed}/\mathcal{T}	t_{mobile}/\mathcal{T}	$\frac{L_x}{D_p} \times \frac{L_y}{D_p} \times \frac{L_z}{D_p}$
S144B	144	1.5	1.0050	1.2874	30000	52.38	730.88	$9 \times 9 \times 24$
S144C	144	1.5	1.0075	1.2906	30000	52.36	730.59	$12 \times 12 \times 24$

2.2 Flow configuration two particles

A different approach is used to perform the simulations of two falling spheres, i.e. simulating the *drafting-kissing-tumbling* phenomenon. The boundary conditions in the horizontal directions and the outflow plane are similar to the conditions described in Section 2.1. The values for the inlet velocity w_∞ imposed at the inflow plane and the initial positions for each case are displayed in Table 2.3. Note that the two spheres are not exactly aligned initially in the vertical direction, but instead a small offset is introduced in order to trigger the *drafting-kissing-tumbling* phenomenon. The domain is displayed in Figure 2.1 and has horizontal lengths $L_x = L_y = 6D_p$ and vertical length $L_z = 32D_p$. This means that the computational domain is extended in the vertical direction compared to the computational domain used for a single sphere.

The simulation consists of one part in which the spheres are released right from the start of the simulation. The spheres are released immediately to capture the transient motion of the two falling spheres and therefore give a better resemblance of two spheres falling and interacting with each other in the physical world. A small investigation on the transient motion of a falling sphere was performed in order to ensure that the spheres remain in the computational domain and a distance of $5D_p$ away from the inflow and outflow plane for the entire duration of the simulation. This is described in Appendix B.3.

TABLE 2.3: Simulation parameters for the sedimentation of two spheres. Subscript s indicates the sphere number.

Case	Ga	Γ	w_∞/\mathcal{U}	N_t	t_{sim}/\mathcal{T}	Initial sphere positions
						$\langle \frac{x_c}{D_p} \times \frac{y_c}{D_p} \times \frac{z_c}{D_p} \rangle_s$
T144	144	1.5	1.2375	45000	1193.07	$\langle 3\frac{1}{32}, 3\frac{1}{32}, 11 \rangle_1, \langle 2\frac{31}{32}, 2\frac{31}{32}, 9 \rangle_2$
T178	178	1.5	1.2665	45000	1100.31	$\langle 3\frac{1}{32}, 3\frac{1}{32}, 11 \rangle_1, \langle 2\frac{31}{32}, 2\frac{31}{32}, 9 \rangle_2$
T200	200	1.5	1.2821	45000	1066.76	$\langle 3\frac{1}{32}, 3\frac{1}{32}, 16 \rangle_1, \langle 2\frac{31}{32}, 2\frac{31}{32}, 14 \rangle_2$
T250	250	1.5	1.3198	45000	1009.74	$\langle 3\frac{1}{32}, 3\frac{1}{32}, 16 \rangle_1, \langle 2\frac{31}{32}, 2\frac{31}{32}, 14 \rangle_2$

2.3 Flow configuration multiple particles

The simulations of the sedimentation of suspensions of solid spheres are performed in a singly periodic computational domain, which means that periodic boundary conditions are employed in the vertical direction. Similar to the single and two sphere setup, walls are implemented in the horizontal directions. In Figure 2.2 a sketch of the computational domain is given, where the red and yellow planes indicate the periodic boundaries and the walls, respectively. Since a periodic system containing falling spheres will not reach a steady state, i.e. the falling spheres will keep accelerating, a constant vertical pressure gradient (z -direction) was imposed to enforce a zero mean flow in the vertical direction. The spheres are randomly distributed in the computational domain, such that the spheres do not overlap with each other nor the walls in the horizontal directions. The code for the random distribution of the spheres is appended in Appendix F.

The solid-volume fraction depends on the number of particles N_p and is defined by

$$\Phi = \frac{N_p \frac{\pi}{6} D_p^3}{L_x L_y L_z} \quad (2.1)$$

Where the domain dimensions are indicated in Figure 2.2.

A total of 21 simulations were performed: Seven different solid-volume fractions Φ are used in the simulations for three different Galileo numbers Ga . The duration of each simulation is $t = 900\mathcal{T}$. The Galileo numbers considered are $Ga = 144, 178, 200$, for which also reference data is available from the one and two spheres cases. An overview of the parameters is given in Table 2.4.

TABLE 2.4: Simulation parameters for the sedimentation of multiple spheres. xxx denotes one of three Galileo numbers $Ga = 144, 178, 200$.

Case	N_p	$\frac{L_x}{D_p} \times \frac{L_y}{D_p} \times \frac{L_z}{D_p}$	Φ
MxxxA	25	$6 \times 6 \times 72$	$5.1 \cdot 10^{-3}$
MxxxB	25	$6 \times 6 \times 36$	$1.0 \cdot 10^{-2}$
MxxxC	31	$6 \times 6 \times 18$	$2.5 \cdot 10^{-2}$
MxxxD	62	$6 \times 6 \times 18$	$5.0 \cdot 10^{-2}$
MxxxE	124	$6 \times 6 \times 18$	$1.0 \cdot 10^{-1}$
MxxxF	248	$6 \times 6 \times 18$	$2.0 \cdot 10^{-1}$
MxxxG	375	$6 \times 6 \times 18$	$3.0 \cdot 10^{-1}$

Note that the vertical length of the domain L_z is larger for the dilute suspensions (case MxxxA and MxxxB) compared to the other suspensions (case MxxxC-MxxxG). This is chosen in order to increase the number of particles N_p for a given concentration.

In Appendix D.2 a small investigation on the effect of the periodic boundary conditions is shown.

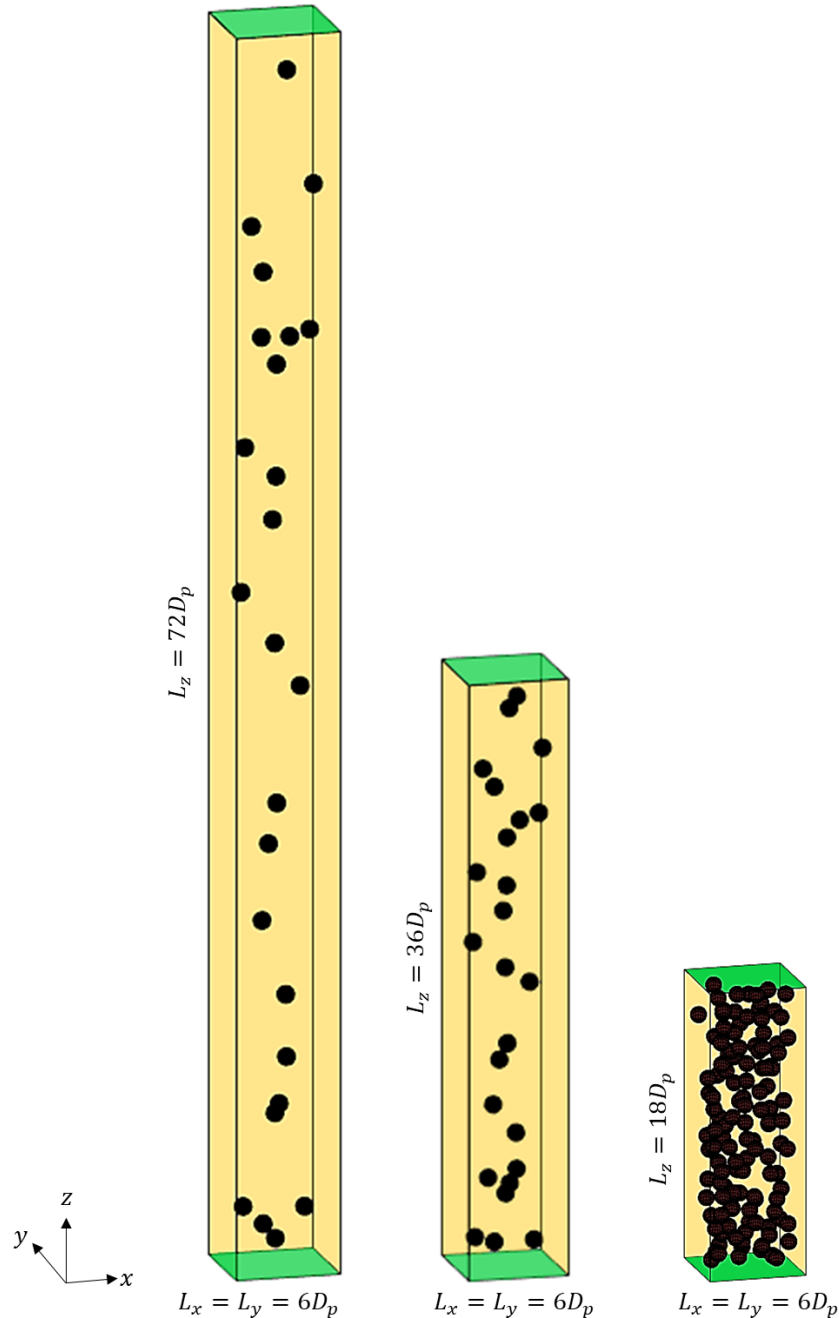


Figure 2.2 The computational domains employed in the simulations for the sedimentation multiple spheres. Left: Domain employed for case MxxxxA. Mid: Domain employed for case MxxxxB. Right: Domain employed for the 5 other cases. This particular setup is used for case M144E.

Chapter 3

Results

In this chapter the findings of the simulations described in Chapter 2 are presented. The first section will cover the simulation results for a single sphere and the simulations focusing on the wall effects, in the second section the results of the simulations involving two spheres are presented and the results of the simulations of multiple spheres are considered in the third section.

3.1 Single particle

In this section the results of the simulations involving the sedimentation of a single particle falling under gravity are discussed. The particle velocity relative to the ambient fluid velocity is defined in Equation 3.1 to avoid confusion when observing the figures displayed in this section.

$$\mathbf{U}_{\text{pr}} = \mathbf{U}_p - \mathbf{u}_\infty \quad (3.1)$$

Where $\mathbf{U}_{\text{pr}} = \langle U_{px}, U_{py}, U_{pz} \rangle$ and $\mathbf{u}_\infty = \langle 0, 0, w_\infty \rangle$.

The magnitude of the particle velocity in the horizontal plane is therefore defined as

$$U_{pH} = \sqrt{U_{px}^2 + U_{py}^2} \quad (3.2)$$

And the vertical particle velocity is given by

$$U_{pV} = U_{pz} \quad (3.3)$$

A similar approach holds for the angular velocity of the particle, where the angular particle velocity in the horizontal direction (ω_{cH}) and the vertical direction (ω_{cV}) are defined by

$$\omega_{cH} = \sqrt{\omega_{cx}^2 + \omega_{cy}^2} \quad (3.4)$$

$$\omega_{cV} = \omega_{cz} \quad (3.5)$$

Another parameter is the angle of particle motion with respect to the vertical (α) and it is defined by

$$\tan(\alpha) = \frac{U_{pH}}{|U_{pV}|} \quad (3.6)$$

In this section many results are compared to the findings by Uhlmann and Dušek [6]. Keep in mind that their simulations were performed in triply periodic boxes, i.e. no walls were implemented.

3.1.1 Steady vertical regime

In Figure 3.1 the results for the trajectory of the particle in the horizontal plane and the vertical position of the particle z_c in time are illustrated for case S144A.

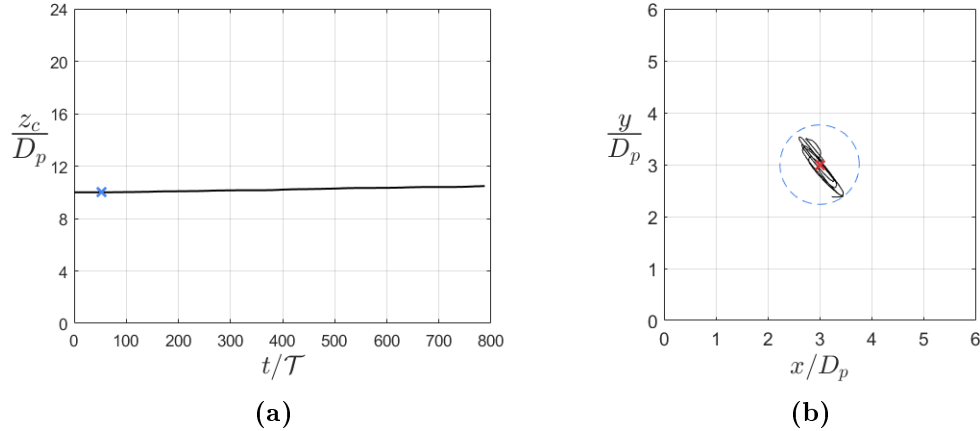


Figure 3.1 Results for case S144A ($Ga = 144$) (a) Temporal evolution of the vertical position of the particle z_c . The blue cross marks the particle's release. (b) Trajectory of a single sphere in the horizontal plane. The red cross marks the initial position of the particle and the blue dashed line indicates the region of motion.

Figure 3.1a shows that the particle remains a safe distance away from the inflow and outflow plane for the entire duration of the simulation, so that the inflow field is not disturbed and the wake of the particle is within the computational domain. It can be seen in Figure 3.1b that the particle trajectory is not perfectly steady vertical. This result differs from the findings by Uhlmann and Dušek [6], where no motion in the horizontal direction was found for the steady vertical regime. However, it is important to note that there were no walls present in their simulations, instead periodic boundary conditions were employed. The blue dashed line gives an indication of the region of particle motion in the horizontal plane. The radius of the region for S144A is $r_{motion} = 0.7641D_p$.

The results regarding the angular particle velocity are displayed in Figure 3.2a. It can be concluded from this figure that, in contrast to Uhlmann and Dušek, the angular particle velocity components are nonzero. Also note that the particle rotates at a higher rate in the horizontal direction compared to the rotation rate in the vertical direction.

Figure 3.2b displays the vertical particle velocity U_{pV} in time. The vertical particle velocity has been averaged over a time interval from $t = 110\mathcal{T}$ to $t = 685\mathcal{T}$ to determine the terminal settling velocity of the particle in the vertical direction U_T . This specific interval is chosen for consistency between the four cases. For S144A the terminal settling velocity of the particle $U_T = -1.2700\mathcal{U}$, which corresponds to a Reynolds number $Re_T = 182.88$.

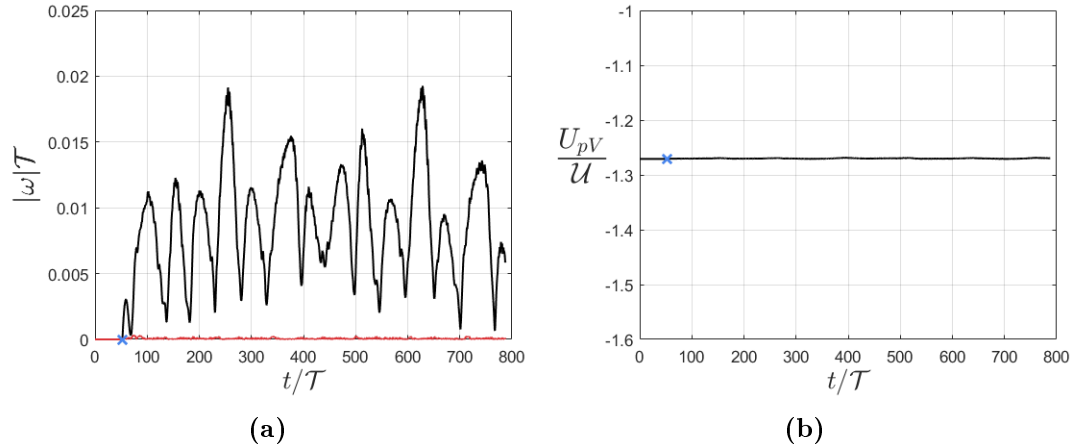


Figure 3.2 Results for case S144A ($Ga = 144$) (a) Temporal evolution of the vertical particle velocity U_{pV} . The blue cross marks the particle's release. (b) Temporal evolution of the magnitude of the angular particle velocity in the horizontal direction ω_{cH} (black solid line) and in the vertical direction ω_{cV} (red solid line).

3.1.2 Steady oblique regime

In Figure 3.3 the results for the trajectory of the particle in the horizontal plane and the vertical position of the particle z_c in time are illustrated for case S178A.

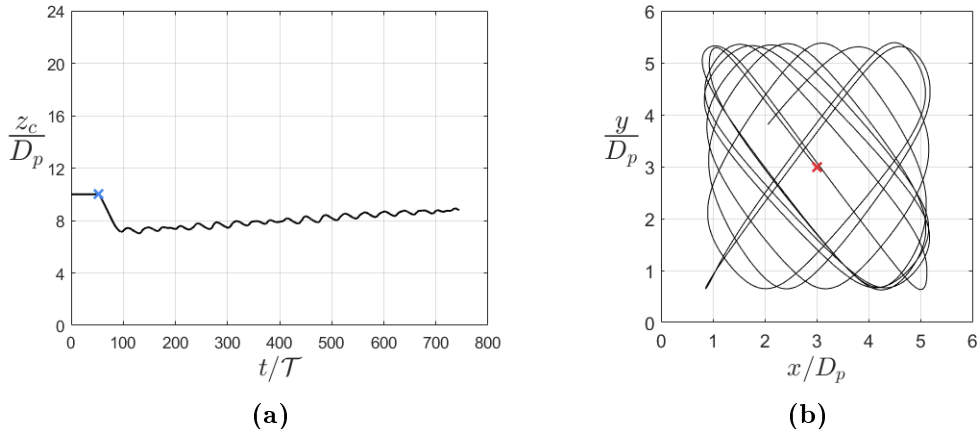


Figure 3.3 Results for case S178A ($Ga = 178$) (a) Temporal evolution of the vertical position of the particle z_c . The blue cross marks the particle's release. (b) Trajectory of a single sphere in the horizontal plane. The red cross marks the initial position of the particle.

It can be seen in Figure 3.3b that the particle moves in the entire domain and although it may hard to see, the particle never collides with any wall during the entire simulation.

Similar to S144A the angular particle velocity in the horizontal direction is higher than the angular particle velocity in the vertical direction. However the magnitude of the angular particle velocity of S178A differs by one order of magnitude compared to S144A (see Figure 3.4a).

Figure 3.4b shows the vertical particle velocity U_{pV} in time. When the sphere is released the magnitude of the vertical particle velocity increases initially, causing the sphere to move downwards (see Figure 3.3a). The vertical particle velocity has been

averaged over a time interval from $t = 110\mathcal{T}$ to $t = 685\mathcal{T}$ to determine the terminal settling velocity of the particle in the vertical direction U_T . As earlier mentioned, this specific interval is chosen for consistency between the four cases. For S178A the terminal settling velocity of the particle $U_T = -1.2777\mathcal{U}$, which corresponds to a Reynolds number $Re_T = 227.43$.

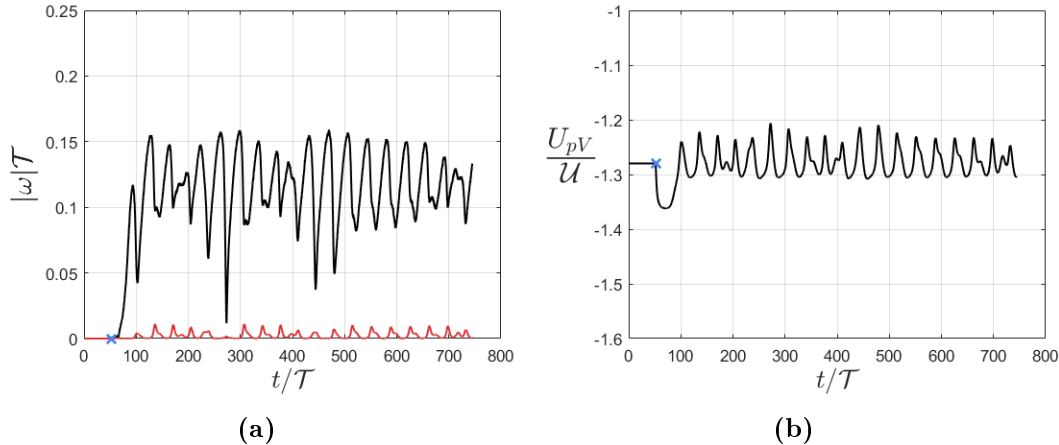


Figure 3.4 Results for case S178A ($Ga = 178$) (a) Temporal evolution of the vertical particle velocity U_{pV} . The blue cross marks the particle's release. (b) Temporal evolution of the magnitude of the angular particle velocity in the horizontal direction ω_{cH} (black solid line) and in the vertical direction ω_{cv} (red solid line).

Over this time interval ($t = 110\mathcal{T} - 685\mathcal{T}$) the vertical particle velocity fluctuates between $U_{pV,min} = -1.2061\mathcal{U}$ and $U_{pV,max} = -1.3085\mathcal{U}$, which means that the amplitude of the velocity fluctuations is $|\frac{U_{pV,max} - U_{pV,min}}{2}| = 0.0512\mathcal{U}$. Furthermore, a periodic behaviour is observed regarding these fluctuations. Therefore, a basic spectral analysis has been performed to determine which frequency dominates the fluctuations of the vertical particle velocity (Figure 3.4b). The Fourier transform is a tool to perform this analysis, since it identifies the frequency components of a time-domain signal. The analysis has been performed on the velocity fluctuation signal U'_{pV} between $t = 100\mathcal{T}$ and $t = 744\mathcal{T}$, where U'_{pV} is defined by U_{pV} minus the average of U_{pV} over the time interval. Figure 3.5 shows the single-sided amplitude spectrum of U'_{pV} . The largest amplitude of the Fourier transform is observed for a frequency $f = \frac{0.0284}{\mathcal{T}}$, which means that the periodicity of the vertical particle velocity is characterized by this frequency. Another observation, based on Figure 3.7, is that the particle approaches the wall 18 times between $t = 100\mathcal{T}$ and $t = 744\mathcal{T}$. This corresponds to a frequency $f = \frac{18}{744\mathcal{T} - 100\mathcal{T}} = \frac{0.0280}{\mathcal{T}}$, which (roughly) corresponds to the frequency found with the spectral analysis. Hence, it can be concluded that the fluctuations of the vertical particle velocity are dominated by the interactions with the walls.

Note that the peak amplitude in the Fourier transform does not match the amplitude of the velocity fluctuations in the time domain. This is probably due to spectral leakage.

The angle of particle motion with respect to the vertical (α) has been plotted against the simulated time in Figure 3.6. Despite some outliers it can be calculated that α fluctuates around 7.9° . This value differs significantly from the value obtained by Uhlmann and Dušek [6] ($\alpha \approx 5.3^\circ$), where periodic conditions (instead of walls) were employed.

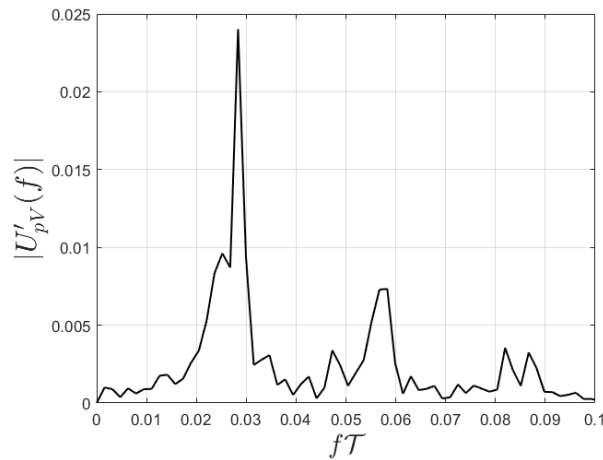


Figure 3.5 Single-sided amplitude spectrum of $U'_{pV}(t)$: the magnitude of the vertical particle velocity in the frequency domain $U'_{pV}(f)$ plotted against the frequency normalized by the characteristic time scale \mathcal{T} .

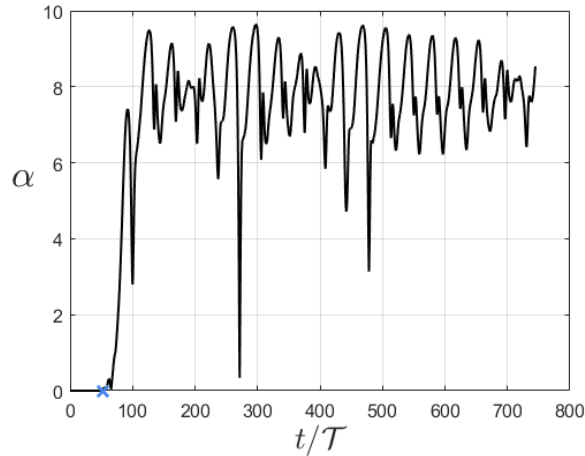


Figure 3.6 The angle of particle motion with respect to the vertical (α) plotted against time. The blue cross marks the particle's release.

Figure 3.7 shows a pronounced wall effect over a distance in the order of one particle diameter D_p : Both the vertical and horizontal velocity of the particle decrease each time it approaches a wall and increase when it moves away from the wall. Remark that the magnitude of the vertical particle velocity reaches a certain maximum value when it moves away from the wall. In this figure d_{wall} is defined as the nearest distance of the particle surface to either the walls in the x -direction or the y -direction. The decrease in the vertical particle velocity as it approaches a wall is explained as follows: As the fluid between the wall and the particle is getting more and more squeezed as the particle approaches the wall, the velocity gradient near the surface of the particle increases. When the velocity gradient increases, the shear stress acting on the particle surface also increases and thus an increase in drag acting on the particle. Hence, the vertical particle velocity decreases.

Since the particle never collides with a wall during the entire simulation and the fact that the horizontal particle velocity decreases each time it approaches a wall give rise to the presumption that the particle experiences a lubrication effect. However, because of the relatively large gap between the surface of the particle and the wall in present simulations, lubrication theory fails. Lubrication models, such as the well-known lubrication model described in the paper of Davis et al.[22] are valid under the condition that: $d_{wall}/(\frac{1}{2}D_p) \ll 1$. From Figure 3.7 a minimum gap width of $d_{wall}/(\frac{1}{2}D_p) = 0.2246$ is obtained, hence the lubrication theory is invalid. Although the for-mentioned does not explain why the particle never collides with the wall, it does eliminate a plausible explanation.

A possible explanation, found in literature, is a wall-induced lift force acting on the particle. Takemura and Magnaudet [23] discussed two hydrodynamical mechanisms of wall-induced lift force for the case of a sphere moving parallel to a wall in an otherwise quiescent fluid: A vortical mechanism and an irrotational mechanism. The vortical mechanism is related to the vorticity generated at the sphere surface, which advects and diffuses downstream and interacts with the wall. This interaction results in a lift force acting on the sphere directed away from the wall (repulsive force).

The irrotational mechanism is related to the irrotational (or potential) flow theory. This theory predicts that the presence of a wall tends to accelerate the fluid in the gap between the sphere surface and the wall, resulting in a local pressure drop and thus a lift force acting on the particle directed towards the wall (attractive force). It was observed in the experiments of Takemura and Magnaudet [23], for a solid sphere with Reynolds numbers up to $Re_p \approx 100$, that the vortical mechanism dominates. Hence, the lift force acting on the sphere is directed away from the wall. Numerical studies by Zeng et al.[24] confirm the findings by Takemura and Magnaudet. They found that the vortical mechanism also dominates for Reynolds numbers above $Re_p \approx 100$ up to $Re_p = 300$. Furthermore, they observe an increase in the wall-induced lift coefficient with increasing Re_p above about 100, which is suggested to be due to the formation of a double-threaded wake structure.

It is shown in Figure 3.8, a double-threaded wake structure was also observed in the present simulation (case S178A). This strongly supports the explanation of a repulsive lift force preventing the particle from colliding with the wall.

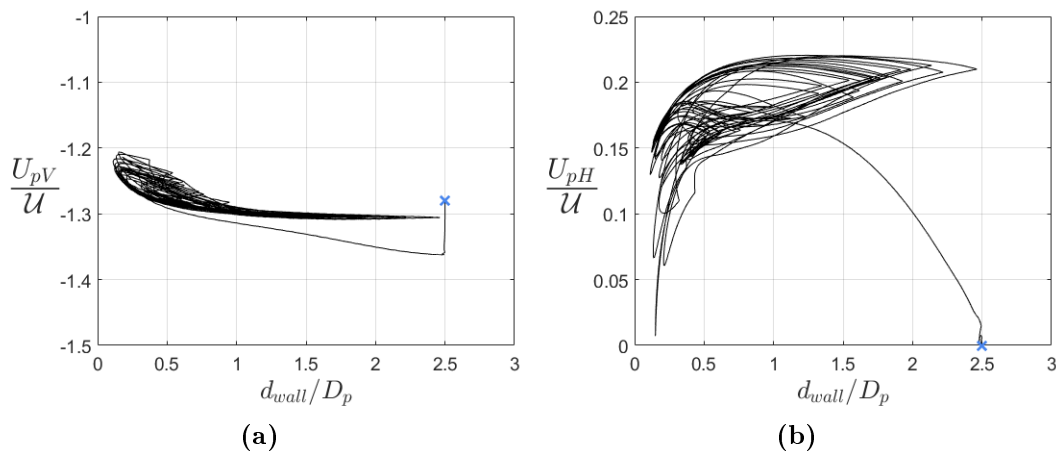


Figure 3.7 (a) The vertical particle velocity and (b) the horizontal particle velocity plotted against the distance to the nearest wall d_{wall} . The blue cross marks the particle's release. d_{wall} is defined by $d_{wall} = \min(x_c, L_x - x_c, y_c, L_y - y_c) - \frac{1}{2}D_p$.

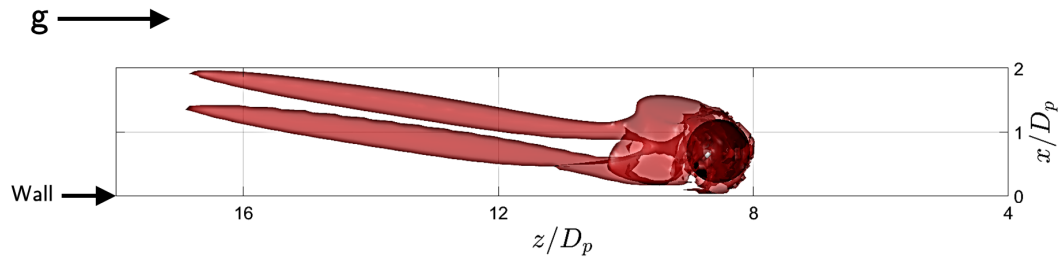


Figure 3.8 Iso-surface plot revealing the wake structure of the particle close to the wall for $Ga = 178$ using the λ_2 -method ($\lambda_2 = -0.015$). The wake structure shows a double-threaded vortex. The λ_2 -method is explained in Section 3.2.2.

3.1.3 Oblique oscillating regime

In Figure 3.9 the results for the trajectory of the particle in the horizontal plane and the vertical position of the particle z_c in time are illustrated for case S200A.

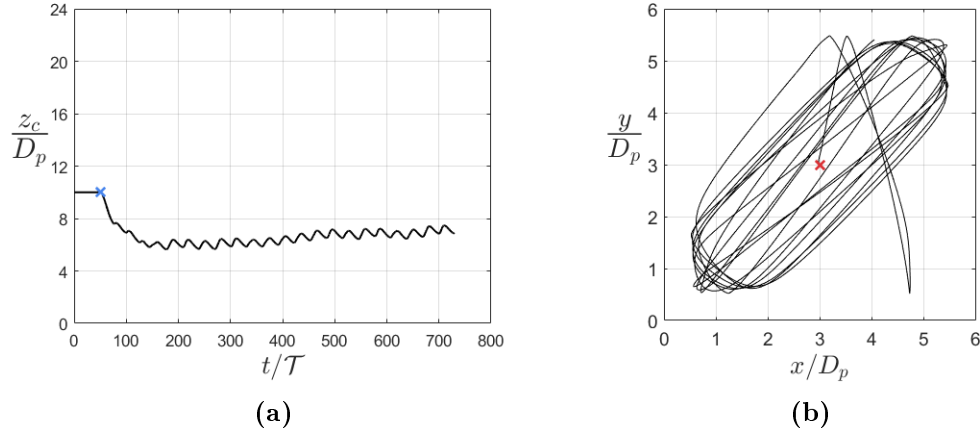


Figure 3.9 Results for case S200A ($Ga = 200$) (a) Temporal evolution of the vertical position of the particle z_c . The blue cross marks the particle's release. (b) Trajectory of a single sphere in the horizontal plane. The red cross marks the initial position of the particle.

From Figure 3.9a it can be concluded that the particle remains a safe distance away from the in- and outflow plane during the entire simulation. The particle moves in diagonal pattern in the horizontal plane and for this case collisions between the particle and the wall do occur, however the number of collisions was 6.

In Figure 3.10 the temporal evolution of the angular and vertical particle velocity are displayed. For S200A the terminal settling velocity of the particle $U_T = -1.2780\mathcal{U}$, which corresponds to a Reynolds number $Re_T = 255.60$.

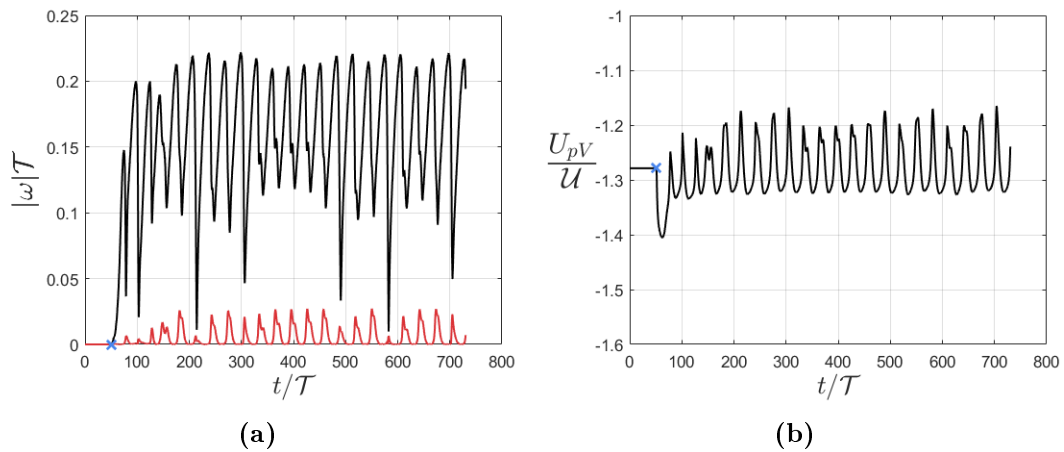


Figure 3.10 Results for case S200A ($Ga = 200$) similar to Figure 3.4.

Similar to case S178A (Figure 3.4), periodic velocity fluctuations are observed for S200A (Figure 3.10). The vertical particle velocity fluctuates between $U_{pV,min} = -1.1679\mathcal{U}$ and $U_{pV,max} = -1.3349\mathcal{U}$ over the time interval ranging from $t = 110\mathcal{T}$ to $685\mathcal{T}$, which means that the amplitude of the velocity fluctuations is $\frac{|U_{pV,max} - U_{pV,min}|}{2} = 0.0835\mathcal{U}$. A basic spectral analysis (using the Fourier transform) has been performed

to determine which frequency dominates the fluctuations of the vertical particle velocity and to possibly extract a frequency related to the expected oscillating motion (wake) of the particle. For this case, the analysis has been performed on the velocity fluctuation signal U'_{pV} between $t = 100\mathcal{T}$ and $t = 730\mathcal{T}$. In Figure 3.11 it can be seen that the largest amplitude of the Fourier transform is observed for a frequency $f = \frac{0.0333}{\mathcal{T}}$.

The number of times, between $t = 100\mathcal{T}$ and $t = 730\mathcal{T}$, that the particle approaches the wall over the vertical of the computational domain is 21 (based on Figure 3.12). This corresponds to a frequency $f = \frac{21}{730\mathcal{T}-100\mathcal{T}} = \frac{0.0333}{\mathcal{T}}$. Therefore, it can be concluded that the fluctuations of the vertical particle velocity are dominated by the interactions with the walls. The other peak in Figure 3.12 at $f = \frac{0.0651}{\mathcal{T}}$ is most likely related to the approaches of the particle between two adjacent walls (see Figure 3.9b) and could therefore not be related to the oscillating motion of the particle.

Similar to S178A, it should be noted that the peak amplitude in the Fourier transform does not match the amplitude of the velocity fluctuations in the time domain. This is probably due to spectral leakage.

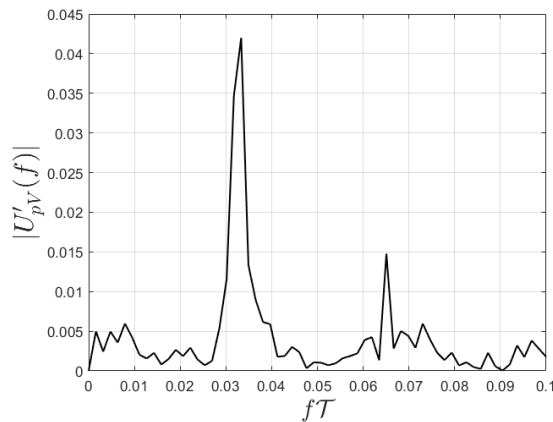


Figure 3.11 Single-sided amplitude spectrum of $U'_{pV}(t)$: the magnitude of the vertical particle velocity in the frequency domain $U'_{pV}(f)$ plotted against the frequency normalized by the characteristic time scale \mathcal{T} .

Similar to S178A it can be concluded from Figure 3.12 that both the vertical and horizontal velocity of the particle decreases each time it approaches a wall and increases when it moves away from the wall. Same reasoning as mentioned in Section 3.1.2.

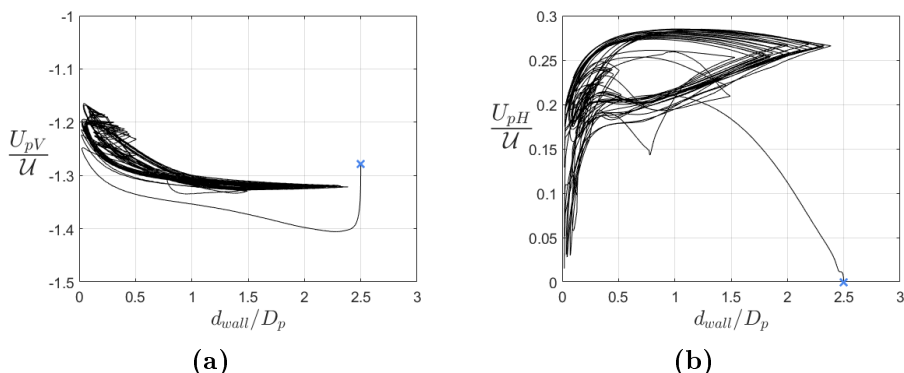


Figure 3.12 (a) The vertical particle velocity and (b) the horizontal particle velocity plotted against the distance to the nearest wall d_{wall} . The blue cross marks the particle's release. d_{wall} is defined by $d_{wall} = \min(x_c, L_x - x_c, y_c, L_y - y_c) - \frac{1}{2}D_p$.

3.1.4 Chaotic regime

In Figure 3.13 the results for the trajectory of the particle in the horizontal plane and the vertical position of the particle z_c in time are illustrated for case S250A.

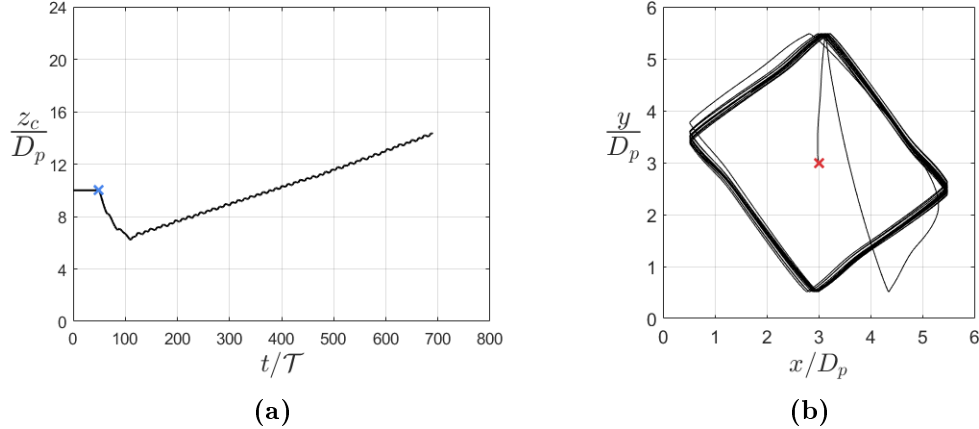


Figure 3.13 Results for case S250A ($Ga = 250$) (a) Temporal evolution of the vertical position of the particle z_c . The blue cross marks the particle's release. (b) Trajectory of a single sphere in the horizontal plane. The red cross marks the initial position of the particle.

For $Ga = 250$ a chaotic trajectory in the horizontal plane was expected, however Figure 3.13b shows a distinctive pattern. There is a lot of uncertainty in these results, since a single configuration is used to investigate S250A. Uhlmann and Dušek averaged over 7 simulation runs with an identical setup, but for each run a different velocity for the moving frame of reference was set. The investigation on this case is not further expanded, since it is not the main focus of this work.

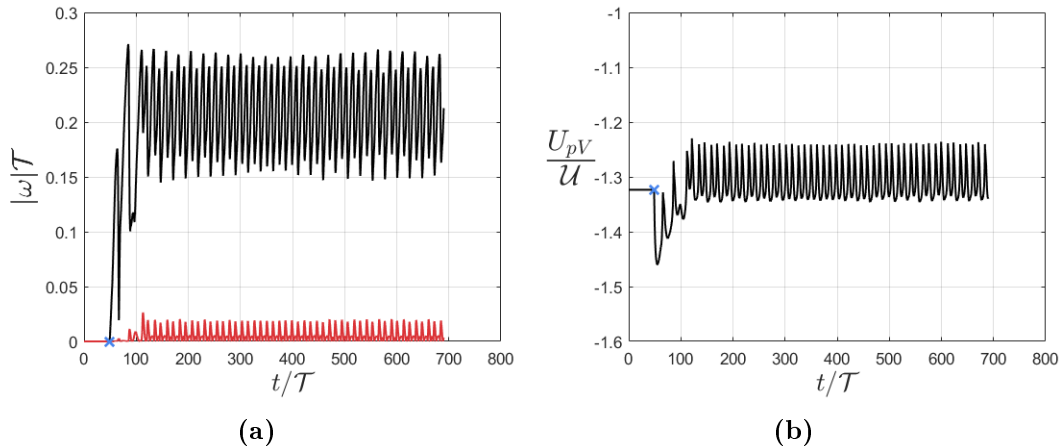


Figure 3.14 Results for case S250A ($Ga = 250$) similar to Figure 3.4.

Despite the for-mentioned the data for S250A is still analyzed. In Figure 3.14 it can be seen that the frequency of the fluctuations of the vertical particle velocity is much higher than the frequencies found in case S178A and S200A. A spectral analysis (Figure 3.15) for the vertical particle velocity fluctuations over the time interval between $t = 110\tau$ and $t = 685\tau$ has been performed. From this analysis the frequency characterizing these velocity fluctuations is found to be $f = \frac{0.0835}{\tau}$. The number of times the particle approaches the wall in this time interval is 47 (based on Figure 3.16). This corresponds to a frequency $f = \frac{47}{685\tau - 110\tau} = \frac{0.0817}{\tau}$, which roughly corresponds to the

frequency found with the spectral analysis. Similar to case S178A and S200A, it can be concluded that the fluctuations of the vertical particle velocity are dominated by the interactions with the walls. Additionally, note that over the for-mentioned time interval the vertical particle velocity fluctuates between $U_{pV,min} = -1.2296\mathcal{U}$ and $U_{pV,max} = -1.3462\mathcal{U}$, which means that the amplitude of the velocity fluctuations is $|\frac{U_{pV,max} - U_{pV,min}}{2}| = 0.0583\mathcal{U}$.

The terminal settling velocity of the particle $U_T = -1.3091\mathcal{U}$, which corresponds to a Reynolds number $Re_T = 327.28$.

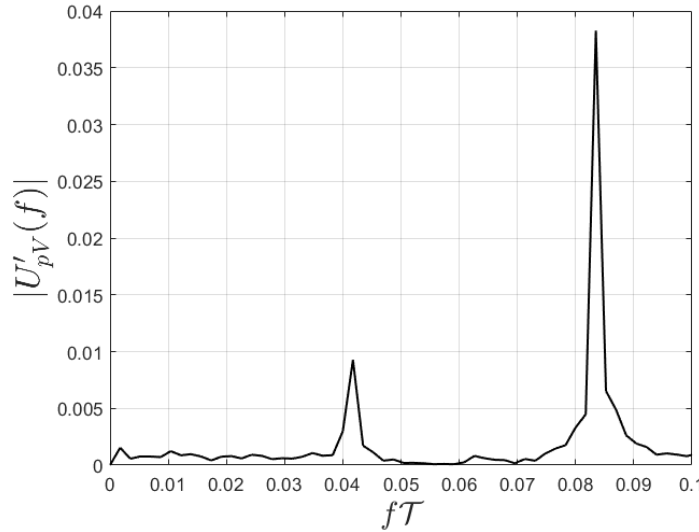


Figure 3.15 Single-sided amplitude spectrum of $U'_{pV}(t)$: the magnitude of the vertical particle velocity in the frequency domain $U'_{pV}(f)$ plotted against the frequency normalized by the characteristic time scale \mathcal{T} .

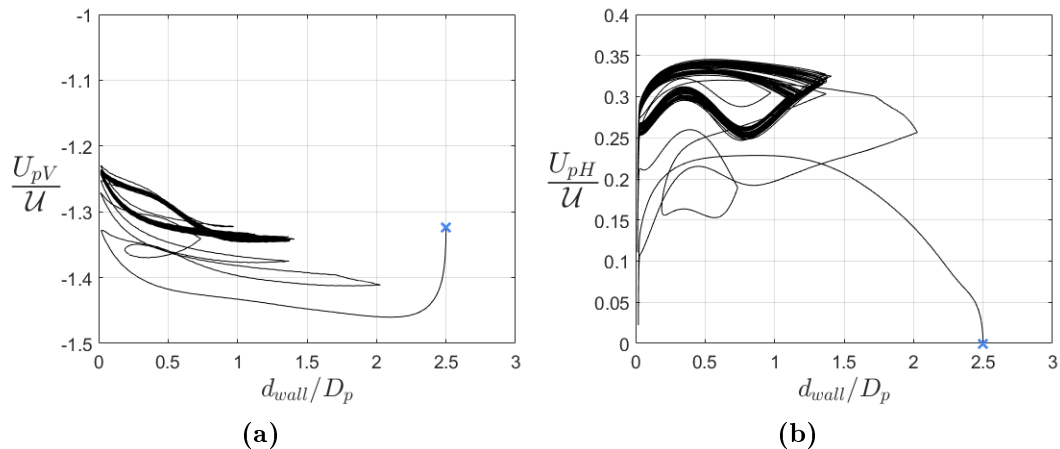


Figure 3.16 (a) The vertical particle velocity and (b) the horizontal particle velocity plotted against the distance to the nearest wall d_{wall} . The blue cross marks the particle's release. d_{wall} is defined by $d_{wall} = \min(x_c, L_x - x_c, y_c, L_y - y_c) - \frac{1}{2}D_p$.

3.1.5 Wall effects

In Figure 3.17 and 3.18 the results for the trajectory of the particle in the horizontal plane and the vertical particle velocity U_{pV} in time are illustrated for case S144B and S144C, respectively. From the figures below and figures displayed in Section 3.1.1 two observations could be made.

The first observation is the influence on the width of the tube ($= L_x$) on the terminal settling velocity of the particle U_T . When the width of the tube increases the vertical particle velocity increases, see Figure 3.19. Note that the terminal settling velocity of the particle $U_T = -1.2859\mathcal{U}$ for S144B and $U_T = -1.2903\mathcal{U}$ for S144C, which corresponds to $Re_T = 185.17$ and $Re_T = 185.80$, respectively.

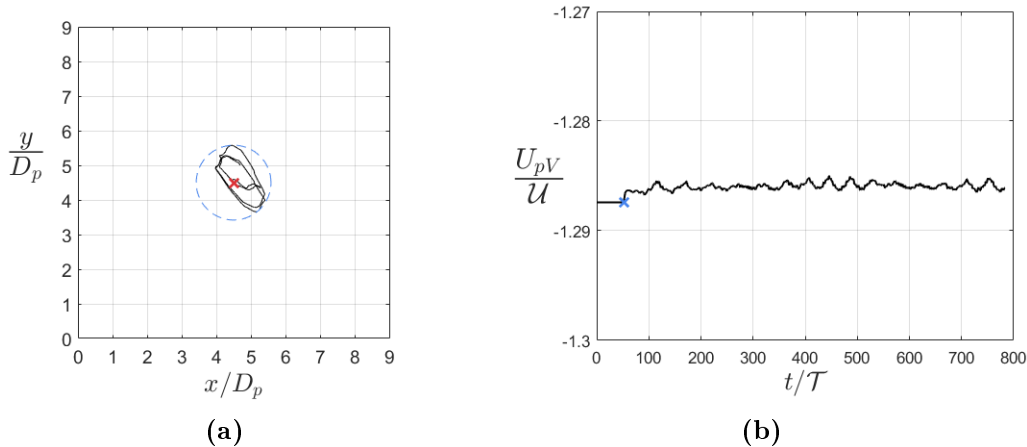


Figure 3.17 Results for case S144B ($Ga = 144$) (a) Trajectory of a single sphere in the horizontal plane. The red cross marks the initial position of the particle and the blue dashed line indicates the region of motion. (b) Temporal evolution of the vertical particle velocity U_{pV} . The blue cross marks the particle's release.

Figure 3.19 also contains the graphical representation of Equation B.8 for three different values of $U_{T,free}$ to check whether this equation could be used as a crude estimator to determine the terminal settling velocity of a sphere in a rectangular duct:

- $U_{T,free} = -1.2810\mathcal{U}$: based on Morison's equation (Appendix B.1).
- $U_{T,free} = -1.2920\mathcal{U}$: based on highly-accurate spectral/spectral-element simulations by Uhlmann and Dušek [6].
- $U_{T,free} = -1.2975\mathcal{U}$: fitted on the simulation data in this work.

The curves in Figure 3.19 show that Equation B.8 could be used as a crude estimator to determine the terminal settling velocity of a sphere in a rectangular duct provided that the value for the terminal settling velocity of a sphere in free space $U_{T,free}$ is set correctly.

The other observation focuses on the motion of the particle in the horizontal plane. Recall that for S144A the radius of the region of motion for S144A is $r_{motion} = 0.7641D_p$. Which is $r_{motion} = 1.0800D_p$ and $r_{motion} = 1.9264D_p$ for case S144B and S144C, respectively. This means that the radius of the region of motion increases for wider channels. This result could indicate that besides the fact that a narrow tube suppresses the vertical particle velocity more than a wider tube, it also suppresses

the motion of the particle in the horizontal plane. Since the distance between the particle and the wall is relatively large, it is suggested that a lift force related to the irrotational (or potential) flow theory is influencing the horizontal motion of the particle.

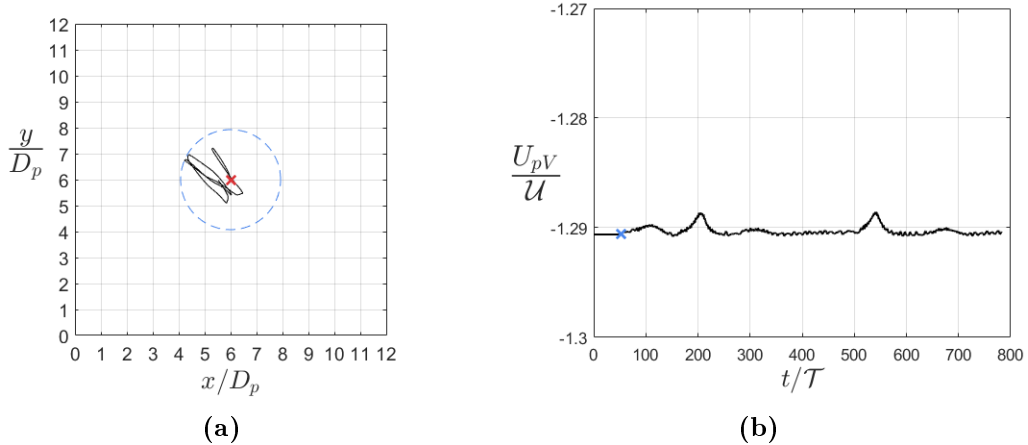


Figure 3.18 Results for case S144C similar to Figure 3.17.

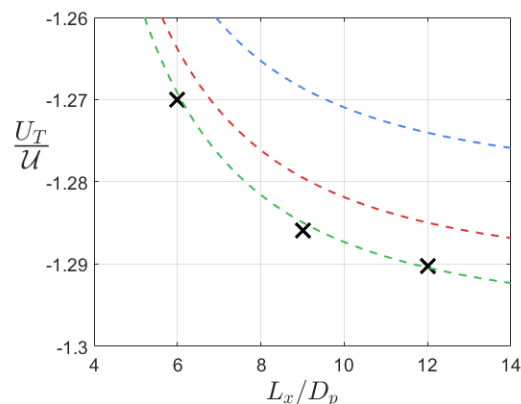


Figure 3.19 The vertical particle velocity plotted against the width of the tube ($= L_x$) for $Ga = 144$. The simulation results are indicated by the black crosses. The dashed lines correspond to Equation B.8 with $U_{T,free} = -1.2810\mathcal{U}$ (blue), $U_{T,free} = -1.2920\mathcal{U}$ (red) and $U_{T,free} = -1.2975\mathcal{U}$ (green).

3.2 Two particles

In this section the results regarding the sedimentation of two spheres are presented. As a first step a qualitative analysis is performed by means of a code written in MATLAB®. This code makes it possible to visualize the entire simulation in the 3D domain. Comparison of the results regarding the *drafting-kissing-tumbling* phenomenon is difficult, since other studies (numerical and experimental) covering this subject mainly report the occurrence of the phenomenon, rather than quantify the dynamics accompanying the DKT phenomenon. In this section it is therefore chosen to describe the results qualitative and (if possible) quantify the dynamical features.

3.2.1 Steady vertical regime

Case T144 corresponds to the sedimentation of two particles with $Ga = 144$. The behaviour of both particles in case T144 can be summarized by Figure 3.20, which displays the coordinates of both particles as a function of time. In the figure the anticipated DKT phenomenon is clearly observed after the particles are released at $t = 0$. The velocity of the moving frame of reference outperforms the vertical particle velocity initially, since the particles have not reached their terminal velocity yet, causing the particles to move upwards in the computational domain. As a result of the DKT the particles interchange their role, so that the leading particle becomes the trailing particle and vice versa. After the tumbling stage the particles drift to opposite corners in the computational domain and remain there for the remainder of the simulation, while falling with a constant vertical velocity.

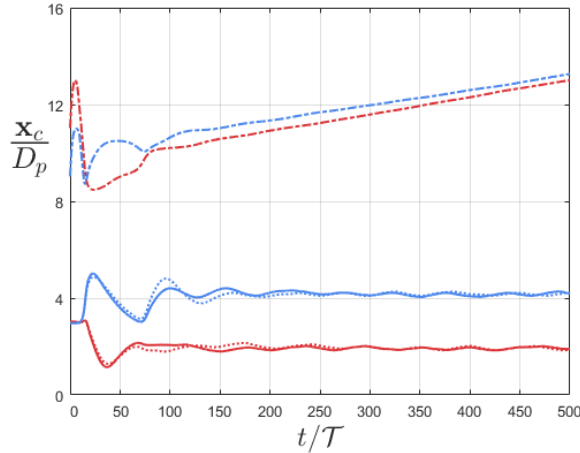


Figure 3.20 Position of the particle centroid ($\mathbf{x}_c = \langle x_c, y_c, z_c \rangle$) plotted against time for both particles. The coordinates of particle 1 and 2 are indicated with the red and blue lines, respectively. x_c : solid lines(-), y_c : dotted lines(:) and z_c : dash-dotted lines(-).

Since the two particles fall independently in the computational domain for the remainder of the simulation a greater hindered settling effect is expected and therefore a lower magnitude of the vertical particle velocity. This is confirmed by Figure 3.21, since both particles have a lower vertical particle velocity compared to a single sphere (case S144A). If the vertical particle velocity is averaged over a time interval $t = 200\mathcal{T}$ to $t = 1000\mathcal{T}$, one obtains a terminal settling velocity of both particles of approximately $U_T \approx -1.23\mathcal{U}$.

Also note that there is a significant increase in the vertical particle velocity of both particles during the DKT process .

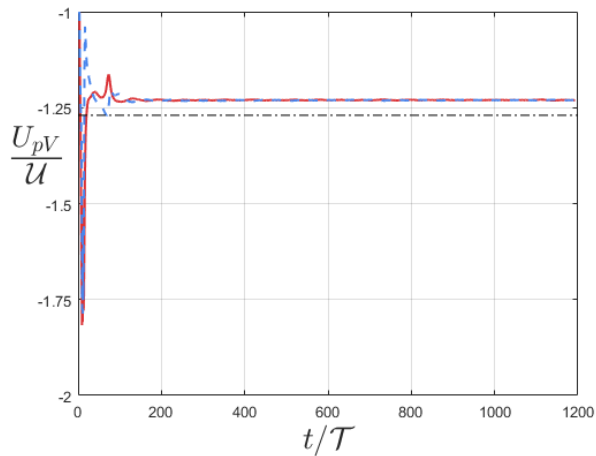


Figure 3.21 Temporal evolution of the vertical particle velocity for both particles in case T144. The red solid line(-) and the blue dashed line(--) indicate particle 1 and 2, respectively. The black dash-dotted line(-.) indicates the terminal settling velocity of a single particle (case S144A) and is added for comparison.

3.2.2 Steady oblique regime

T178 is an interesting case, since it involves the Galileo number $Ga = 178$, which has been extensively studied by Uhlmann and Doychev [7] for a single and multiple particles. In their work they suggest that wake attraction, in the sense of drafting-kissing-tumbling, is the key mechanism of particle cluster formation. Figure 3.22 shows the vertical position of the two spheres during the simulation. This figure contains two time intervals labelled ‘1’ and ‘2’, which will be further discussed below.

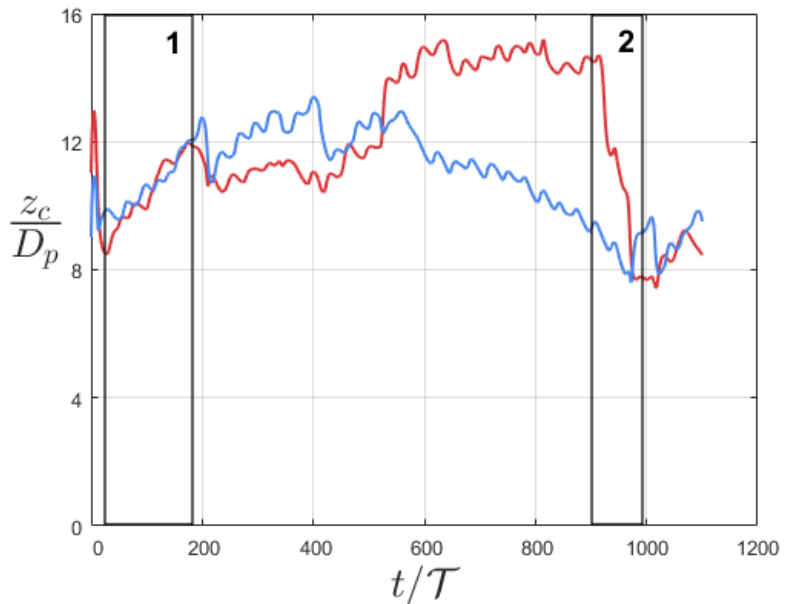


Figure 3.22 Temporal evolution of the vertical particle position for both particles in case T178. The red and blue solid line indicate particle 1 and 2, respectively.

Interval 1

Although Figure 3.22 suggests that the DKT phenomenon occurs multiple times in rapid succession, observing an animation of the simulation created with MATLAB® provides us with different insights: The DKT process was never observed during this time interval, nor do the particles collide in a horizontal manner. Instead, the two particles move independently in the domain. The animation also reveals that after $t = 1030\mathcal{T}$ no DKT occurs.

Interval 2

In contrast to box 1, this time interval shows interesting results regarding the wake attraction between the particles. The particles move around in the computational domain at different heights in the time prior to interval 2. At $t \approx 915\mathcal{T}$ particle 1 starts descending, this point marks the initiation of the drafting stage. Beyond $t = 915\mathcal{T}$ the trailing particle (particle 1) moves towards the leading particle (particle 2), this is the drafting stage. After the drafting stage, the particles kiss at $t \approx 971\mathcal{T}$. The unstable configuration of the particles during the kissing stage causes the particles to tumble ($t \approx 978\mathcal{T}$) and subsequently the particles repel each other and swap their vertical positions in the domain.

In Figure 3.23 the three stages of the DKT phenomenon are displayed. The iso-surfaces in the plots indicate the second largest eigenvalue (λ_2) of the tensor $\mathbf{S}^2 + \boldsymbol{\Omega}^2$, where \mathbf{S} and $\boldsymbol{\Omega}$ are the symmetric and anti-symmetric parts of the velocity gradient $\nabla \mathbf{u}$. Vortex structures can be identified as the connected region where λ_2 is negative, hence this is known as the λ_2 -method. This method, which has been extensively studied by Jeong and Hussain [25], gives insights in the wake structures of the sedimenting particles. The iso-surfaces in Figure 3.23 indicate the regions where $\lambda_2 = -0.015$.

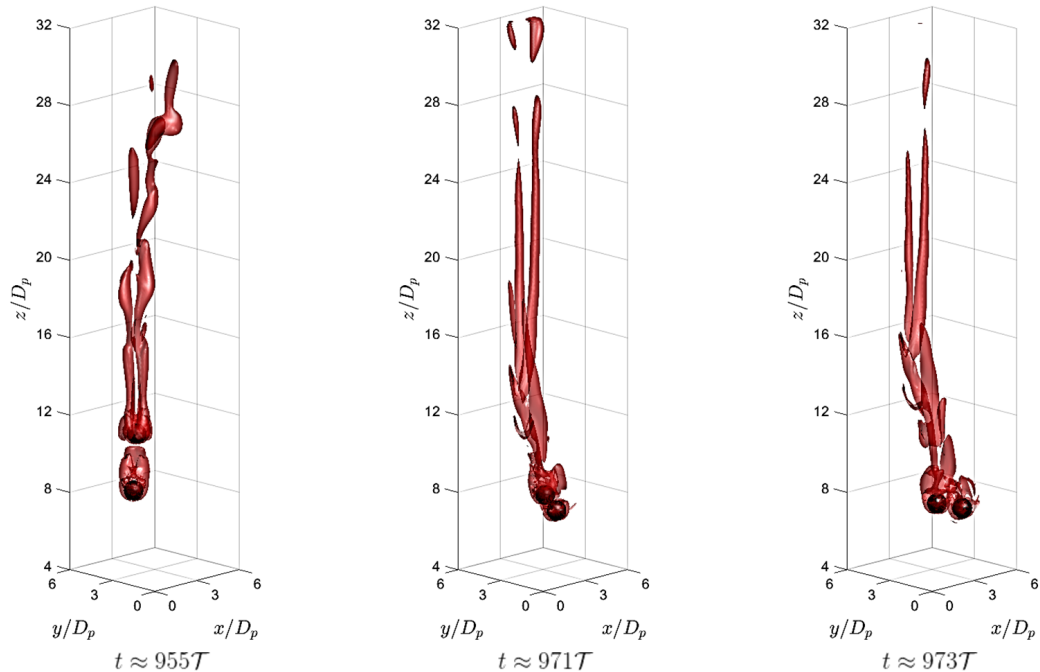


Figure 3.23 The DKT phenomenon seen in case T178 between $t = 900\mathcal{T}$ and $t = 1000\mathcal{T}$. From left to right: drafting, kissing, tumbling. The red iso-surface highlights the region where $\lambda_2 = -0.015$.

The initiation of the DKT process at $t \approx 915\mathcal{T}$ and not before this time could be related to the vertical alignment of the particles and the direction of motion in the horizontal plane. When observing the 3D animation of the simulation it is clear that the wake attraction starts (the drafting stage) as soon as the particles are almost vertically aligned and both particles move in the same direction in the horizontal plane. This observation is supported by Figure 3.24a, where the horizontal coordinates of the particle centroid (x_c and y_c) are plotted against the time between $t = 900\mathcal{T}$ and $t = 1000\mathcal{T}$.

Note that the particles are a considerable length apart at the onset of the drafting stage. This distance amounts roughly 5 particle diameters. Figure 3.24b shows both particles and their wake structure at $t \approx 915\mathcal{T}$. It can be seen that the wake of the leading particle interacts with the trailing particle over a distance of roughly $5D_p$. This length was also reported by Fortes et al.[8].

Also take note of the double-threaded structure of the wake. This wake structure is similar to the wake structure reported in the paper of Uhlmann and Dušek [6] for the same Galileo number.

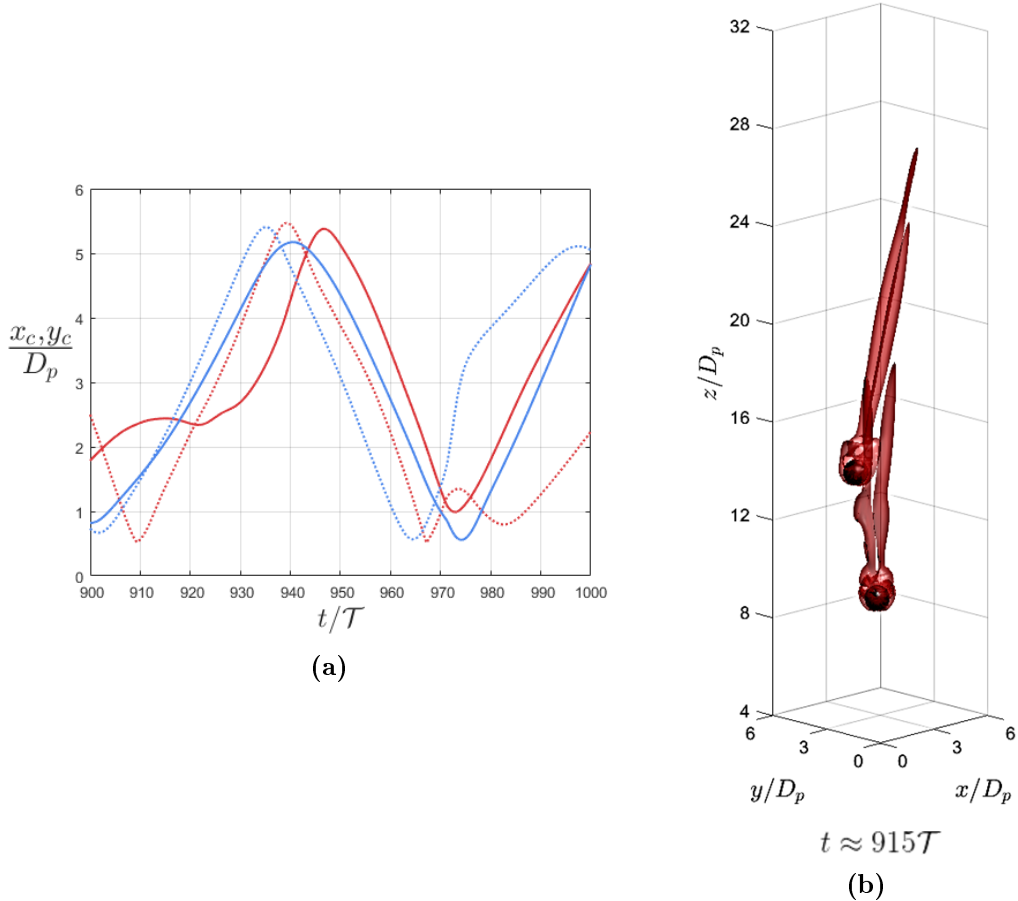


Figure 3.24 (a) Temporal evolution of the horizontal particle positions, x_c (solid lines) and y_c (dotted lines), for both particles on the time interval between $t = 900\mathcal{T}$ and $t = 1000\mathcal{T}$. The red and blue lines indicate particle 1 and 2, respectively.
(b) The DKT onset at $t \approx 915\mathcal{T}$. The red iso-surface highlights the region where $\lambda_2 = -0.015$.

Figure 3.25 shows the vertical particle velocity of both particles. It can be seen that at some time instances the vertical particle velocity of both particles significantly exceeds the vertical velocity of a single particle (case S178A). These instances are around $t = 200\tau, 400\tau, 500\tau, 900\tau$. When looking at Figure 3.22 it can be seen that at these times the particles interact with each other in the form of wake-trapping between the trailing and leading particle or DKT (see Figure 3.23). Also note the time instances in the plot where vertical particle velocity is much less than the vertical velocity of a single particle. This corresponds to the end of the tumbling stage, where the leading particle is ‘catapulted’ upwards so it becomes the trailing particle. The small velocity fluctuations seen in the plot could not be analyzed by means of a spectral analysis, since the signal contains too much noise. It is expected that these small fluctuations are related to the particle-wall interaction as observed for a single particle (see Section 3.1.2).

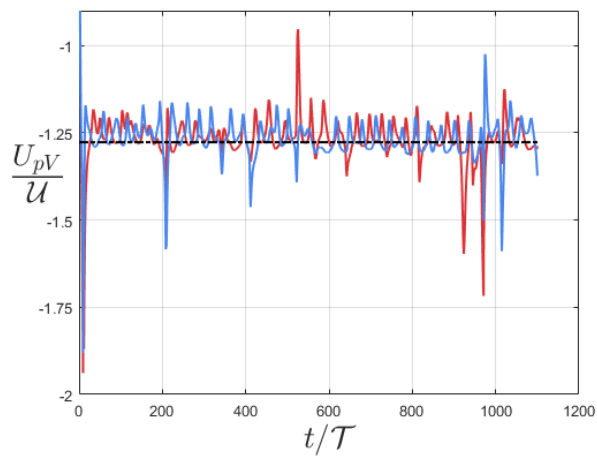


Figure 3.25 Temporal evolution of the vertical particle velocity for both particles in case T178. The red and blue line indicate particle 1 and 2, respectively. The black dash-dotted line(-.) indicates the terminal settling velocity of a single particle (case S178A) and is added for comparison.

3.2.3 Oblique oscillating regime

In Figure 3.26 and by visual inspection it is seen that the particles interact with each other on the time interval between $t = 0$ and $t = 300\tau$. During this time interval the particles repeatedly experience drafting-kissing-tumbling. Similar to T178, the DKT process initiates when the particles are almost vertically aligned and they have a similar direction of motion in the horizontal plane. It is difficult to show the direction of the particles as clearly as Figure 3.24a, because the DKT process occurs several times in a relatively short time interval.

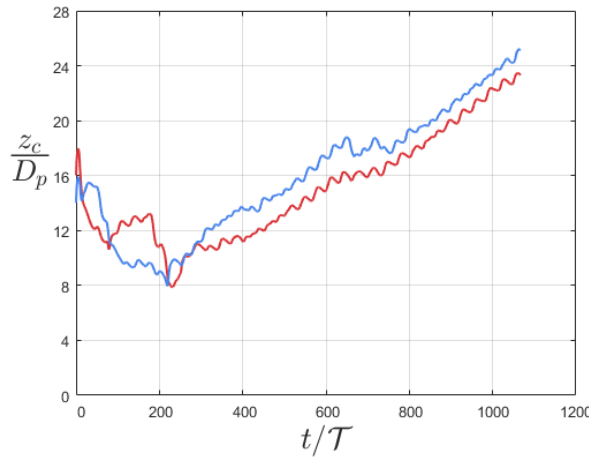


Figure 3.26 Temporal evolution of the vertical particle position for both particles in case T200. The red and blue solid line indicate particle 1 and 2, respectively.

Figure 3.27 shows the vertical particle velocity of both particles. The behaviour is similar to T178 and is explained in Section 3.2.2.

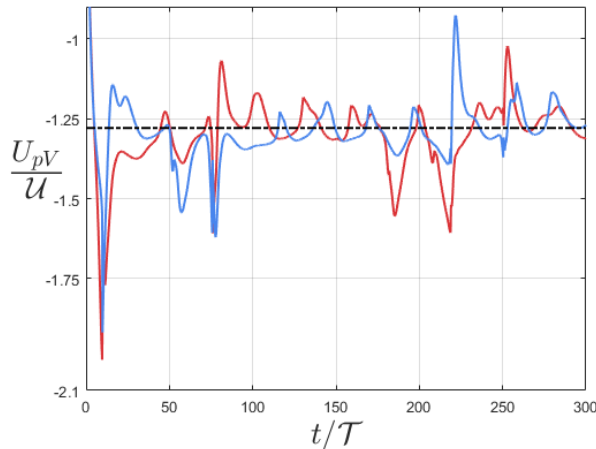


Figure 3.27 Temporal evolution of the vertical particle velocity for both particles in case T200. The red and blue line indicate particle 1 and 2, respectively. The black dash-dotted line(-.) indicates the terminal settling velocity of a single particle (case S200A) and is added for comparison.

3.2.4 Chaotic regime

This case is not extensively elaborated, since $Ga = 250$ is not the main focus of this work. However, one interesting observation is made regarding the trajectories of the particles. Similar to S250A the paths of both particles are predictable instead of chaotic. In Figure 3.28 the position of both particle centroids are plotted against time. From this plot it could be argued that this case was not simulated long enough, since a different trajectory is observed after $t = 800\mathcal{T}$, which could suggest a change in dynamical behaviour. Another explanation could be that the particles show interaction with each other for the second time in the entire simulation (the first time is right after the start of the simulation).

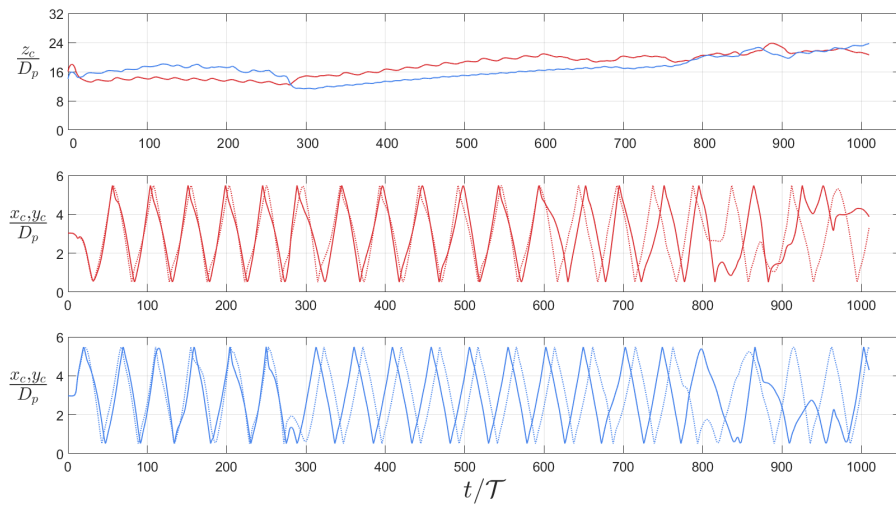


Figure 3.28 Position of the particle centroid plotted against time for both particles. The upper plot shows the vertical position z_c of both particles. The middle and lower plot show the coordinates x_c and y_c of particle 1 and 2, respectively. x_c : solid lines(-), y_c : dotted lines(:).

3.3 Multiple particles

This section focuses mainly on the results regarding the settling velocity of the suspensions with solid-volume fractions Φ . Equations 3.7-3.10 are defined to avoid confusion in terms of terminology.

The average of a particle-related quantity $\mathcal{Q}(t)$ over all particles is defined by

$$\overline{\mathcal{Q}_p}(t_m) = \langle \mathcal{Q}_p \rangle_p(t_m) = \frac{1}{N_p} \sum_{i=1}^{N_p} \mathcal{Q}_p^i(t_m), \quad \text{for all } m \in [1, N_t] \quad (3.7)$$

And the time average for that quantity $\mathcal{Q}(t)$ is

$$\langle \mathcal{Q} \rangle_t = \frac{1}{N_t} \sum_{m=1}^{N_t} \mathcal{Q}(t_m) \quad (3.8)$$

The combination of Equation 3.7 and 3.8 is denoted by $\langle \mathcal{Q}_p \rangle_{p,t}$, which is the mean over all particles and time.

The auto-correlation function (ACF) for the vertical particle velocity is used to determine whether enough time steps were used in order for the suspensions to settle. In general the ACF for a quantity $\mathcal{Q}(t)$ is defined as

$$R_{QQ}(\tau_{lag}) = \frac{\langle \mathcal{Q}'(t) \mathcal{Q}'(t + \tau_{lag}) \rangle_{p,t}}{\langle \mathcal{Q}'(t) \mathcal{Q}'(t) \rangle_{p,t}} \quad (3.9)$$

Where $\mathcal{Q}'(t) = \mathcal{Q}(t) - \langle \mathcal{Q} \rangle_t$ is the fluctuation of the quantity and τ_{lag} the lag time.

From the auto-correlation function for the vertical particle velocity, a time step N_{start} could be determined where the vertical particle velocity fluctuations become decorrelated, i.e. $R_{QQ} = 0$. The settling velocity of the suspension U_S is then defined as

$$U_S = \langle U_{pV} \rangle_{p,t}, \quad \text{for all } m \in [N_{start}, N_t] \quad (3.10)$$

Case M144A, M178A and M200A ($\Phi = 5.1 \cdot 10^{-3}$) have been chosen to determine the time step N_{start} where the vertical particle velocity fluctuations become decorrelated, since their velocity signal shows the largest fluctuations (see Figure 3.30, 3.37, 3.44). The auto-correlation functions of the vertical particle velocity for M144A, M178A and M200A are shown in Figure 3.29.

From this figure it is determined that the vertical particle velocities become decorrelated after $t = 200\mathcal{T}$. This means the settling velocity of the suspension U_S is based on the time interval between $t = 200\mathcal{T}$ and $t = 900\mathcal{T}$ for all cases.

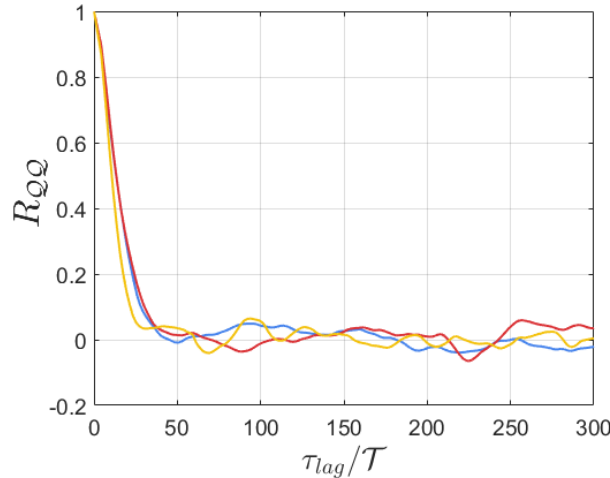


Figure 3.29 The auto-correlation functions of the vertical particle velocity U_{pV} as a function of the lag time τ_{lag} for M144A (blue line), M178A (red line) and M200A (yellow line).

3.3.1 Steady vertical regime

In Figure 3.30 the average particle settling velocity $\overline{U_{pV}}$ has been plotted against time for all cases (M144A-M144G). First of all the anticipated hindered settling effect is clearly observed, because it can be seen in this figure that the average particle settling velocity decreases with increasing solid-volume fraction Φ . Also, a difference in fluctuation level between the dilute and dense suspensions is observed: the fluctuations of the average particle settling velocity are larger for the dilute cases compared to the dense cases.

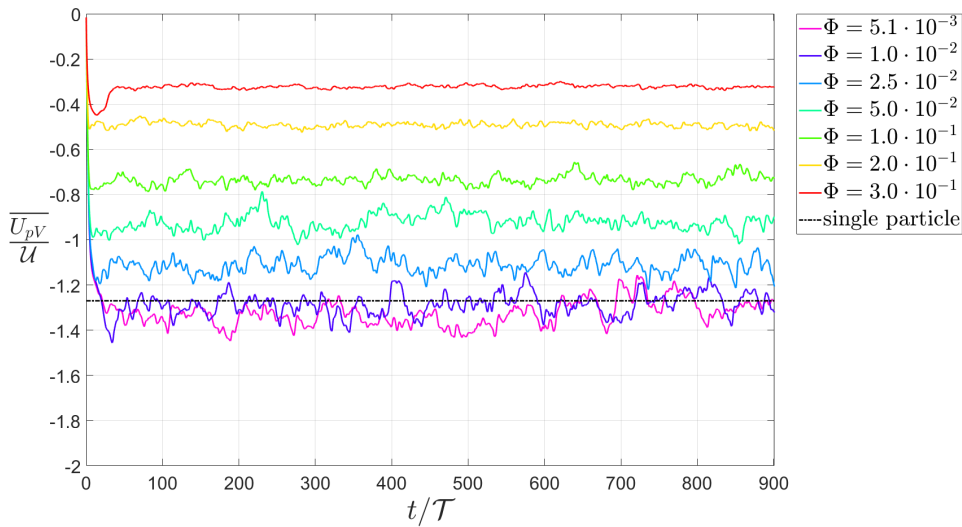


Figure 3.30 The average particle settling velocity plotted against time for all cases (all solid-volume fractions Φ). The black dashed-dotted line represents the vertical particle velocity of a single sphere U_T (case S144A).

Figure 3.31 shows the settling velocity of the suspension plotted against the solid-volume fraction. From this plot it can be determined that the settling velocity of the suspensions with $\Phi = 5.1 \cdot 10^{-3}$ and $\Phi = 1.0 \cdot 10^{-2}$ are increased by 4.1% and 1.2% compared to the value of a single particle. Additionally, this figure could imply

that the hindered settling effect observed by Richardson and Zaki comes into effect for solid-volume fractions $\Phi \gtrapprox 0.01$.

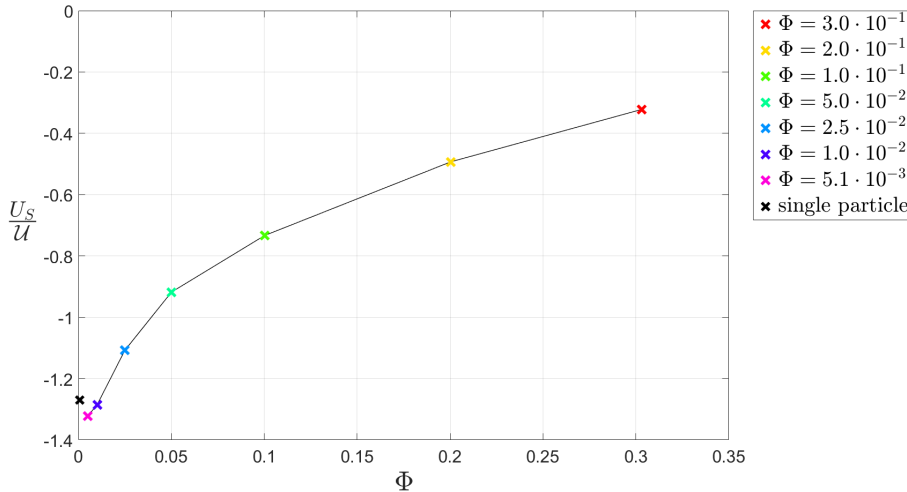


Figure 3.31 The settling velocity of the suspension plotted against the solid-volume fraction for all cases (all solid-volume fractions Φ). The black cross represents the terminal settling velocity of a single particle U_T (case S144A).

Similar to Richardson and Zaki [1] it is interesting to see if there exists a constant exponent n that relates U_S and Φ according to Equation 1.2.

Equation 1.2 could be rewritten, so that

$$\log U_S(\Phi) = n \log(1 - \Phi) + \log U_T \quad (3.11)$$

It can be seen in Figure 3.32 that n is not constant, since no straight line is observed in this plot. This means n does not solely depend on the particle Reynolds number Re_p and the ratio $\frac{D_p}{L_x}$ (or $\frac{D_p}{D_t}$), but also on the solid-volume fraction Φ itself.

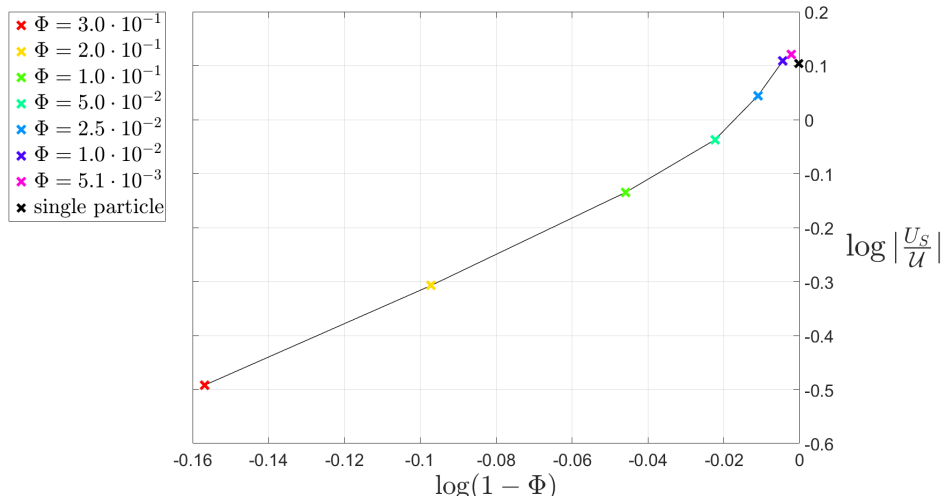


Figure 3.32 $\log |U_S/U|$ vs. $\log(1 - \Phi)$ for $Ga = 144$. The black cross indicates the terminal settling velocity of a single particle U_T .

In Figure 3.33 the distribution of the vertical particle velocity (normalized by the velocity of a single particle) is displayed for three different solid-volume fractions. The three solid-volume fractions are: $\Phi = 5.1 \cdot 10^{-3}$ (most dilute suspension), $\Phi = 5.0 \cdot 10^{-2}$ (a semi-dilute suspension) and $\Phi = 3.0 \cdot 10^{-1}$ (most dense suspension). The velocity distributions of the other solid-volume fractions are appended in Appendix E.1. Note that the distribution of the vertical particle velocity is indicated by the normalized histogram, so that it displays the estimate of the probability density function (PDF) for the vertical particle velocity. The red line, added in the graphs, is a Gaussian (normal) distribution with a mean and standard deviation based on the vertical particle velocity simulation data of all particles. Also note that the simulation data, used to determine these distributions, is taken between $t = 200\mathcal{T}$ and $t = 900\mathcal{T}$.

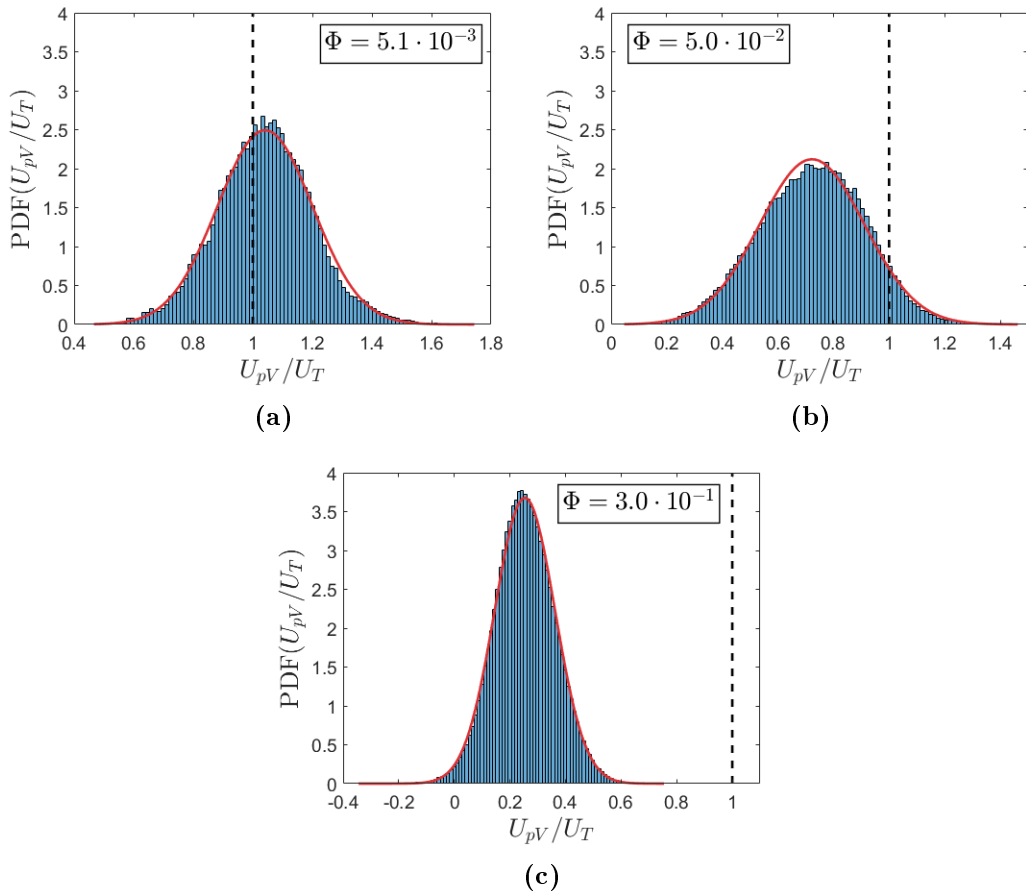


Figure 3.33 Distribution of the vertical particle velocity for $Ga = 144$ and (a) $\Phi = 5.1 \cdot 10^{-3}$, (b) $\Phi = 5.0 \cdot 10^{-2}$ and (c) $\Phi = 3.0 \cdot 10^{-1}$. The black dashed line indicates the settling velocity of a single sphere and the red line indicates the Gaussian distribution with a mean and standard deviation based on the vertical particle velocity simulation data.

A priori, A non-Gaussian distribution was expected for the dilute suspensions ($\Phi = 5.1 \cdot 10^{-3}$ and $\Phi = 1.0 \cdot 10^{-2}$), because the settling velocity of the suspension is higher compared to the velocity of a single particle. When this increase is due to particle interaction (such as DKT), a different distribution of the vertical particle velocity is expected compared to the case when the same particles do not interact with each other. Therefore, a non-Gaussian distribution, similar to distributions seen in Figure 1.7, was expected. The for-mentioned suggests that particle clustering is present, which could be due to wake trapping (drafting) or DKT.

However, from Figure 3.33 it can be concluded that the vertical particle velocity is by approximation normally distributed for all solid-volume fractions. This means it can not be determined, based on this statistic, if particle clustering occurs for the solid-volume fractions $\Phi = 5.1 \cdot 10^{-3}$ and $\Phi = 1.0 \cdot 10^{-2}$.

Further investigation on the possibility of particle clusters being present in the simulations for the dilute suspensions brings us to an interesting spatial parameter θ , which is the angle of a particle with its nearest neighbouring particle and the vertical; see the sketch in Figure 3.35h. The distribution of the angle θ is plotted for all solid-volume fractions in Figure 3.35. To compare the data, a probability density function of the angle θ for a set of non-interacting particles, randomly distributed in an arbitrary volume, has to be specified. For such a set of random distributed particles (RDP), it can be theoretically derived that the PDF of the angle θ is given by $\text{PDF}_{RDP} = \frac{1}{2}\sin(\theta)$, where $\theta \in [0, \pi]$. This PDF is used as a reference and it shows that the particles in the simulations interact with each other for low solid-volume fraction as their statistics (see Figure 3.35) strongly differ from that of random distributed particles: A clear increase is observed for $\theta < 30^\circ$ (or $\theta > 150^\circ$). This means particles are found to align vertically more than a set of random distributed particles. This enables particles to enter the wake of leading particles, which results in the formation of particle clusters, hence the increase in the settling velocity of clustered particles compared to a single particle settling individually. This hypothesis is supported by Figure 3.34, where a top view on the computational box for $Ga = 144$ and $\Phi = 5.1 \cdot 10^{-3}$ is shown for several time instances and Figure 3.36, where DKT is observed for the same case.

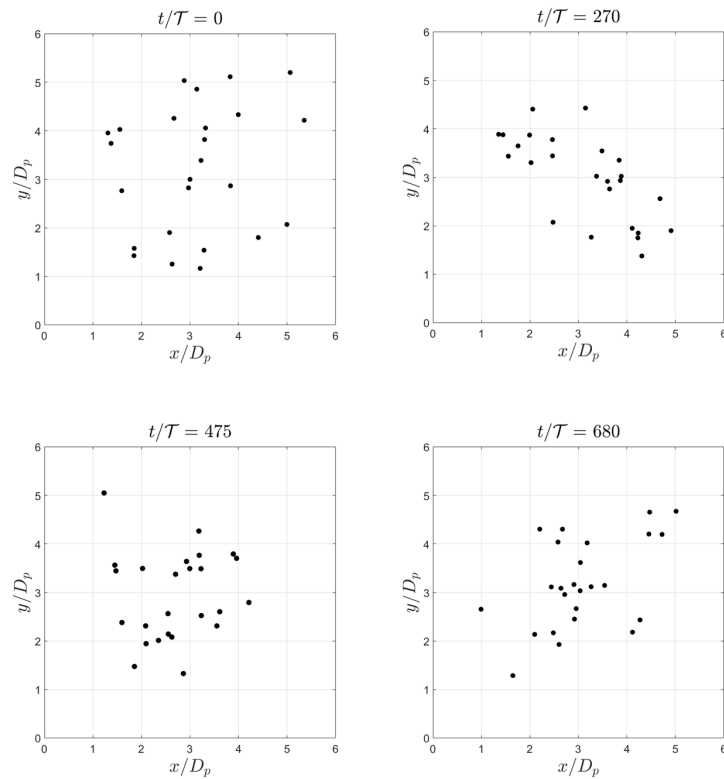


Figure 3.34 Particle locations seen from the top of the computational domain for several time instances for case M144A ($Ga = 144$ and $\Phi = 5.1 \cdot 10^{-3}$). It is observed that the particles align vertically more for different instances in time than the initial setup ($t = 0\mathcal{T}$).

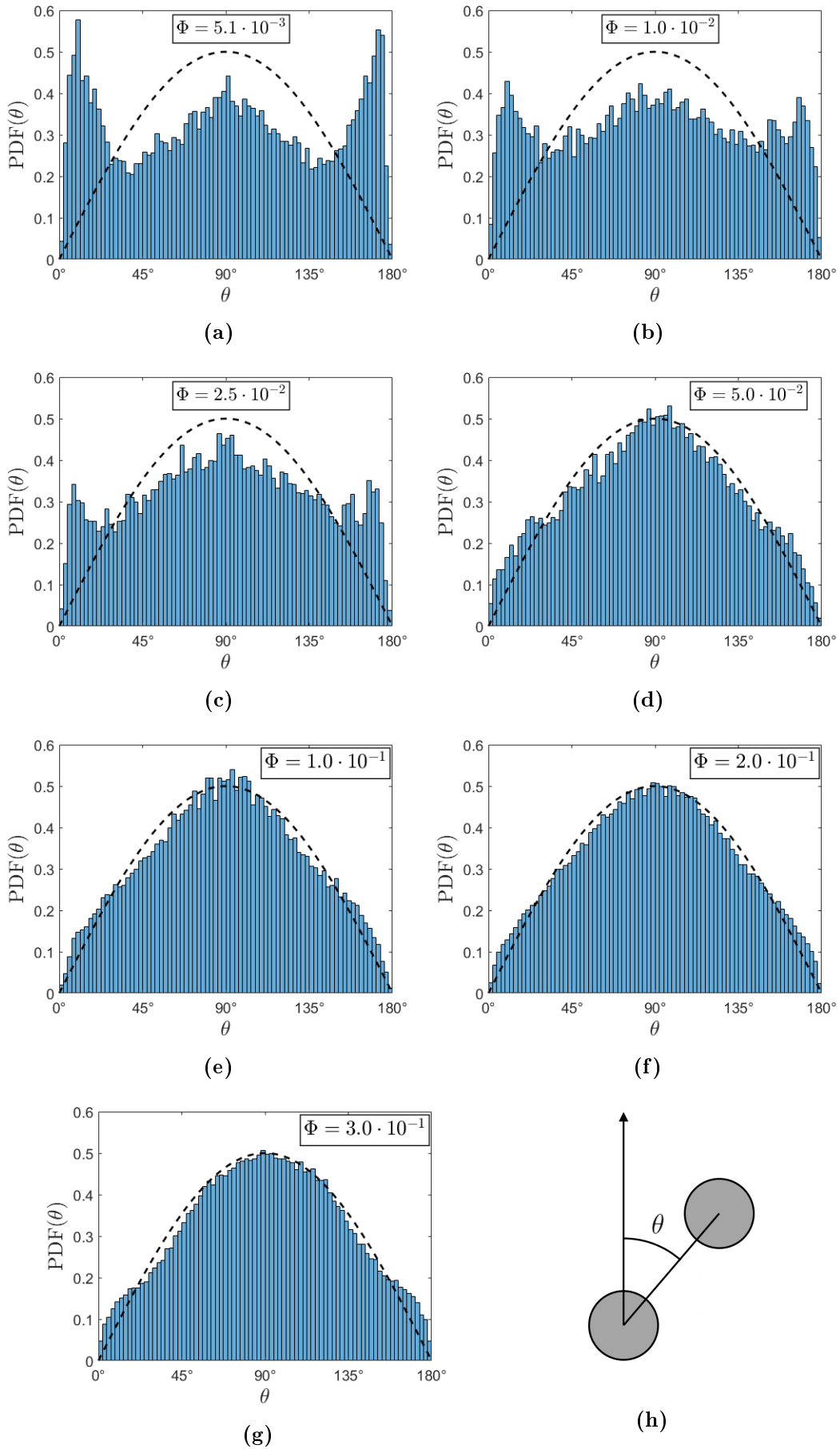


Figure 3.35 Distribution of the angle θ for $Ga = 144$ and all solid-volume fractions. The black dashed line indicates the PDF for random distributed particles PDF_{RDP} . Notice the increase for $\theta < 30^\circ$ (or $\theta > 150^\circ$) for the dilute suspensions (low Φ). (h) The basic principle of the angle θ .

From Figure 3.35 it can be seen that for increasing solid-volume fraction Φ , the statistic regarding the angle θ is starting to look more like that of random distributed particles. This could indicate that as the solid-volume fraction increases, particle clustering vanishes and other interactions occur. Besides the two most dilute concentrations, the distribution of θ for $\Phi = 2.5 \cdot 10^{-2}$ also indicates that the particles tend to align vertically. However, an increase in the settling velocity was not observed, this is probably attributed to the hindered settling effect.

Regarding Figure 3.33 it can be argued, that the statistics involving the distribution of the vertical particle velocity are not decisive when identifying particle clustering, i.e. a Gaussian distribution of the vertical particle velocity does not necessarily mean that particles do not cluster.

The results, described in this section, confirm the findings by Huisman et al.[15], who also observed mild clustering in their experiments for the steady vertical regime ($Ga = 110$) at even lower solid-volume fractions. Note that in the studies of Uhlmann and Doychev [7] no significant increase in the settling velocity of the suspension was observed nor the formation of clusters for $Ga = 121$ in a triply periodic computational box. The clustering of particles, resulting in an increase of the settling velocity of the suspension, might be explained by the presence of intrinsic convection, which could occur for multiple particles settling in a confined geometry.

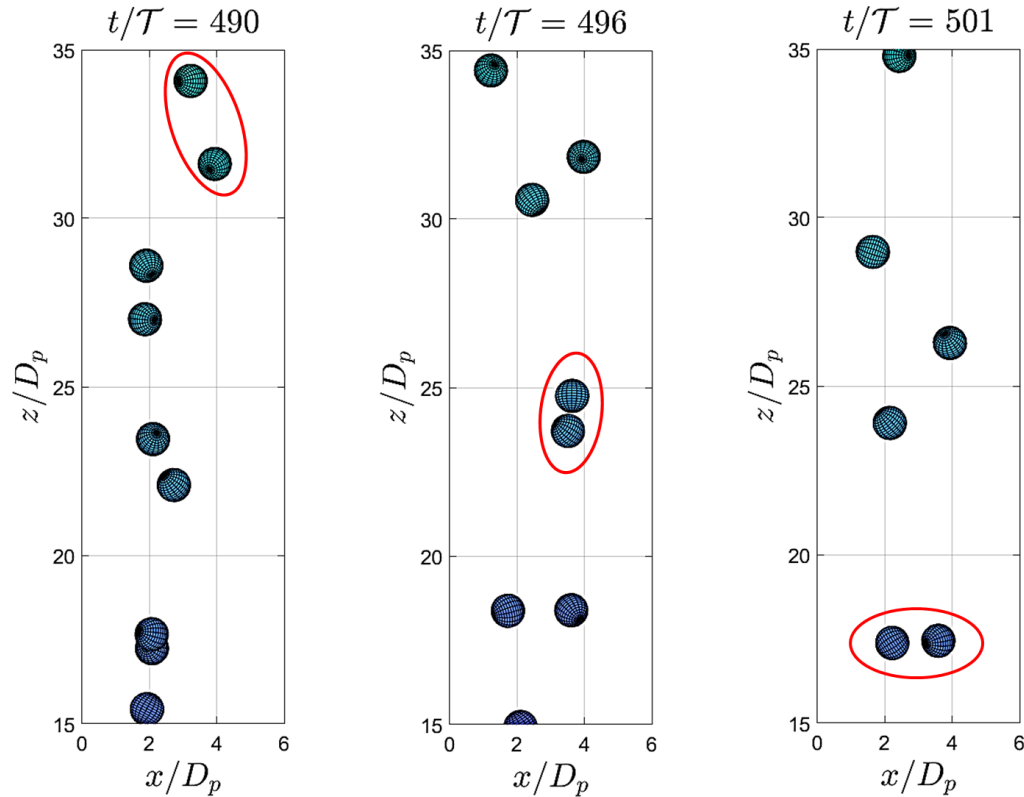


Figure 3.36 From left to right: Drafting, kissing, tumbling. One of many instances of DKT seen in the simulations for case M144A ($Ga = 144$ and $\Phi = 5.1 \cdot 10^{-3}$).

3.3.2 Steady oblique regime

In Figure 3.37 the average particle settling velocity $\overline{U_{pV}}$ has been plotted against time for all cases (M178A-M178G). Similar to the steady vertical regime, the anticipated hindered settling effect is clearly observed and the fluctuations of the average particle settling velocity are larger for the dilute cases compared to the dense cases.

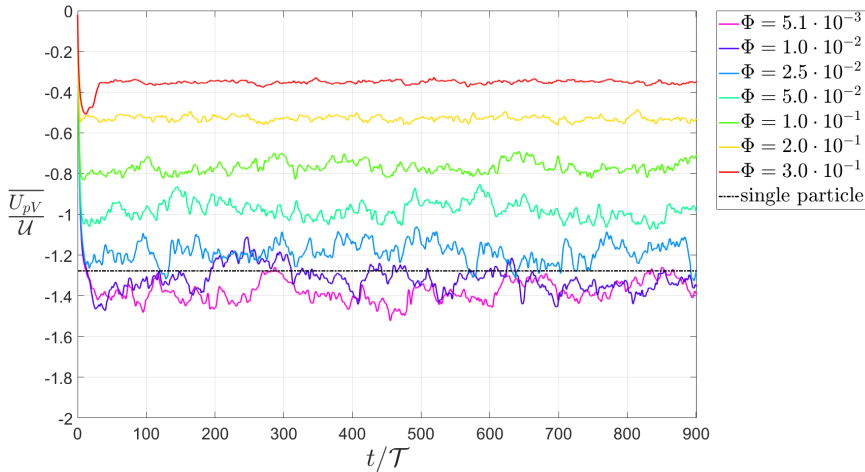


Figure 3.37 The average particle settling velocity plotted against time for all cases (all solid-volume fractions Φ). The black dashed-dotted line represents the vertical particle velocity of a single sphere U_T (case S178A).

Figure 3.38 shows the settling velocity of the suspension plotted against the solid-volume fraction. From this plot it can be determined that the settling velocity of the suspensions with $\Phi = 5.1 \cdot 10^{-3}$ and $\Phi = 1.0 \cdot 10^{-2}$ are increased by 7.8% and 2.7% compared to the value of a single particle. These increases are higher compared to the values seen in the steady vertical regime (previous section) for the same solid-volume fractions. Similar to the previous section, this figure could imply that the hindered settling effect observed by Richardson and Zaki comes into effect for solid-volume fractions $\Phi \gtrsim 0.01$.

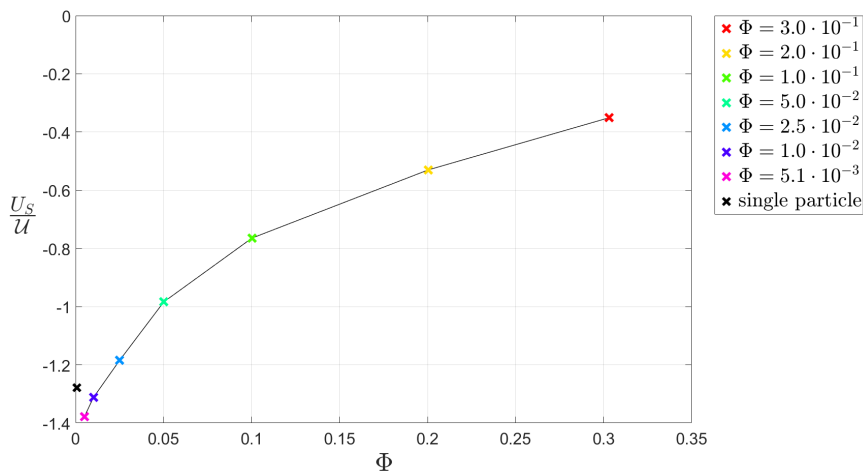


Figure 3.38 The settling velocity of the suspension plotted against the solid-volume fraction for all cases (all solid-volume fractions Φ). The black cross represents the terminal settling velocity of a single particle U_T (case S178A).

It can be seen in Figure 3.39 that n (see Equation 3.11) is not constant, since no straight line is observed in this plot. This indicates, similar to the steady vertical regime, that n does not solely depend on the particle Reynolds number Re_p and the ratio $\frac{D_p}{L_x}$ (or $\frac{D_p}{D_t}$), but also on the solid-volume fraction Φ itself.

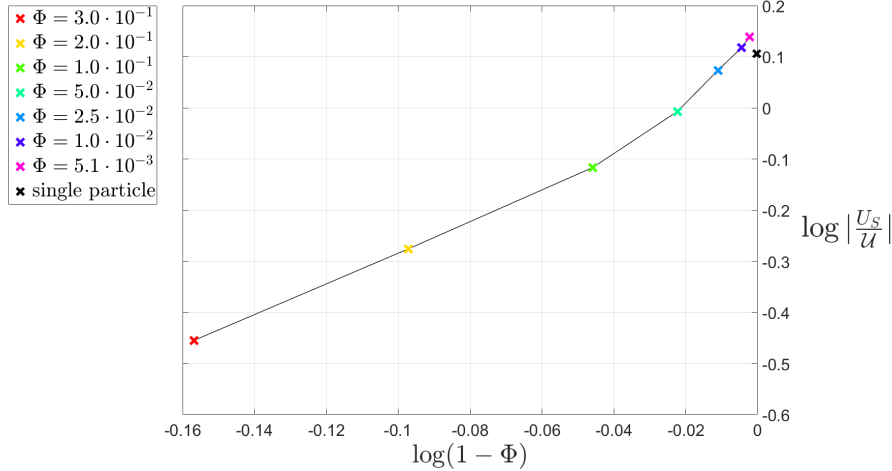


Figure 3.39 $\log |\frac{U_s}{U}|$ vs. $\log(1 - \Phi)$ for $Ga = 178$. The black cross indicates the terminal settling velocity of a single particle U_T .

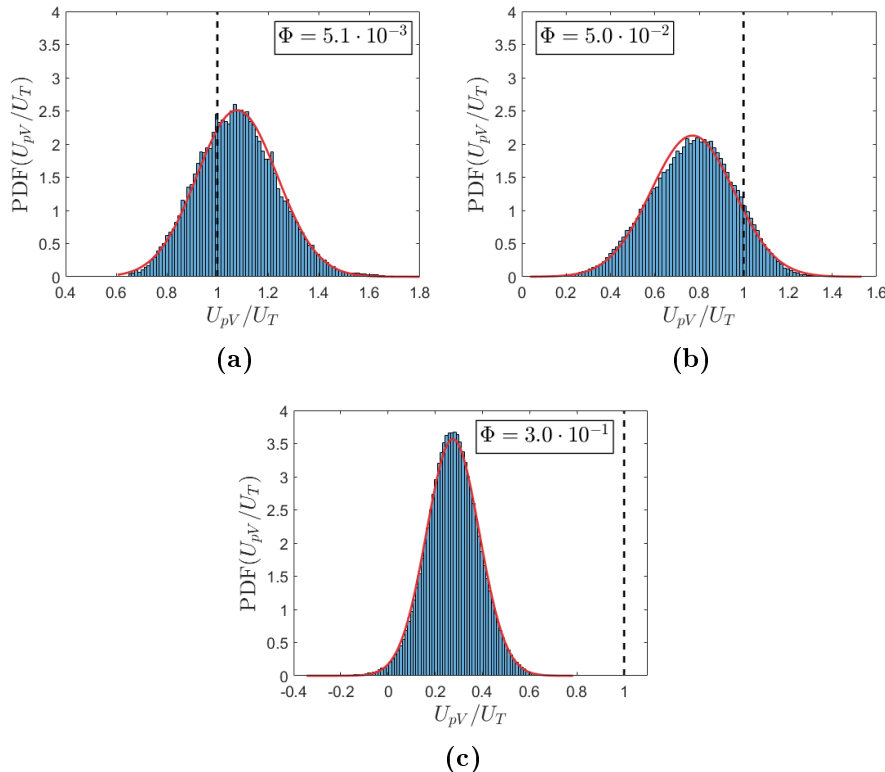


Figure 3.40 Distribution of the vertical particle velocity for $Ga = 178$ and (a) $\Phi = 5.1 \cdot 10^{-3}$, (b) $\Phi = 5.0 \cdot 10^{-2}$ and (c) $\Phi = 3.0 \cdot 10^{-1}$. The black dashed line indicates the settling velocity of a single sphere and the red line indicates the Gaussian distribution with a mean and standard deviation based on the vertical particle velocity simulation data.

In Figure 3.40 the distribution of the vertical particle velocity (normalized by the velocity of a single particle) is displayed for three different solid-volume fractions. The three solid-volume fractions are: $\Phi = 5.1 \cdot 10^{-3}$, $\Phi = 5.0 \cdot 10^{-2}$ and $\Phi = 3.0 \cdot 10^{-1}$. The velocity distributions of the other solid-volume fractions are appended in Appendix E.1. Note that the distribution of the vertical particle velocity is indicated by the normalized histogram, so that it displays the estimate of the probability density function (PDF) for the vertical particle velocity. The red line, added in the graphs, is a Gaussian distribution with a mean and standard deviation based on the vertical particle velocity simulation data of all particles.

As is the case in the steady vertical regime, the vertical particle velocity is approximately normally distributed for all solid-volume fractions in the steady oblique regime. So this statistic does not indicate the presence of particle clusters for the solid-volume fractions $\Phi = 5.1 \cdot 10^{-3}$ and $\Phi = 1.0 \cdot 10^{-2}$.

The distribution of the angle θ (Figure 3.41) shows a familiar sight: Similar to the steady vertical regime, a clear increase is visible for $\theta < 30^\circ$ (or $\theta > 150^\circ$) for the solid-volume fractions $\Phi = 5.1 \cdot 10^{-3}$, $\Phi = 1.0 \cdot 10^{-2}$, $\Phi = 2.5 \cdot 10^{-2}$ and therefore their statistics differ strongly from that of random distributed particles (PDF_{RDP}, as described in the previous section). This result indicates that particles do interact with each other and the particles are found to align vertically more than random distributed particles. This will result in the clustering of particles and causes the settling velocity of the particles to fall faster than the particles would individually. A remarkable difference in the distribution of θ for $\Phi = 5.1 \cdot 10^{-3}$ is observed when comparing $Ga = 144$ and $Ga = 178$: $Ga = 178$ shows a reduction of the distribution of θ for an angle $\theta \approx 90^\circ$, compared to the same solid-volume fraction in the steady vertical regime ($Ga = 144$). This means the probability of particles located next to each other is reduced for the steady oblique regime (compared to the steady vertical regime). This difference was also observed in the work of Huisman et al.[15] and it possibly explains why the increase of the settling velocity of the suspension is higher in the steady oblique regime (7.8%) compared to the steady vertical regime (4.1%) for $\Phi = 5.1 \cdot 10^{-3}$.

Additionally, Figure 3.42 and 3.43 strongly support the hypothesis of cluster formation. The pictures seen in Figure 3.43 and the two particles simulation (T178) support the suggestion by Uhlmann and Doychev [7] that DKT is the key mechanism of cluster formation.

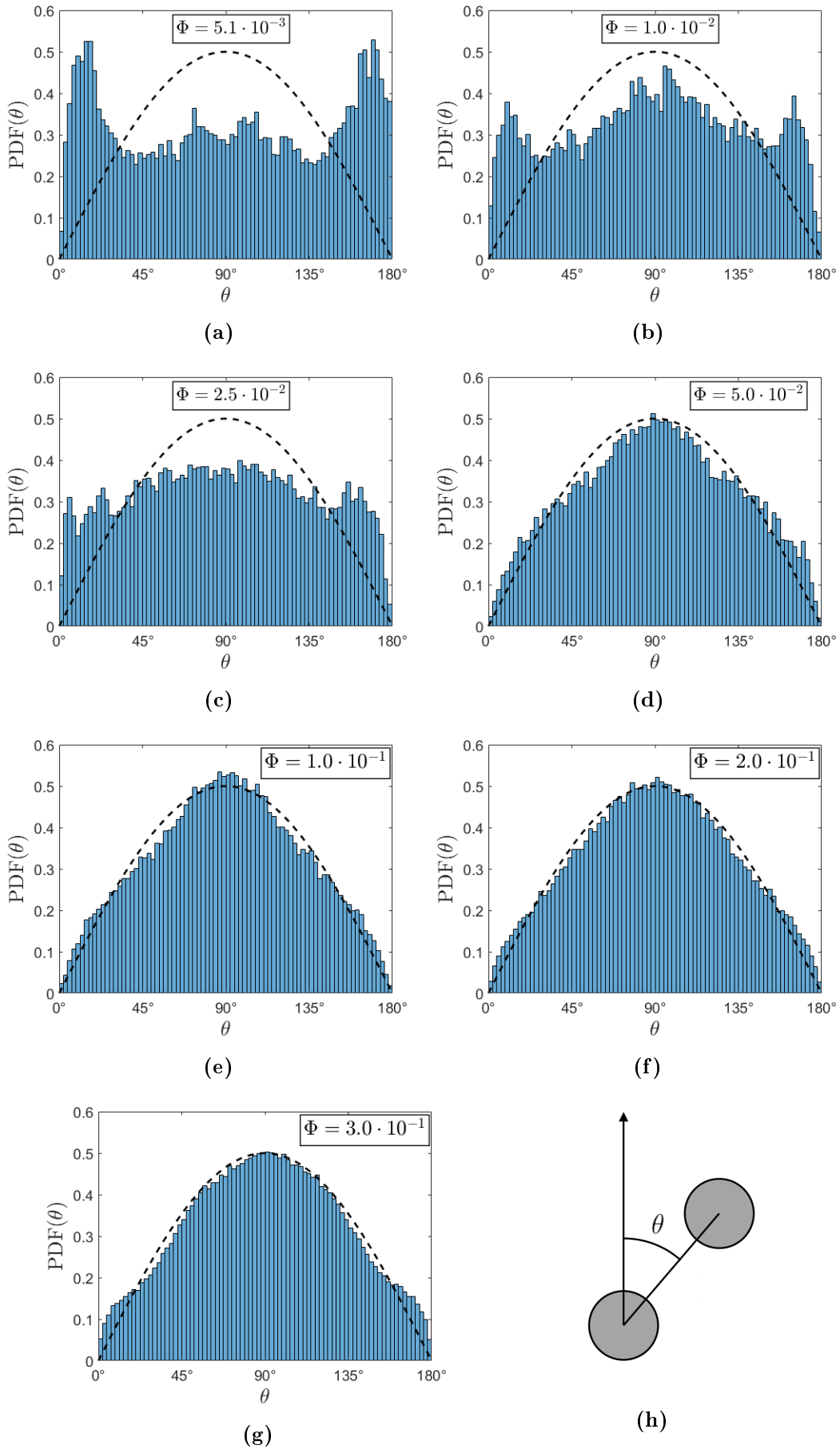


Figure 3.41 Distribution of the angle θ for $Ga = 178$ and all solid-volume fractions. The black dashed line indicates the PDF for random distributed particles $\text{PDF}_{RDP} = \frac{1}{2} \sin(\theta)$. Notice the increase for $\theta < 30^\circ$ (or $\theta > 150^\circ$) for the dilute suspensions (Φ). (h) The basic principle of the angle θ .

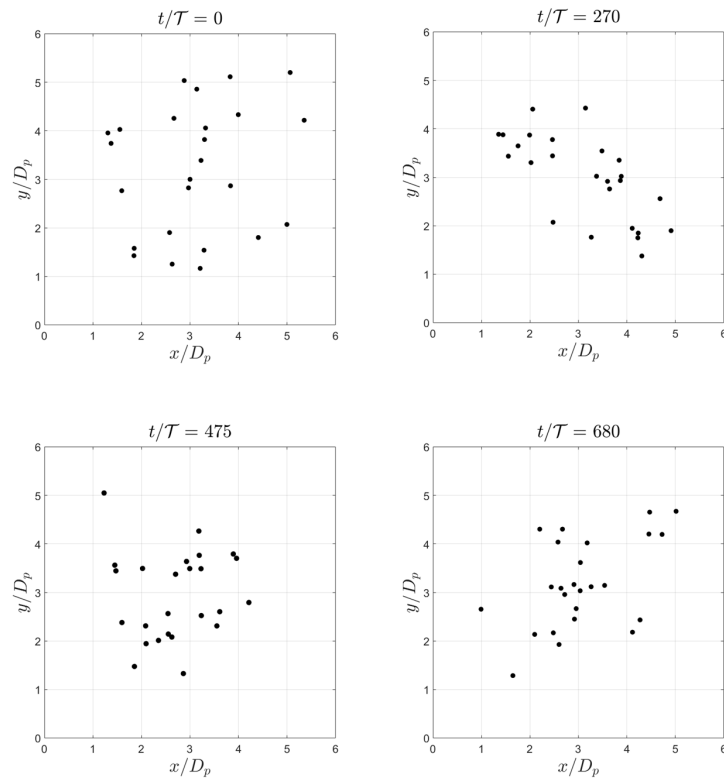


Figure 3.42 Particle locations seen from the top of the computational domain for several time instances for case M178A ($Ga = 178$ and $\Phi = 5.1 \cdot 10^{-3}$). It is observed that the particles align vertically more for different instances in time than the initial setup ($t = 0\mathcal{T}$).

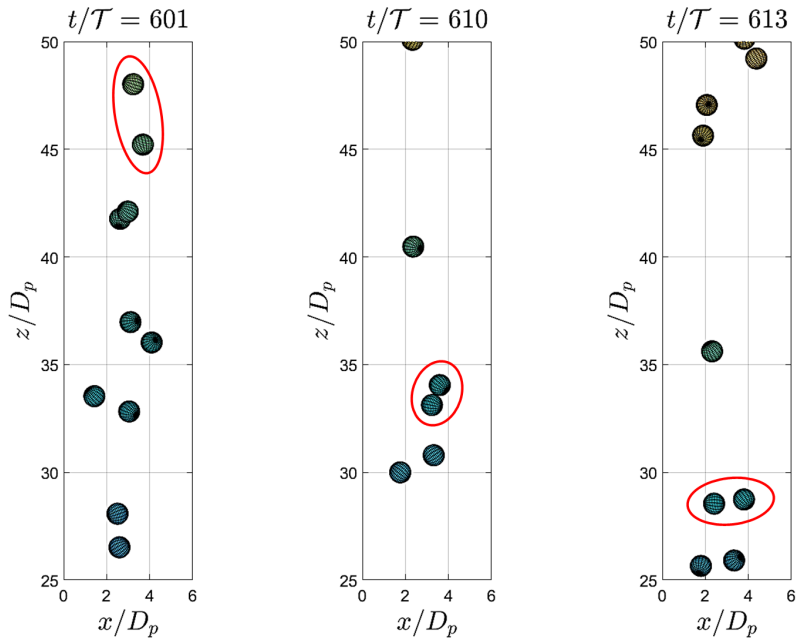


Figure 3.43 From left to right: Drafting, kissing, tumbling. One of many instances of DKT seen in the simulations for case M178A ($Ga = 178$ and $\Phi = 5.1 \cdot 10^{-3}$).

3.3.3 Oblique oscillating regime

In Figure 3.44 the average particle settling velocity $\overline{U_{pV}}$ has been plotted against time for all cases (M200A-M200G). Similar to the other regimes, the anticipated hindered settling effect is clearly observed and the fluctuations of the average particle settling velocity are larger for the dilute cases compared to the dense cases.

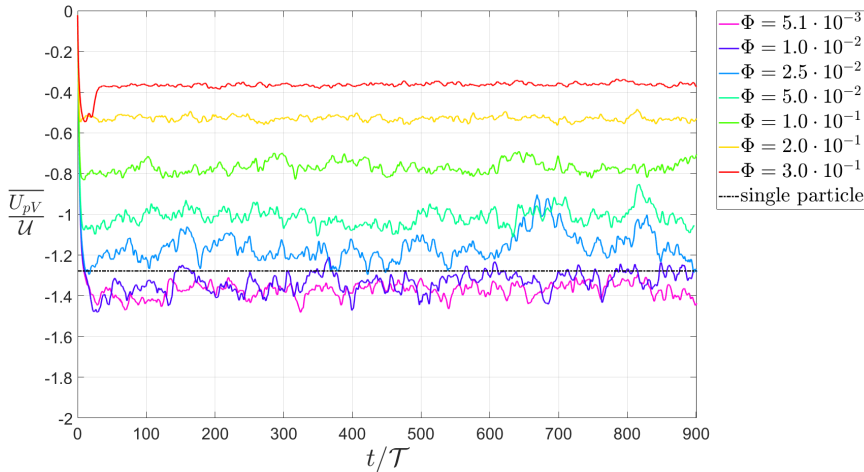


Figure 3.44 The average particle settling velocity plotted against time for all cases (all solid-volume fractions Φ). The black dashed-dotted line represents the vertical particle velocity of a single sphere U_T (case S200A).

The results involving the settling velocity of the suspensions for $Ga = 200$ are similar to the results for $Ga = 178$. Both dilute suspensions ($\Phi = 5.1 \cdot 10^{-3}$ and $\Phi = 1.0 \cdot 10^{-2}$) show a significant increase in the magnitude of the settling velocity of the suspension compared to the value of a single particle (S200A). The increases are 7.1% and 4.0%, respectively. These increases are of the same level as seen in the steady oblique regime. Similar to the steady oblique regime, it is also observed in the oblique oscillating regime that the hindered settling effect comes into effect for solid-volume fractions $\Phi \gtrsim 0.01$. Finally, it is seen in Figure 3.46 that the exponent n is not constant.

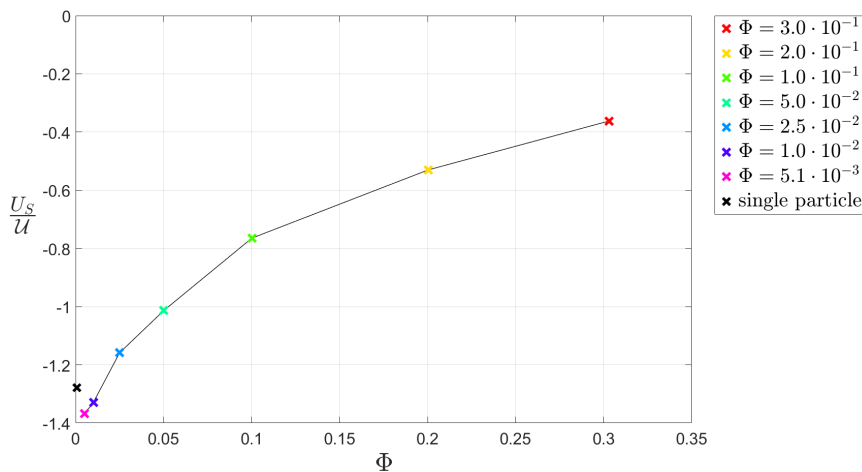


Figure 3.45 The settling velocity of the suspension plotted against the solid-volume fraction for all cases (all solid-volume fractions Φ). The black cross represents the terminal settling velocity of a single particle U_T (case S200A).

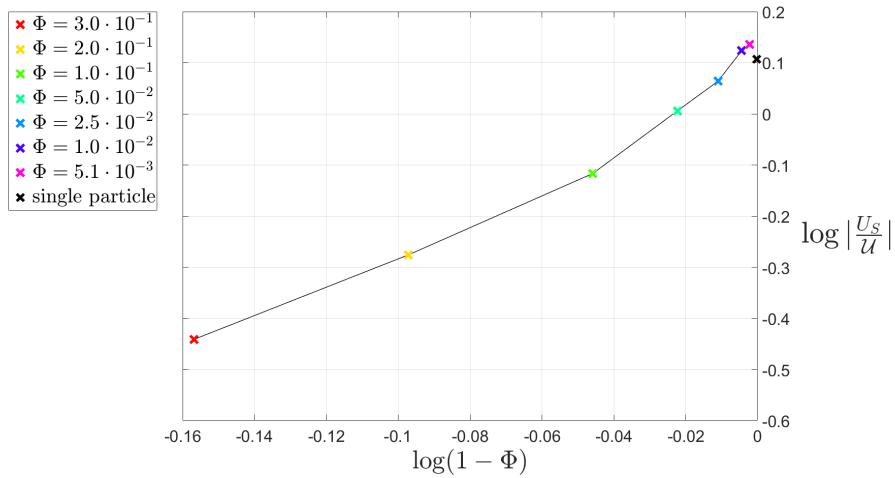


Figure 3.46 $\log \left| \frac{U_S}{U} \right|$ vs. $\log(1 - \Phi)$ for $Ga = 200$. The black cross indicates the terminal settling velocity of a single particle U_T .

The distributions of the vertical particle velocity and the angle θ can be seen in Figures 3.47 and 3.48, respectively. Similar statistics, regarding the distribution of the vertical particle velocity, are observed for the oblique oscillating regime and the other two regimes (steady vertical and steady oblique).

For $\Phi = 5.1 \cdot 10^{-3}$ and $Ga = 200$, the distribution for θ is similar to the distribution seen in the steady vertical regime, while the increase of U_S (7.1%) is higher compared to the steady vertical regime (4.1%). This contradicts the suggestion made in the previous section. Hence, the distribution of θ and the increase of the settling velocity of the suspension compared to the velocity of a single particle are not related.

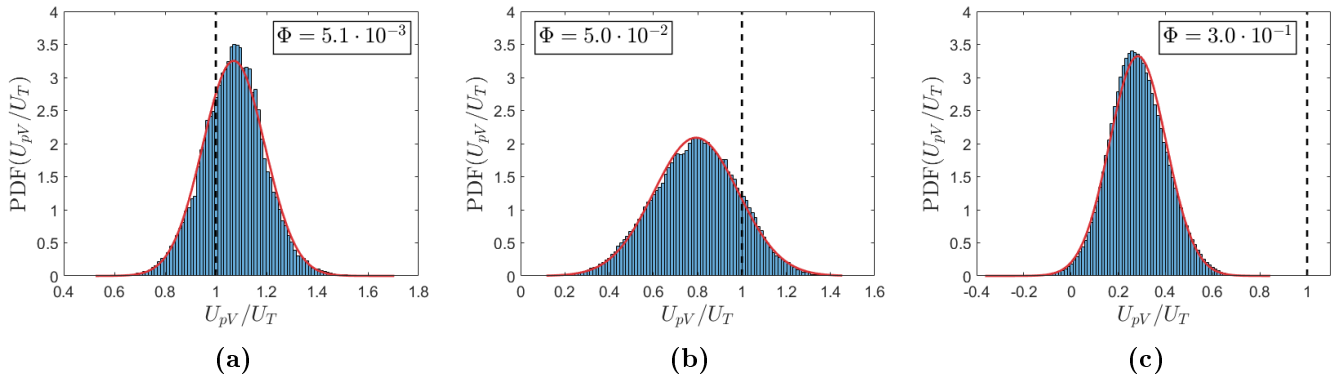


Figure 3.47 Distribution of the vertical particle velocity for $Ga = 200$ and (a) $\Phi = 5.1 \cdot 10^{-3}$, (b) $\Phi = 5.0 \cdot 10^{-2}$ and (c) $\Phi = 3.0 \cdot 10^{-1}$. The black dashed line indicates the settling velocity of a single sphere and the red line indicates the Gaussian distribution with a mean and standard deviation based on the vertical particle velocity simulation data.

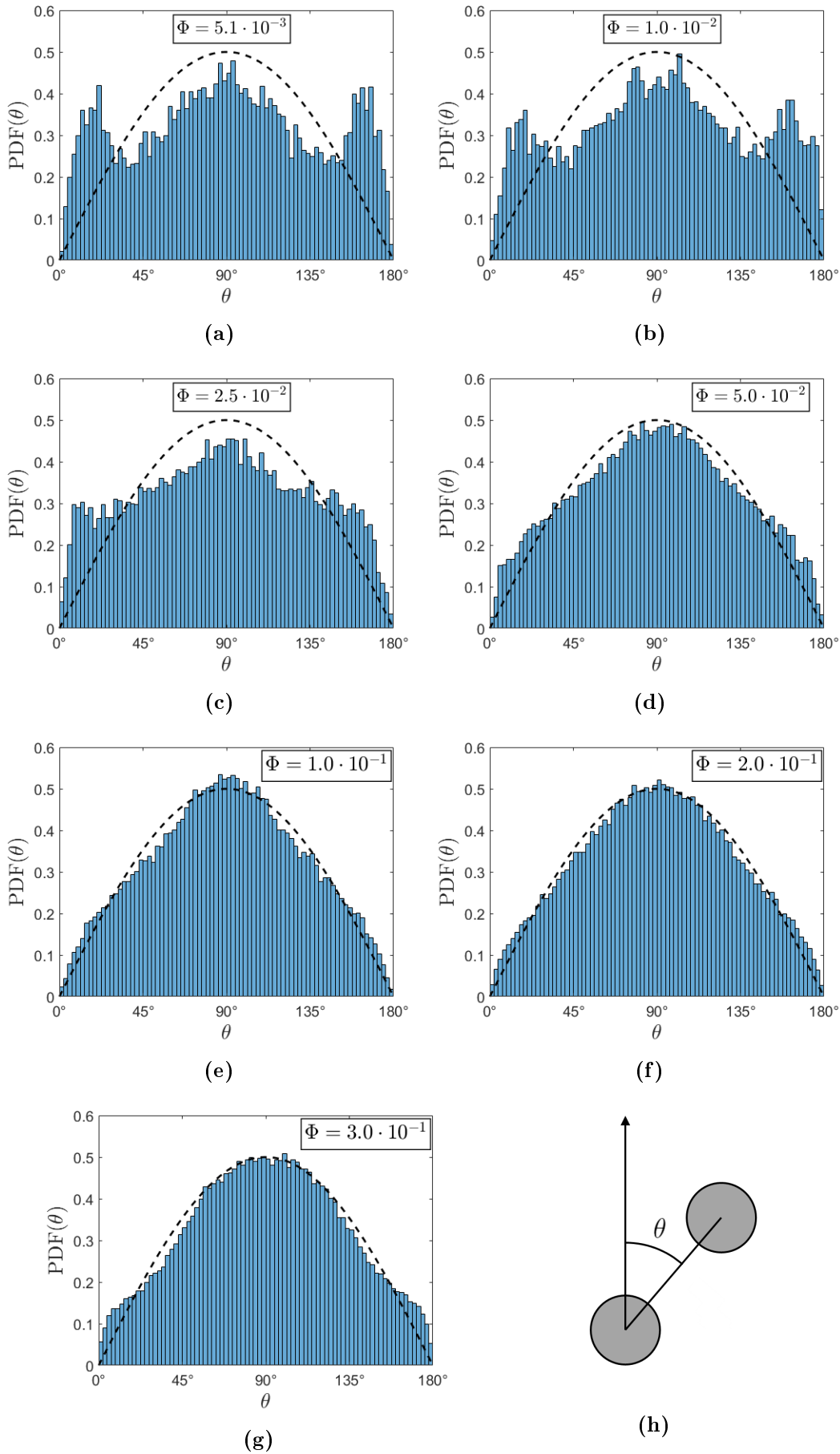


Figure 3.48 Distribution of the angle θ for $Ga = 200$ and all solid-volume fractions. The black dashed line indicates the PDF for random distributed particles $\text{PDF}_{RDP} = \frac{1}{2} \sin(\theta)$. Notice the increase for $\theta < 30^\circ$ (or $\theta > 150^\circ$) for the dilute suspensions (Φ). (h) The basic principle of the angle θ .

It can be seen (similar to the other regimes) that for increasing solid-volume fraction, the distribution of θ becomes similar to that of random distributed particles, which could mean that particle clustering vanishes and other interactions occur. The statistic of θ for the dilute suspensions indicates the formation of clusters. This is supported by Figure 3.49 and 3.50, which show the particle locations for different time instances and a visualization of DKT seen in the simulations for $\Phi = 1.0 \cdot 10^{-2}$.

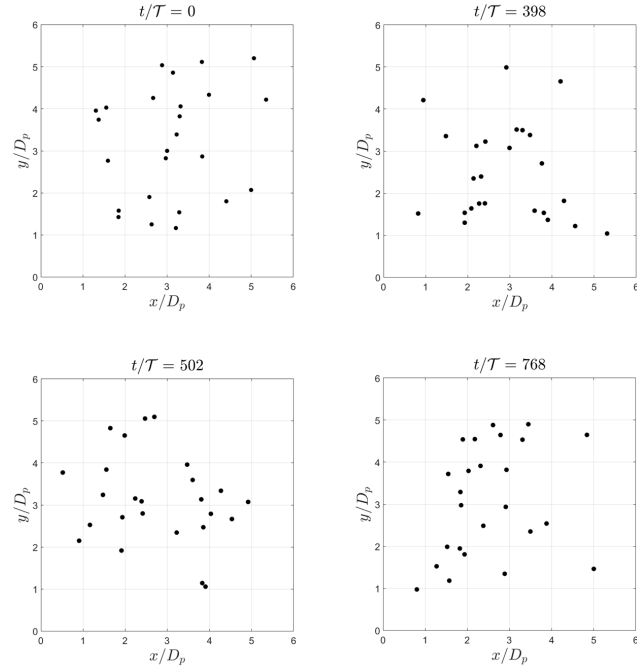


Figure 3.49 Particle locations seen from the top of the computational domain for several time instances for case M200B ($Ga = 200$ and $\Phi = 1.0 \cdot 10^{-2}$). It is observed that the particles align vertically more for different instances in time than the initial setup ($t = 0\mathcal{T}$).

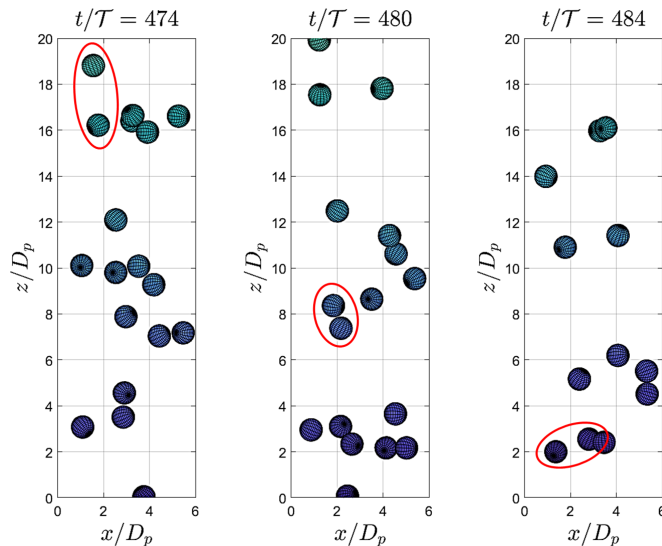


Figure 3.50 From left to right: Drafting, kissing, tumbling. One of many instances of DKT seen in the simulations for case M200B ($Ga = 200$ and $\Phi = 1.0 \cdot 10^{-2}$).

3.3.4 Vertical particle velocity fluctuations

The standard deviation (or root-mean-square) of the vertical particle velocity (U_{pV}^{rms}) is the simplest measure of the vertical particle velocity fluctuations. In the work of Guazzelli and Hinch [26] it is observed that in the Stokes regime, the vertical particle velocity fluctuations (normalized by U_S) reach a maximum at $\Phi \approx 0.3$, which means the velocity fluctuations are the strongest for this solid-volume fraction. It was shown for solid-volume fractions $\Phi < 0.3$ that the relation between the vertical particle velocity fluctuations and the solid-volume fraction is given by Equation 3.12 (for the Stokes regime).

$$\frac{U_{pV}^{rms}}{U_S} \approx A\Phi^{1/3}, \quad \text{with } 2 \leq A \leq 3 \quad (3.12)$$

In Figure 3.51 the vertical particle velocity fluctuations normalized by the settling velocity of the suspension are plotted against the solid-volume fraction for the simulations in the present work. It can be seen for all Galileo numbers that the strongest velocity fluctuations occur for $\Phi = 0.3$. Since this study focuses on particle Reynolds numbers in the intermediate regime, a different relation between the vertical particle velocity fluctuations and the solid-volume fraction is expected. A suggested relation is given by Equation 3.13 and is plotted in Figure 3.51. It can be seen in this figure that Equation 3.13 is a good approximation for the vertical particle velocity fluctuations given a solid-volume fraction $\Phi < 0.3$. This relation suggests that the vertical particle velocity fluctuations increase roughly as $\Phi^{1/3}$ for the intermediate particle Reynolds numbers considered in this work, which is similar to the Stokes regime.

$$\frac{U_{pV}^{rms}}{U_S} \approx B\Phi^{1/3}, \quad \text{with } 0.6 \leq B \leq 0.7 \quad (3.13)$$

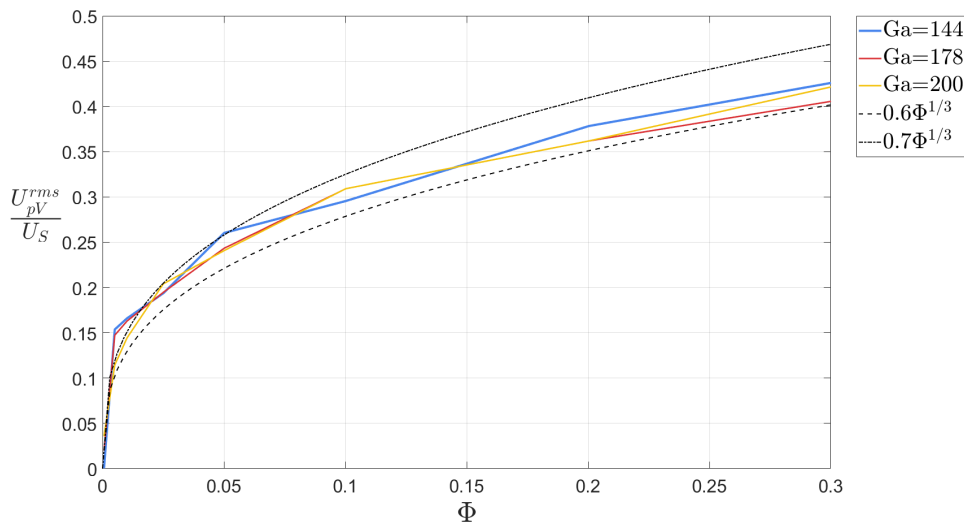


Figure 3.51 Vertical particle velocity fluctuations normalized by U_S versus the solid-volume fraction for the three Galileo numbers considered in the multiple particles simulations. The dashed and dash-dotted line represent Equation 3.13 with $B = 0.6$ and $B = 0.7$, respectively.

Chapter 4

Conclusions

Direct numerical simulations of the settling of a single, two and multiple solid spheres under gravity have been performed. The simulations involve 4 different Galileo numbers, i.e. $Ga = 144, 178, 200$ and 250 for a fixed solid-to-fluid-density ratio $\Gamma = 1.5$. In the study of Jenny et al.[3] it is shown that for these Ga the particle motions of a single particle are steady vertical, steady oblique, oblique oscillating and chaotic. The influence of these different regimes of motion on the dynamics of suspensions of solid spheres with solid-volume fractions ranging from $\Phi = 0.005$ to $\Phi = 0.3$ has been investigated in this work. This is done by observing the dynamics of a single particle, two particles and eventually multiple particles. To resemble the conditions of an experiment, such as the experiments of Richardson and Zaki [1] and Huisman et al.[15], it is chosen to implement a square duct.

From the simulations of a single settling sphere it is shown that the fluctuations of the vertical particle velocity for $Ga = 178, 200, 250$ are dominated by particle-wall interactions. For these Galileo numbers, the vertical particle velocity decreases when it approaches a wall and increases to a maximum value when it moves away from the wall. In the steady oblique regime the particle never collides with the wall, which is probably due to a wake-induced lift force acting on the particle directed away from the wall. The motion of the particle for $Ga = 144$ was found to be not perfectly steady vertical, since it has been shown that it also moves in the horizontal plane. It is observed that the movement in the horizontal plane is suppressed, when the square duct employed in the simulations becomes narrower, i.e. increasing $\frac{D_p}{L_x}$. It is suggested that this is due to a lift force related to the potential flow theory.

Drafting-kissing-tumbling has been investigated in the simulations of two settling spheres. Instances of DKT in these simulations show an increase of the vertical particle velocity of both the trailing and leading particle during the drafting stage. It is also found that DKT initiates when the particles are almost vertically aligned and move in the same direction in the horizontal plane. DKT could even occur when the particles are several particle diameters apart.

The results of the settling of suspensions for $Ga = 144, 178, 200$ show that the hindered settling effect (see definition in Section 1.2.3) comes into effect for solid-volume fractions $\Phi \gtrapprox 0.01$. The results also show that the exponent n is not constant for this range of solid-volume fractions, which indicates that n is not solely dependent on the Re_p and the ratio $\frac{D_p}{D_t}$, but also on the solid-volume fraction Φ itself.

For the solid-volume fractions $\Phi \leq 0.01$ an increase in the settling velocity of the suspensions U_S compared to the value of a single particle is observed for all regimes (vertical, oblique, oblique oscillating). The increases are higher in the steady oblique and oblique oscillating regime compared to the steady vertical regime.

For all the regimes it has been shown that the vertical particle velocity is roughly normally distributed for all solid-volume fractions. For the dilute suspensions ($\Phi \leq 0.01$), the distribution of the angle θ (the angle of a particle with its nearest neighbouring particle and the vertical) shows that particles are found to align vertically more than random distributed particles. This statistic indicates that particles do interact with each other and causes the trailing particles to enter the wake of leading particles, which results in the formation of particle clusters and thus an increase in the settling velocity of the suspension. These findings are supported by instances of DKT observed in the animations of the simulations and by looking at the particle locations from the top of the computational domain at several time instances.

Huisman et al.[15] also observed particle clustering in the steady vertical regime (at an even lower solid-volume fraction), while in the studies of Uhlmann and Doychev [7] no significant increase in the settling velocity of the suspension was observed nor the formation of clusters in a triply periodic computational box for the same regime. The clustering of particles in the steady vertical regime, resulting in an increase of the settling velocity of the suspension, might be explained by large-scale flows, such as intrinsic convection, caused by the settling of multiple particles in a confined geometry.

Furthermore, the distribution of the angle θ is found to resemble the PDF of the θ for random distributed particles as the solid-volume fraction increases, which would indicate that with increasing Φ , particle clustering vanishes and other interactions influence the sedimentation of the particles.

Finally, it has been observed for all regimes (corresponding to intermediate Reynolds numbers) that the vertical particle velocity fluctuations relative to the settling velocity of the suspension increase roughly with $\Phi^{1/3}$, which is similar to the Stokes regime. These relative fluctuations are the highest for $\Phi = 0.3$ in the present simulations.

As a future perspective, it would be interesting to investigate the sedimentation of multiple (spherical) particles for different cross-section dimensions of the duct, to see whether the clustering of particles vanishes for the steady vertical regime when the cross-section dimensions are chosen large enough. It is also interesting to investigate the relative vertical particle velocity fluctuations for higher solid-volume fractions $\Phi > 0.3$, to see for which Φ it shows a maximum value for intermediate Reynolds numbers (in the Stokes regime it is found that the maximum relative velocity fluctuations occur for $\Phi = 0.3$). Finally, a subject of interest is to determine whether clustering of particles in dilute suspensions is dominated by macroscale effects (such as intrinsic convection) or microscale effects (such as the DKT mechanism) or a combination of both.

Appendix A

Governing equations

A.1 Equations for flows with solid particles

In this study an incompressible Newtonian flow is assumed and describes the motion of spherical solid particles with diameter D_p in a quiescent Newtonian fluid.

Fluid phase

The fluid phase is described by the equation for conservation of mass [A.1](#) and the Navier-Stokes equation for an incompressible Newtonian flow [A.2](#):

$$\nabla \cdot \mathbf{u} = 0 \quad (\text{A.1})$$

$$\underbrace{\rho_f \left(\frac{\partial \mathbf{u}}{\partial t} + \nabla \cdot \mathbf{u} \mathbf{u} \right)}_1 = \underbrace{-\nabla p}_2 + \underbrace{\mu_f \nabla^2 \mathbf{u}}_3 \quad (\text{A.2})$$

where \mathbf{u} is the flow velocity, p is the modified pressure (the total pressure minus the contribution from the hydrostatic pressure), ρ_f is the mass density and μ_f is the dynamic viscosity of the fluid.

The terms correspond to inertial forces (1), pressure forces (2) and viscous forces (3).

Solid phase

The velocity of a particle segment at position \mathbf{X} located on the surface ∂V of the particle:

$$\mathbf{U}_{ps}(\mathbf{X}) = \mathbf{u}_c + \boldsymbol{\omega}_c \times \mathbf{r} \quad (\text{A.3})$$

where $\mathbf{r} = \mathbf{X} - \mathbf{x}_c$ is the position vector relative to the center of the particle. \mathbf{u}_c is the translational velocity of the particle centroid, whereas $\boldsymbol{\omega}_c$ is the angular velocity of the particle. The translational and rotational velocities are described by Equation [A.4](#) and [A.5](#), respectively. These equations are known as the Newton-Euler equations for solid spheres.

$$\rho_p V_p \frac{d\mathbf{u}_c}{dt} = \oint_{\partial V} \boldsymbol{\tau} \cdot \mathbf{n} dA + (\rho_p - \rho_f) V_p \mathbf{g} \quad (\text{A.4})$$

$$I_p \frac{d\boldsymbol{\omega}_c}{dt} = \oint_{\partial V} \mathbf{r} \times (\boldsymbol{\tau} \cdot \mathbf{n}) dA \quad (\text{A.5})$$

ρ_p is the mass density and V_p is the volume of the particle.

I_p is the moment of inertia of the particle. In this study the main focus is on spherical particles with diameter D_p , hence the volume is $V_p = \frac{\pi}{6}D_p^3$ and the moment of inertia is $I_p = \frac{\pi}{60}\rho_p D_p^5$.

$\boldsymbol{\tau} = -p\mathbf{I} + \mu_f(\nabla\mathbf{u} + \nabla\mathbf{u}^T)$ is the stress tensor for a Newtonian fluid with unit tensor \mathbf{I} , \mathbf{n} is the outward pointing unit normal at the surface ∂V of the particle and the gravitational vector $\mathbf{g} = -g\mathbf{k}$, where \mathbf{k} is the unit vector in the positive z -direction

Coupling solid and fluid phase

Equations A.1, A.2, A.4 and A.5 form a system of differential equations. These equations are coupled through a no-slip and no-penetration condition at the surface of the particle A.6. The fluid and particle motion are obtained by solving the system of differential equations with the interface condition.

$$\mathbf{u} = \mathbf{U}_{ps} \quad \forall \mathbf{X} \in \partial V \quad (\text{A.6})$$

A.2 Non-dimensionalized equations and free parameters

Non-dimensionalization of the Navier-Stokes and Newton-Euler equations results in dimensionless parameters characteristic for particle-laden flows. For the non-dimensionalization a characteristic length scale \mathcal{L} and velocity scale \mathcal{U} are used to obtain the following dimensionless variables.

Navier-Stokes:

$$\begin{aligned}\nabla^* &= \mathcal{L}\nabla, & \mathbf{u}^* &= \mathbf{u}/\mathcal{U}, & t^* &= t/(\mathcal{L}/\mathcal{U}), \\ p^* &= p/(\rho_f\mathcal{U}^2).\end{aligned}$$

Newton-Euler:

$$\begin{aligned}\mathbf{U}_p^* &= \mathbf{U}_p/\mathcal{U}, & \mathbf{u}_c^* &= \mathbf{u}_c/\mathcal{U}, & \boldsymbol{\omega}_c^* &= \boldsymbol{\omega}_c \cdot (\mathcal{L}/\mathcal{U}) \\ \mathbf{r}^* &= \mathbf{r}/\mathcal{L}, & \mathbf{X}^* &= \mathbf{X}/\mathcal{L}, & \mathbf{x}_c^* &= \mathbf{x}_c/\mathcal{L} \\ A^* &= A/\mathcal{L}^2, & \boldsymbol{\tau}^* &= \boldsymbol{\tau}/(\rho_f\mathcal{U}^2).\end{aligned}$$

Substituting these dimensionless variables into Equation A.1-A.6 results in the following non-dimensionalized equations for the fluid and solid phase:

$$\nabla^* \cdot \mathbf{u}^* = 0 \quad (\text{A.7})$$

$$\frac{\partial \mathbf{u}^*}{\partial t^*} + \mathbf{u}^* \cdot \nabla \mathbf{u}^* = -\nabla^* p^* + \boxed{\frac{\nu_f}{\mathcal{U}\mathcal{L}}} \nabla^{*2} \mathbf{u}^* \quad (\text{A.8})$$

$$\mathbf{U}_p^*(\mathbf{X}^*) = \mathbf{u}_c^* + \boldsymbol{\omega}_c^* \times \mathbf{r}^* \quad (\text{A.9})$$

$$\boxed{\Gamma} \left(\boxed{\frac{D_p}{\mathcal{L}}} \right)^3 \frac{d\mathbf{u}_c^*}{dt^*} = \frac{6}{\pi} \oint_{\partial V} \boldsymbol{\tau}^* \cdot \mathbf{n} dA^* - \boxed{\frac{(\Gamma-1)g\mathcal{L}}{\mathcal{U}^2}} \mathbf{k} \quad (\text{A.10})$$

$$\boxed{\Gamma} \left(\boxed{\frac{D_p}{\mathcal{L}}} \right)^5 \frac{d\boldsymbol{\omega}_c}{dt} = \frac{60}{\pi} \oint_{\partial V} \mathbf{r}^* \times (\boldsymbol{\tau}^* \cdot \mathbf{n}) dA^* \quad (\text{A.11})$$

$$\mathbf{u}^* = \mathbf{U}_p^* \quad \forall \mathbf{X}^* \in \partial V \quad (\text{A.12})$$

The four dimensionless parameters boxed in Equation A.7-A.12 are:

- Reynolds number $Re \equiv \frac{U\mathcal{L}}{\nu_f}$
- Particle densimetric Froude number $Fr \equiv \frac{U}{\sqrt{|\Gamma-1|g\mathcal{L}}}$
- Solid-to-fluid-density ratio Γ
- Particle diameter-to-characteristic length scale ratio $\frac{D_p}{\mathcal{L}}$

Dynamic similarity requires these four dimensionless numbers to be kept constant. Fortunately, the number of free parameters is reduced to **two** by a proper choice of the characteristic length and velocity scales (\mathcal{L}, U):

$$\begin{aligned} \mathcal{L} &= D_p & \frac{D_p}{\mathcal{L}} &= 1 & \boxed{\Gamma} \\ U &= \sqrt{|\Gamma-1|gD_p} & Fr &= 1 & \boxed{Re = \sqrt{\frac{|\Gamma-1|gD_p^3}{\nu_f^2}} = Ga} \end{aligned}$$

So it can be concluded from the dimensional analysis of the Navier-Stokes and Newton-Euler equations, that the parameters characterizing particle laden flows are the **solid-to-fluid-density ratio** $\Gamma = \frac{\rho_p}{\rho_f}$ and the **Galileo number** Ga .

Appendix B

Sphere dynamics

B.1 Morison's equation for a sphere settling under gravity in free space

The Galileo number Ga and the solid-to-fluid-density ratio Γ are related to the particle Reynolds number Re_p . Their relation can be approximated with Morison's equation¹ for unsteady particle motion (Morison et al.[27]). In case of a spherical particle in gravitational motion in free space, Morison's equation reads:

$$\underbrace{\rho_p V_p \frac{dU_{pz}}{dt}}_1 = \underbrace{(\rho_p - \rho_f)V_p g}_2 - \underbrace{\frac{1}{2}\rho_f V_p \frac{dU_{pz}}{dt}}_3 - C_D A_{fs} \frac{1}{2} \rho_f U_{pz}^2 \quad (\text{B.1})$$

Where A_{fs} is the frontal surface area of the particle, which is $A_{fs} = \frac{\pi}{4} D_p^2$ for a sphere. The terms correspond to particle inertia (1), buoyancy force (2), added mass (3) and drag force (4).

Equation B.1 can be rewritten to obtain the non-dimensional form of Morison's equation for unsteady motion of a sphere settling under gravity:

$$[(\Gamma + \frac{1}{2}) \cdot Ga] \frac{dRe_p}{d(t/\mathcal{T})} = Ga^2 - \frac{3}{4} C_D(Re_p) \cdot Re_p^2 \quad (\text{B.2})$$

With $Re_p = \frac{U_{pz} D_p}{\nu_f}$ and where $\mathcal{T} = \mathcal{L}/\mathcal{U}$ is a characteristic time scale. \mathcal{L} and \mathcal{U} are listed in A.2.

Different empirical relations between the drag coefficient and the particle Reynolds number were obtained throughout the twentieth century [28]. For this study the relation from Abraham [29] is used, which reads:

$$C_D(Re_p) = \left(\sqrt{\frac{24}{Re_p}} + 0.5407 \right)^2 \quad (\text{B.3})$$

When a sphere is falling at its terminal velocity, the right hand side of Equation B.2 becomes zero. Then Equation B.2 reduces to:

$$0 = Ga^2 - \frac{3}{4} C_D(Re_T) \cdot Re_T^2 \quad (\text{B.4})$$

Where Re_T is the Reynolds number at the sphere's terminal settling velocity U_T . Equation B.4 is the non-dimensional form of Morison's equation for steady motion of a sphere settling under gravity in free space. This equation relates Ga and Re_T

¹in literature also referred to as MOJS equation to recognize the contributions of the originators: Morison, O'Brien, Johnson and Schaaf

and since Ga is given, the equation can be solved for Re_T using the Newton–Raphson method. Table B.1 shows the solutions of Equation B.4 for $Ga = 144, 178, 200, 250$.

TABLE B.1: Solutions to Equation B.4 for the Ga numbers of interest in this work.

Ga	Re_T	U_T/\mathcal{U}
144	184.46	1.2810
178	239.82	1.3473
200	276.46	1.3823
250	361.60	1.4464

B.2 Wall effects on terminal settling velocity of a sphere in a quiescent fluid

The effect of walls on the settling of a sphere in an otherwise quiescent fluid, i.e. a sphere falling under gravity in a cylindrical duct, has been extensively investigated [30, 31]. From these studies, it follows that for cylindrical ducts the absolute terminal settling velocity could be approximated quite well by the equation:

$$U_{T,duct} = \left(\frac{D_d^2 - D_p^2}{D_d^2} \right) U_{T,free} \quad (\text{B.5})$$

Where D_d is the diameter of the duct and D_p is the sphere diameter. $U_{T,duct}$ is the absolute terminal settling velocity of a the sphere and $U_{T,free}$ is the terminal settling velocity of a sphere falling in a quiescent fluid in an infinite medium (no walls).

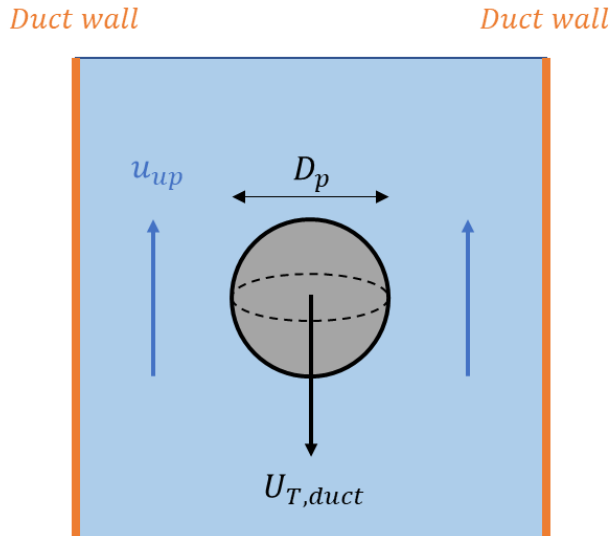


Figure B.1 The schematic of a sphere with diameter D_p falling in a duct.

In this study a similar equation for rectangular ducts is desired. Since a good approximation of $U_{T,duct}$ is required in order to track the sphere in the computational domain for as long as possible. From mass conservation it follows that there is an upward fluid flow, when the sphere is moving downwards (see Figure B.1). For a rectangular duct ($L_x \times L_y$) it follows that the averaged upward fluid velocity at the sphere midplane is:

$$u_{up} = - \left(\frac{\frac{\pi}{4} D_p^2}{L_x L_y - \frac{\pi}{4} D_p^2} \right) U_{T,duct} \quad (\text{B.6})$$

Thus the relative terminal velocity of the sphere relative the the surrounding fluid at the sphere midplane reads:

$$U_{T,rel} = U_{T,duct} - u_{up} = \left(1 + \frac{1}{\frac{4L_x L_y}{\pi D_p^2} - 1} \right) U_{T,duct} \quad (\text{B.7})$$

As a crude estimation, $U_{T,rel}$ is replaced with $U_{T,free}$ in order to give an approximation of $U_{T,duct}$. After applying the substitution and rearranging the terms in Equation B.7 the following equation for $U_{T,duct}$ is obtained:

$$U_{T,duct} = \left(1 - \frac{\frac{\pi}{4} D_p^2}{L_x L_y}\right) U_{T,free} \quad (\text{B.8})$$

Where $U_{T,free}$ is estimated from Morison's equation for a sphere settling under gravity (Appendix B.1):

$$\frac{U_{T,free}}{\mathcal{U}} = \frac{Re_T}{Ga} \quad (\text{B.9})$$

The value for $U_{T,duct}$ acts as a starting point for approximating w_∞ , which is the fluid velocity imposed at the inflow plane in the simulations.

B.3 Transient motion of a sphere

The transient motion of a sphere falling under gravity has been extensively studied. This section features an equation for the transient motion, which was acquired through experimental work by Mordant and Pinton [32]. Their experimental work focuses on Reynolds numbers between 40 and 7000. Since this study focuses on Reynolds numbers within this range and because of the elegance of their equation, it is used in this work to predict the transient motion in the vertical direction of a single sphere when an inflow is imposed. Two additional simulations were performed to validate the equation by Mordant and Pinton.

Non-dimensionalized by the terminal settling velocity obtained from the simulation U_{Tsim} and a characteristic time scale τ_0 obtained by Mordant and Pinton, the equation reads:

$$\frac{U_{pV}}{U_{Tsim}} = 1 - \exp\left(-\frac{t}{\tau_0}\right), \quad \text{with} \quad \frac{\tau_0}{\mathcal{T}} = \sqrt{\frac{4}{3C_{D,Tsim}}} \left(\Gamma + \frac{1}{2}\right) \quad (\text{B.10})$$

$C_{D,Tsim}$ is the drag coefficient based on Equation B.3, where Re_p is based on the terminal velocity (U_{Tsim}) obtained from the simulations, U_{pV} is the vertical component of particle velocity and $\mathcal{T} = \mathcal{L}/\mathcal{U}$.

To obtain the simulated data, a closed computational box with walls was used in which a sphere was released in a fluid at rest. The domain has to be large enough in the z -direction, allowing the particle to reach its terminal velocity before reaching the bottom of the domain. Hence, the domain dimensions are $L_x = L_y = 6D_p$ and $L_z = 54D_p$. The particle's initial position coordinates are $x_c = y_c = 3D_p$ and $z_c = 50D_p$. Figure B.2 shows the simulation results of the vertical velocity of the particle together with the graphical representation of Equation B.10 for $Ga = 144$ and $Ga = 178$. From this figure it can be concluded that Equation B.10 gives a good approximation of the transient motion of the particle in the vertical direction. Therefore this equation is used to determine the vertical trajectory of the particle when a moving frame of reference is used.

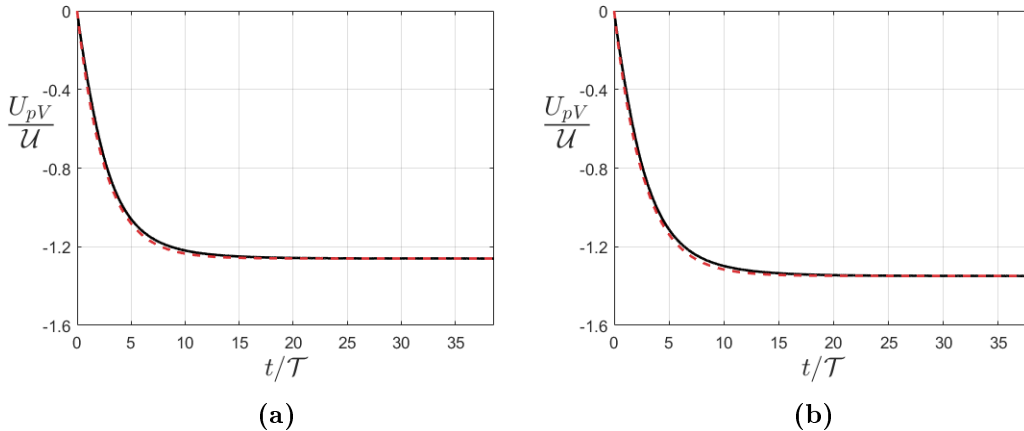


Figure B.2 Non-dimensionalized vertical velocity of a sphere for (a) $Ga = 144$ and (b) $Ga = 178$ obtained from the simulations. The black solid line indicates the simulation data and the red dashed line represents Equation B.10.

The equation to determine the vertical position of the sphere centroid when a moving frame of reference (mf) moving with w_∞ downwards is used, reads:

$$z_c^{mf}(t) = z_c(0) + \int_0^t U_{pV}^{mf} dt \quad \text{with} \quad U_{pV}^{mf} = U_{pV}^{abs} - (-w_\infty) \quad (\text{B.11})$$

Where U_{pV}^{abs} is the vertical particle velocity in the absolute frame of reference and is given by Equation B.10. When the integral in Equation B.11 is solved and the whole equation is non-dimensionalized one obtains:

$$\frac{z_c^{mf}(t)}{D_p} = \frac{z_c(0)}{D_p} + \frac{(U_{Tsim} + w_\infty)t}{D_p} + \frac{U_{Tsim}\tau_0}{D_p} [\exp(-\frac{t}{\tau_0}) - 1] \quad (\text{B.12})$$

Note that the value for U_{Tsim} is always negative, since the sphere falls in the negative z -direction. The value of U_{Tsim} is obtained from the for-mentioned simulation and reads $U_{Tsim} = -1.2600$ and $U_{Tsim} = -1.3487$ for $Ga = 144$ and $Ga = 178$, respectively.

The value for w_∞ is defined positive. When the values for w_∞ , stated in Table 2.3 (T144 and T178), are substituted in Equation B.12, a prediction of the vertical position of the center of the sphere as a function of time could be given. In Figure B.3 the predicted vertical position of the sphere centroid is given for $Ga = 144$ and $Ga = 178$.

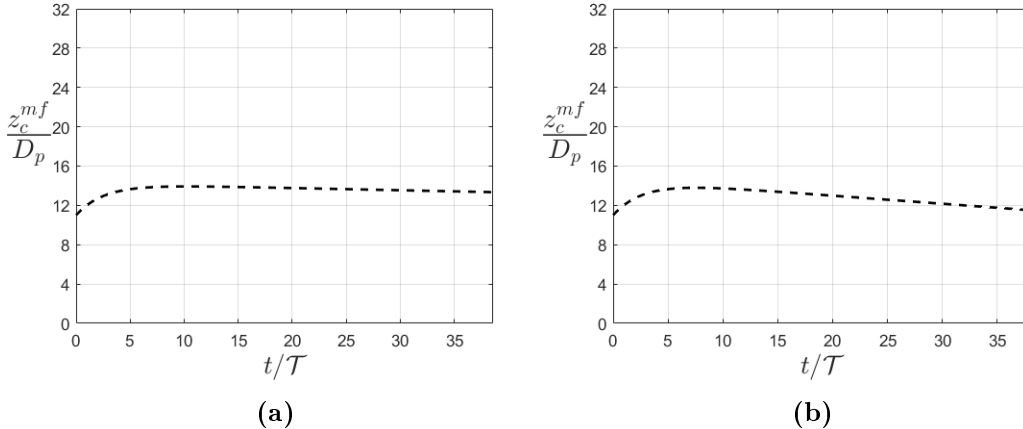


Figure B.3 Predicted vertical position for a single sphere in a moving frame of reference (moving with w_∞ downwards) as a function of time.

(a) $Ga = 144$ and $w_\infty = 1.2375$. (b) $Ga = 178$ and $w_\infty = 1.2665$. In both cases the initial position of the sphere $z_c(0) = 11D_p$.

Ideally, one should match the terminal settling velocity U_{Tsim} and the velocity of the moving frame w_∞ ($U_{Tsim} + w_\infty = 0$), so that the particle remains in the computational domain for an infinite amount of time. It can be seen in Figure B.3 that this is not the case, since the prediction shows that the particle will fall downwards in the moving frame (the particle falls faster than the moving frame is moving). This is done intentionally, since the prediction does not take into account the interaction between the particle and the walls and the interaction with the other particle in simulation T144 and T178. These interactions result in a decrease in the vertical particle velocity, which makes the particle move upwards in the moving frame of reference. Therefore it is chosen to set the magnitude of w_∞ lower than the magnitude

of U_{Tsim} , since it is undesirable for the particle to get close to either the bottom or top of the computational domain.

Appendix C

Immersed boundary method and collision model

Immersed boundary method

The Immersed Boundary Method (IBM) was originally developed by Charles Peskin [33]. The IBM is particularly fitted for multiphase flows involving a solid and a fluid phase. The method makes use of two different grids for the solid and fluid phase. For the fluid phase a fixed, simple-structured (Cartesian) grid is used , referred to as the *Eulerian* grid. The solid phase is represented by an uniform grid moving with the particle surface. This grid is referred to as the *Lagrangian* grid and it is immersed in the Eulerian grid. Both grids are illustrated in Figure C.1.

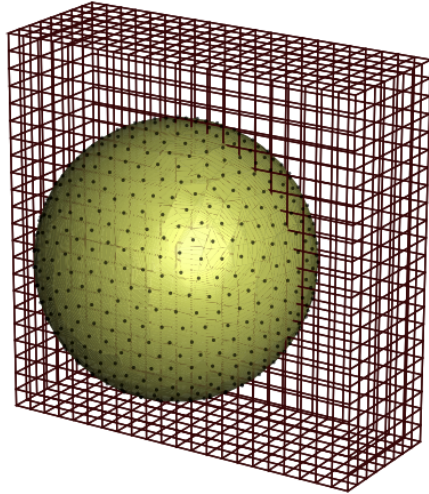


Figure C.1 A visualization of the Eulerian and Lagrangian grid used in the work of Breugem [21].

The no-slip/no-penetration condition (Equation A.6) on the surface of the particle is not employed directly. Instead, a force is applied to the flow in the vicinity of the particle surface, such that it satisfies the condition by a good approximation. This means that a force term has to be added to the RHS of the Navier-Stokes equation (Equation A.2), resulting in the following equation:

$$\rho_f \left(\frac{\partial \mathbf{u}}{\partial t} + \nabla \cdot \mathbf{u} \mathbf{u} \right) = -\nabla p + \mu_f \nabla^2 \mathbf{u} + \rho_f \mathbf{f} \quad (\text{C.1})$$

Equations C.1,A.1,A.4,A.5 are solved for the entire domain.

The use of a simple-structured grid, which does not require regridding when the particles move, makes the IBM computationally more efficient than methods with a body-fitted grid. Unfortunately, the IBM is less accurate than a method with a body-fitted grid, since there is an error in the approximation of the no-slip/no-penetration condition.

Since the original IBM of Peskin, multiple IBM versions were developed to increase the accuracy while maintaining the computational efficiency. One of these versions is the IBM of Breugem [21], which is employed in this work. Breugem improved Uhlmann's IBM [16] by: (1) applying a *multidirect forcing scheme* proposed by Luo et al.[34] to improve the approximation of the no-slip/no-penetration condition, (2) a correction for the excess in the effective particle diameter by a slight retraction of the Lagrangian grid from the surface towards the interior of the particle, (3) enhancing the numerical stability for solid-to-fluid-density ratios near unity by a direct account of the inertia of the fluid contained within the particle.

Collision model

The collision model employed in this study is the model described by Glowinski et al. [11]. This model provides for elastic collisions, i.e. there is no loss in kinetic energy as a result of a collision. This is achieved by adding a collision force and torque term (\mathbf{F}_c and \mathbf{T}_c) to the right hand side of Equation A.4 and A.5, respectively. The paper of Breugem [21] provides a clear description of the description model:

"Define $\mathbf{d}_{ij} = \mathbf{x}_{c,j} - \mathbf{x}_{c,i}$ as the distance vector between the centroid of sphere i and the centroid of another sphere labelled j . The distance vector points from sphere i towards sphere j . The collision model becomes active when the distance $\|\mathbf{d}_{ij}\|$ between the centroids of the two spheres is smaller than $D_p + d_c$, where d_c is a threshold distance that has to be specified. In case the threshold distance is exceeded, the collision force on sphere i due to a collision with a sphere j is computed according to:

$$\mathbf{F}_{c,ij} = -\frac{\rho_p V_p \|\mathbf{g}\|}{\epsilon_c} \left(\frac{\|\mathbf{d}_{ij}\| - D_p - d_c}{d_c} \right)^2 \frac{\mathbf{d}_{ij}}{\|\mathbf{d}_{ij}\|} \quad (\text{C.2})$$

where ϵ_c is a nondimensional parameter that has to be specified."

Equation C.2 holds for collisions of spheres with equal radii. The equation for the collision between a sphere and the wall is obtained by replacing D_p by R_p in Equation C.2 and $\|\mathbf{d}_{ij}\| = d_{wall} = \min(x_c, L_x - x_c, y_c, L_y - y_c)$. In all simulations the collision parameters are $\epsilon_c = 0.1$, $d_c/D_p = 1/16$ and $\mathbf{T}_c = 0$.

A simulation was performed to validate the collision model. In this simulation all forces on the particle are neglected except for the collision force. The particle is given an initial velocity of $\mathbf{U}_p = \langle 0, \mathcal{U}, 0 \rangle$, i.e. the particle moves towards the wall in the y -direction with a constant velocity. Figure C.2 shows the particle velocity in the y -direction in time. It can be concluded from this figure that there is no loss of kinetic energy, when the particle collides with the wall. Hence, the collisions are perfectly elastic.

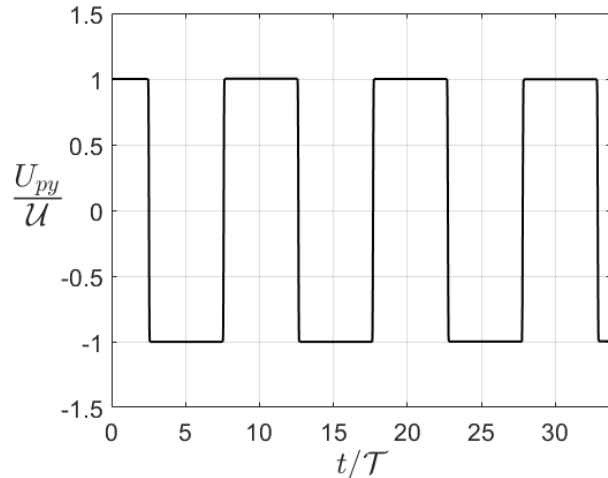


Figure C.2 The y -component of the particle velocity in time. The particle moves between the two walls in the y -direction. The line resembles a step function, which indicates perfect elastic collisions between the walls and the particle.

Appendix D

Additional simulations

D.1 Flow around a fixed sphere

Additional simulations involving the flow around a fixed sphere are performed prior to the simulations involving a single mobile sphere in order to extract (physical) parameters. These parameters are useful, when setting up the parameters for the single sphere simulations.

The computational box used for the fixed sphere simulations is similar to the one used for the sedimentation of a single sphere 2.1. In Table D.1 the inflow parameters for the simulations of the flow around a fixed sphere are displayed. Note that the values for w_∞/\mathcal{U} are obtained by solving Morison's equation for steady motion of a sphere settling under gravity B.4 (see Table B.1). The particle is held fixed at $x_c = y_c = 3D_p$ and $z_c = 6D_p$. For each case a simulation was performed with the duration of 4000 time steps. The duration of a time step depends on the inlet velocity at the inflow plane, which depends on the Galileo number Ga .

TABLE D.1: Simulation parameters and results for the flow around a fixed sphere.

Case	Ga	w_∞/\mathcal{U}	L_r
F144	144	1.2810	1.239
F178	178	1.3473	1.414
F200	200	1.3823	1.477
F250	250	1.4464	1.643

For the single sphere simulations it is desired that the flow around the fixed sphere is fully developed before releasing it. In this study the drag coefficient C_D was used in order to determine the flow to be fully developed. In Figure D.1 C_D is plotted against the time steps t_{steps} . From this plot it can be concluded that C_D becomes constant for all cases after 2000 time steps. Therefore the sphere is held fixed for 2000 time steps in the single sphere simulations for all four cases (S144, S178, S200, S250) corresponding to $t_{fixed} = 52.70\mathcal{T}, 51.93\mathcal{T}, 51.50\mathcal{T}, 48.73\mathcal{T}$ respectively (see Table 2.1).

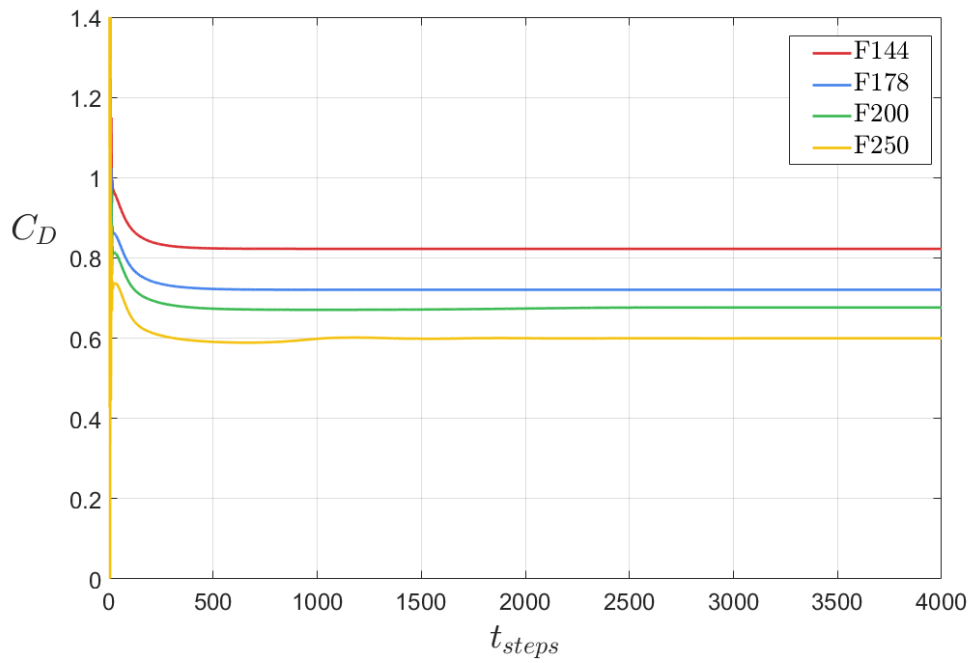


Figure D.1 Drag coefficient C_D plotted against the simulated time steps t_{steps} for the four fixed sphere cases.

Contour plots of the fluid velocity in the vertical direction w in the xz -plane and the yz -plane through the sphere centroid are given in Figures D.2-D.5. The re-circulation length L_r , which is the largest distance between the sphere surface and any point on the contour level $w = 0$, is marked in the plots with a red cross. The re-circulation length acts as an indicator for the wake length.

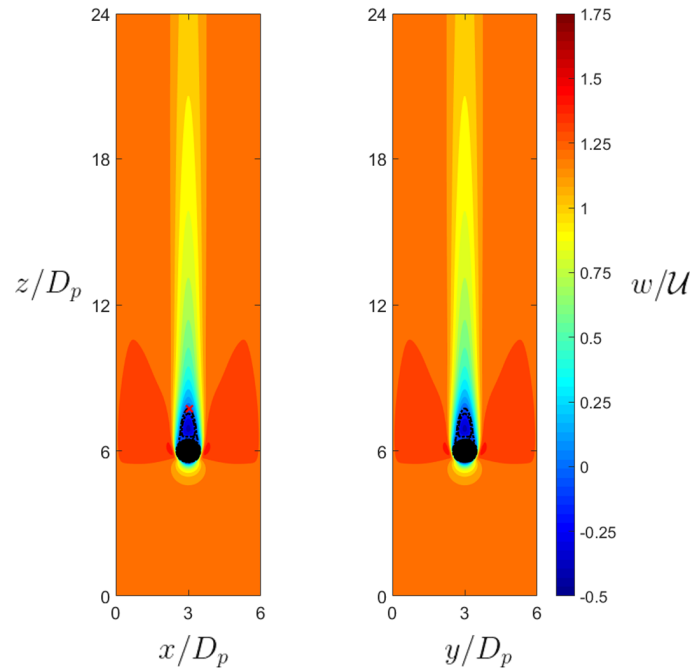


Figure D.2 Case F144. Contours at the xz -plane (left) and the yz -plane (right) through the sphere centroid. The distance between the surface of the sphere and the red cross indicates the re-circulation length. The black dash-dotted line encircles the re-circulation region. The re-circulation length $L_r = 1.239$.

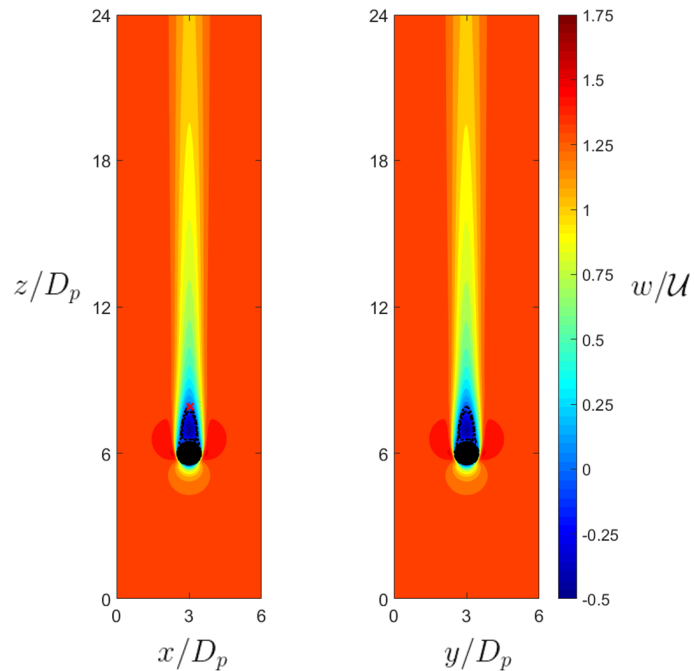


Figure D.3 Case F178. Contours at the xz -plane (left) and the yz -plane (right) through the sphere centroid. The distance between the surface of the sphere and the red cross indicates the re-circulation length. The black dash-dotted line encircles the re-circulation region. The re-circulation length $L_r = 1.414$.

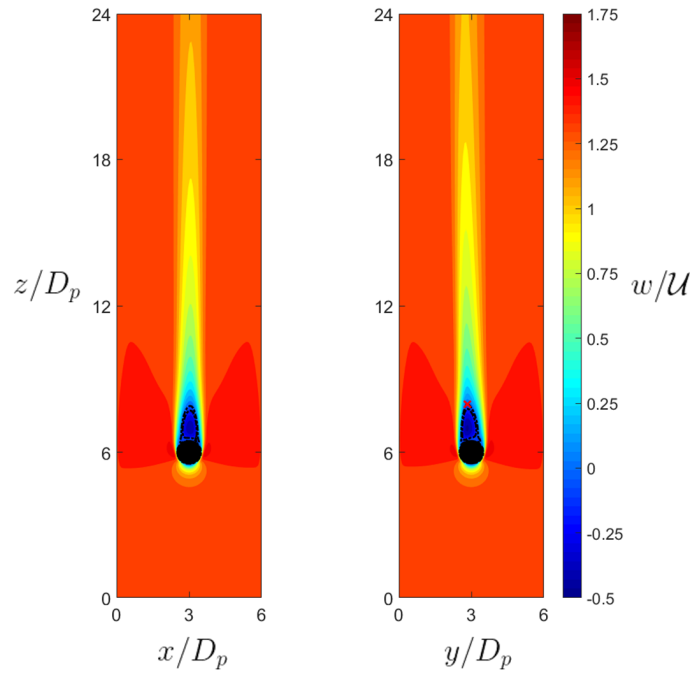


Figure D.4 Case F200. Contours at the xz -plane (left) and the yz -plane (right) through the sphere centroid. The distance between the surface of the sphere and the red cross indicates the re-circulation length. The black dash-dotted line encircles the re-circulation region. The re-circulation length $L_r = 1.477$.

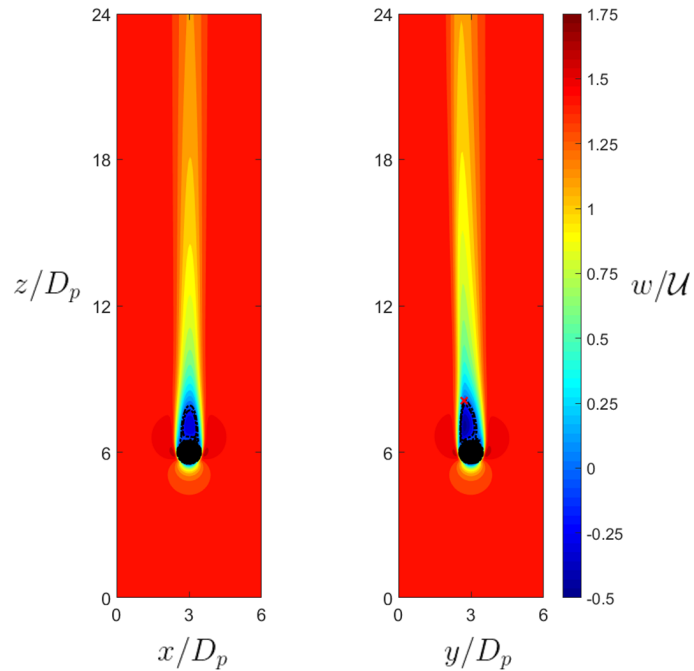


Figure D.5 Case F250. Contours at the xz -plane (left) and the yz -plane (right) through the sphere centroid. The distance between the surface of the sphere and the red cross indicates the re-circulation length. The black dash-dotted line encircles the re-circulation region. The re-circulation length $L_r = 1.643$.

D.2 Effect of periodic boundary conditions

For the most dilute suspension ($\Phi = 5.1 \cdot 10^{-3}$) multiple simulations were performed considering different domain heights L_z . Figure D.6 shows the settling velocity of the suspension as a function of the domain height for $Ga = 144, 178$ and 200 . From this plot it is concluded that by choosing a domain height $L_z = 72D_p$ for the most dilute suspension, the periodic boundary effects are significantly reduced.

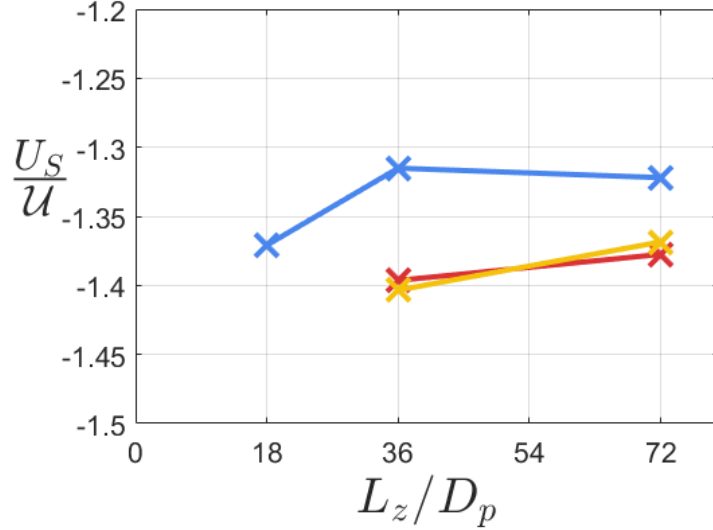


Figure D.6 Settling velocity of the suspension as a function of the domain height for $Ga = 144$ (blue crosses), $Ga = 178$ (red crosses) and $Ga = 200$ (yellow crosses) for the most dilute suspension ($\Phi = 5.1 \cdot 10^{-3}$).

Appendix E

Additional results

E.1 PDFs of the vertical particle velocity

The PDFs of the vertical particle velocity for solid-volume fractions $\Phi = 1.0 \cdot 10^{-2}, 2.5 \cdot 10^{-2}, 1.0 \cdot 10^{-1}, 2.0 \cdot 10^{-1}$ for $Ga = 144$ are given in Figure E.1.

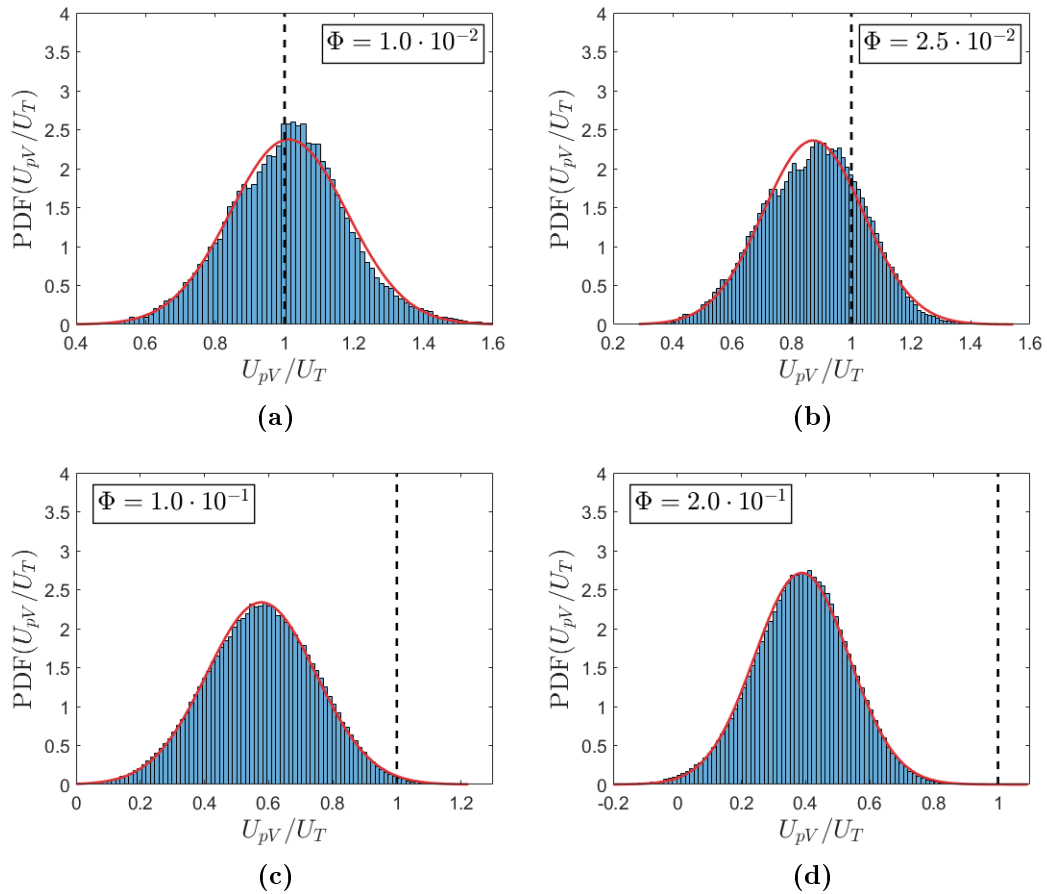


Figure E.1 Distribution of the vertical particle velocity for $Ga = 144$. The black dashed line indicates the settling velocity of a single sphere and the red line indicates the Gaussian distribution with a mean and standard deviation based on the vertical particle velocity simulation data.

The PDFs of the vertical particle velocity for solid-volume fractions $\Phi = 1.0 \cdot 10^{-2}, 2.5 \cdot 10^{-2}, 1.0 \cdot 10^{-1}, 2.0 \cdot 10^{-1}$ for $Ga = 178$ are given in Figure E.2.

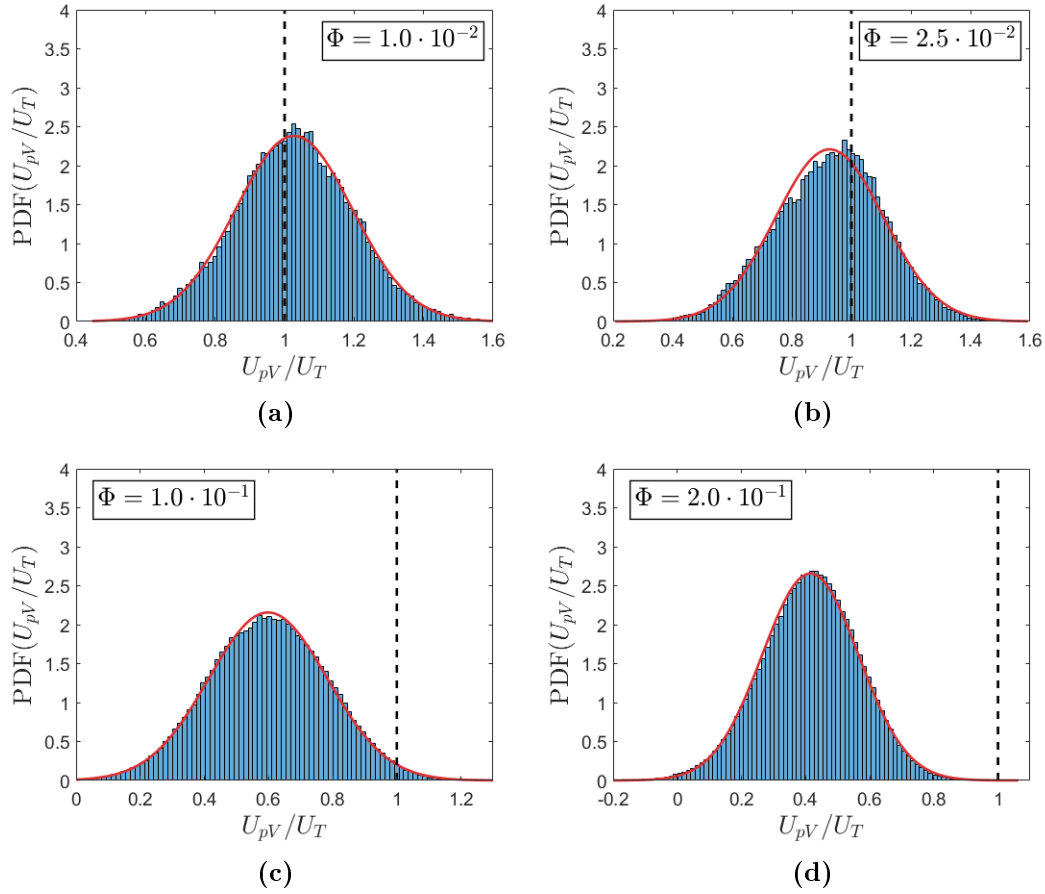


Figure E.2 Distribution of the vertical particle velocity for $Ga = 178$. The black dashed line indicates the settling velocity of a single sphere and the red line indicates the Gaussian distribution with a mean and standard deviation based on the vertical particle velocity simulation data.

The PDFs of the vertical particle velocity for solid-volume fractions $\Phi = 1.0 \cdot 10^{-2}, 2.5 \cdot 10^{-2}, 1.0 \cdot 10^{-1}, 2.0 \cdot 10^{-1}$ for $Ga = 200$ are given in Figure E.3.

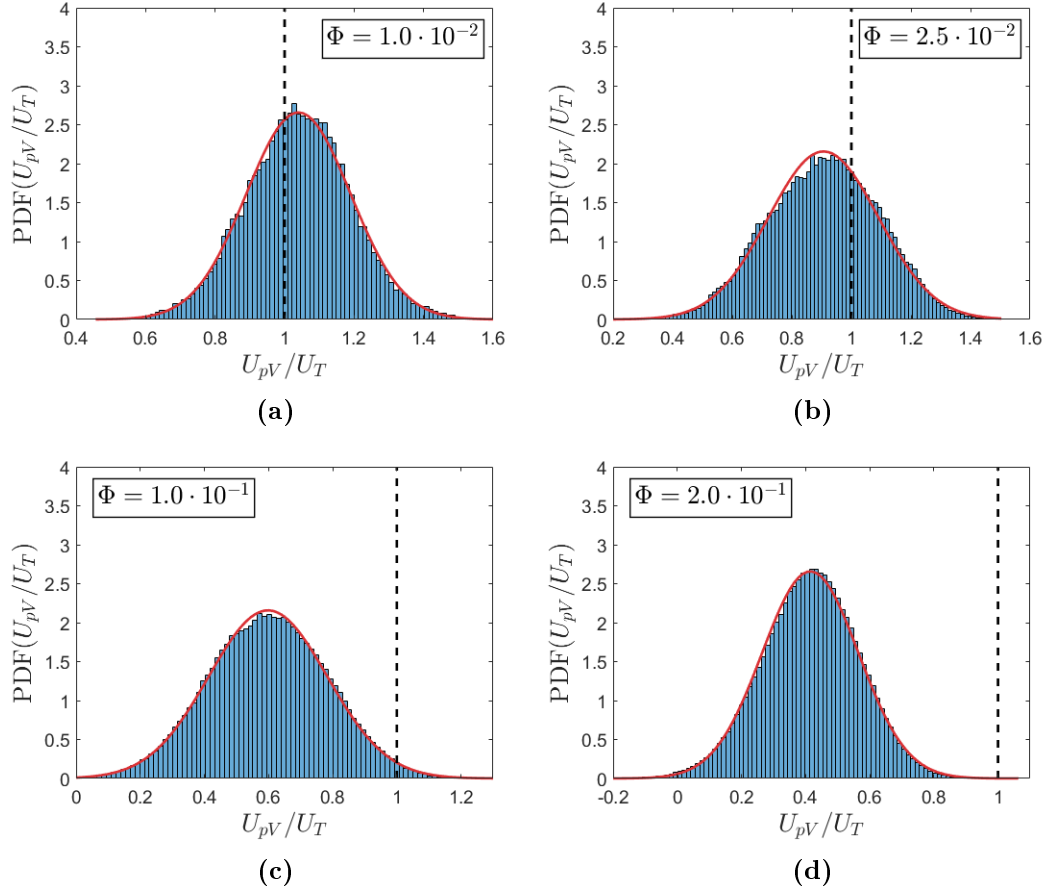


Figure E.3 Distribution of the vertical particle velocity for $Ga = 200$. The black dashed line indicates the settling velocity of a single sphere and the red line indicates the Gaussian distribution with a mean and standard deviation based on the vertical particle velocity simulation data.

Appendix F

Random generator for particle distribution

The code below was implemented in the Fortran to generate a random particle distribution.

```

1 %% Program to generate random 3d particle positions within ...
   computation domain without overlap
2 %% START
3 clc;close all;clear
4
5 %% RANDOM NUMBER GENERATOR
6 % Random number generator set to Non-Repeatability (=shuffle), where
7 % Repeatability (=default)
8 rng shuffle
9
10 %% PARAMETERS
11 % Set desired solid-volume fraction
12 Phi = 0.005;
13
14 % Diameter of the sphere
15 D_p = 1;
16
17 % Radius of the sphere
18 R_p = D_p/2;
19
20 % Set minimum distance between particles and between particle and wall
21 gap = 1/13;
22
23 % Domain dimensions
24 Lx = 6;
25 Ly = 6;
26 Lz = 36;
27
28 % Minimal allowable distance between the particle centroids
29 minAllowableDistance_p = 2*(R_p + gap);
30
31 % Minimal allowable distance between the particle centroid and wall
32 minAllowableDistance_w = R_p + gap;
33
34 % Number of particles
35 N_p = ceil((Phi*Lx*Ly*Lz*6)/(pi*D_p^3));
36
37 % Actual solid-volume fraction
38 concentration_check = (N_p*(pi/6)*D_p^3)/(Lx*Ly*Lz);
39
40
41

```

```
42 % Initialize first sphere centroid position.
43 keeperX(1) = Lx/2;
44 keeperY(1) = Ly/2;
45 keeperZ(1) = Lz/2;
46
47 counter = 2;
48
49 while counter ≤ N_p
50
51     % Get a trial point.
52     trialX = Lx*rand(1,1);
53     trialY = Ly*rand(1,1);
54     trialZ = Lz*rand(1,1);
55
56     for i=1:length(keeperX)
57         % Determine the distances between the trail point and the ...
58         % existing points.
59         distances(i) = sqrt((trialX-keeperX(i))^2 + ...
60                             (trialY-keeperY(i))^2 + (trialZ-keeperZ(i))^2);
61     end
62
63     minDistance = min(distances);
64
65     % Check if the minimal distance between the trial point and the ...
66     % existing points is allowed and to check wether the trial ...
67     % point is
68     % within the computational domain
69     if minDistance > minAllowableDistance_w
70         if trialX > minAllowableDistance_w && trialX < ...
71             (Lx-minAllowableDistance_w)
72             if trialY > minAllowableDistance_w && trialY < ...
73                 (Ly-minAllowableDistance_w)
74                 if trialZ > minAllowableDistance_w && trialZ < ...
75                     (Lz-minAllowableDistance_w)
76                     keeperX(counter) = trialX;
77                     keeperY(counter) = trialY;
78                     keeperZ(counter) = trialZ;
79                     counter = counter + 1;
80                 end
81             end
82         end
83     else
84     end
85 end
```

Bibliography

- [1] JF Richardson and WN Zaki. “Sedimentation and fluidisation: Part I”. In: *Chemical Engineering Research and Design* 75 (1997), S82–S100.
- [2] VM Boiko, AA Pivovarov, and SV Poplavski. “Measurement of gas velocity in a high-gradient flow, based on velocity of tracer particles”. In: *Combustion, Explosion, and Shock Waves* 49.5 (2013), pp. 548–554.
- [3] Mathieu Jenny, J Dušek, and G Bouchet. “Instabilities and transition of a sphere falling or ascending freely in a Newtonian fluid”. In: *Journal of Fluid Mechanics* 508 (2004), pp. 201–239.
- [4] CHJ Veldhuis and A Biesheuvel. “An experimental study of the regimes of motion of spheres falling or ascending freely in a Newtonian fluid”. In: *International journal of multiphase flow* 33.10 (2007), pp. 1074–1087.
- [5] M Horowitz and CHK Williamson. “The effect of Reynolds number on the dynamics and wakes of freely rising and falling spheres”. In: *Journal of Fluid Mechanics* 651 (2010), pp. 251–294.
- [6] Markus Uhlmann and Jan Dušek. “The motion of a single heavy sphere in ambient fluid: a benchmark for interface-resolved particulate flow simulations with significant relative velocities”. In: *International Journal of Multiphase Flow* 59 (2014), pp. 221–243.
- [7] Markus Uhlmann and Todor Doychev. “Sedimentation of a dilute suspension of rigid spheres at intermediate Galileo numbers: the effect of clustering upon the particle motion”. In: *Journal of Fluid Mechanics* 752 (2014), pp. 310–348.
- [8] Antonio F Fortes, Daniel D Joseph, and Thomas S Lundgren. “Nonlinear mechanics of fluidization of beds of spherical particles”. In: *Journal of Fluid Mechanics* 177 (1987), pp. 467–483.
- [9] James Feng, Howard H Hu, and Daniel D Joseph. “Direct simulation of initial value problems for the motion of solid bodies in a Newtonian fluid Part 1. Sedimentation”. In: *Journal of Fluid Mechanics* 261 (1994), pp. 95–134.
- [10] Neelesh A Patankar et al. “A new formulation of the distributed Lagrange multiplier/fictitious domain method for particulate flows”. In: *International Journal of Multiphase Flow* 26.9 (2000), pp. 1509–1524.
- [11] R Glowinski et al. “A fictitious domain approach to the direct numerical simulation of incompressible viscous flow past moving rigid bodies: application to particulate flow”. In: *Journal of Computational Physics* 169.2 (2001), pp. 363–426.
- [12] TE Baldock et al. “Settling velocity of sediments at high concentrations”. In: *Coastal engineering* 51.1 (2004), pp. 91–100.
- [13] Takeo Kajishima and Saotshi Takiguchi. “Interaction between particle clusters and particle-induced turbulence”. In: *International Journal of Heat and Fluid Flow* 23.5 (2002), pp. 639–646.

- [14] Takeo Kajishima. "Influence of particle rotation on the interaction between particle clusters and particle-induced turbulence". In: *International Journal of Heat and Fluid Flow* 25.5 (2004), pp. 721–728.
- [15] Sander G Huisman et al. "Columnar structure formation of a dilute suspension of settling spherical particles in a quiescent fluid". In: *Physical Review Fluids* 1.7 (2016), p. 074204.
- [16] Markus Uhlmann. "An immersed boundary method with direct forcing for the simulation of particulate flows". In: *Journal of Computational Physics* 209.2 (2005), pp. 448–476.
- [17] Walter Fornari, Francesco Picano, and Luca Brandt. "Sedimentation of finite-size spheres in quiescent and turbulent environments". In: *Journal of Fluid Mechanics* 788 (2016), pp. 640–669.
- [18] Elisabeth Guazzelli and Jeffrey F Morris. *A physical introduction to suspension dynamics*. Vol. 45. Cambridge University Press, 2011.
- [19] D Bruneau et al. "Three-dimensional intrinsic convection in dilute and dense dispersions of settling spheres". In: *Physics of Fluids* 10.1 (1998), pp. 55–59.
- [20] E Kuusela, JM Lahtinen, and T Ala-Nissila. "Sedimentation dynamics of spherical particles in confined geometries". In: *Physical Review E* 69.6 (2004), p. 066310.
- [21] Wim-Paul Breugem. "A second-order accurate immersed boundary method for fully resolved simulations of particle-laden flows". In: *Journal of Computational Physics* 231.13 (2012), pp. 4469–4498.
- [22] Robert H Davis, Jean-Marc Serayssol, and EJ Hinch. "The elastohydrodynamic collision of two spheres". In: *Journal of Fluid Mechanics* 163 (1986), pp. 479–497.
- [23] Fumio Takemura and Jacques Magnaudet. "The transverse force on clean and contaminated bubbles rising near a vertical wall at moderate Reynolds number". In: *Journal of Fluid Mechanics* 495 (2003), pp. 235–253.
- [24] Lanying Zeng, S Balachandar, and Paul Fischer. "Wall-induced forces on a rigid sphere at finite Reynolds number". In: *Journal of Fluid Mechanics* 536 (2005), pp. 1–25.
- [25] Jinhee Jeong and Fazle Hussain. "On the identification of a vortex". In: *Journal of fluid mechanics* 285 (1995), pp. 69–94.
- [26] Elisabeth Guazzelli and John Hinch. "Fluctuations and instability in sedimentation". In: *Annual review of fluid mechanics* 43 (2011), pp. 97–116.
- [27] JR Morison, JW Johnson, SA Schaaf, et al. "The force exerted by surface waves on piles". In: *Journal of Petroleum Technology* 2.05 (1950), pp. 149–154.
- [28] Phillip P Brown and Desmond F Lawler. "Sphere drag and settling velocity revisited". In: *Journal of Environmental Engineering* 129.3 (2003), pp. 222–231.
- [29] Farid F Abraham. "Functional dependence of drag coefficient of a sphere on Reynolds number". In: *The Physics of Fluids* 13.8 (1970), pp. 2194–2195.
- [30] RP Chhabra, S Agarwal, and K Chaudhary. "A note on wall effect on the terminal falling velocity of a sphere in quiescent Newtonian media in cylindrical tubes". In: *Powder technology* 129.1-3 (2003), pp. 53–58.
- [31] JR Strom and RC Kintner. "Wall effect for the fall of single drops". In: *AICHE Journal* 4.2 (1958), pp. 153–156.

- [32] Nicolas Mordant and J-F Pinton. “Velocity measurement of a settling sphere”. In: *The European Physical Journal B-Condensed Matter and Complex Systems* 18.2 (2000), pp. 343–352.
- [33] Charles S Peskin. “Flow patterns around heart valves: a numerical method”. In: *Journal of computational physics* 10.2 (1972), pp. 252–271.
- [34] Kun Luo et al. “Full-scale solutions to particle-laden flows: Multidirect forcing and immersed boundary method”. In: *Physical Review E* 76.6 (2007), p. 066709.